HIGH ENTROPY SULFIDES AS CATHODE MATERIALS FOR THERMAL
BATTERIES

A THESIS SUBMITTED TO
THE GRADUATE SCHOOL OF NATURAL AND APPLIED SCIENCES
OF
MIDDLE EAST TECHNICAL UNIVERSITY

BY

CEM AŞCI

IN PARTIAL FULFILLMENT OF THE REQUIREMENTS
FOR
THE DEGREE OF MASTER OF SCIENCE
IN
METALLURGICAL AND MATERIALS ENGINEERING

NOVEMBER 2024

Approval of the thesis:

HIGH ENTROPY SULFIDES AS CATHODE MATERIALS FOR THERMAL BATTERIES

submitted by **CEM AŞCI** in partial fulfillment of the requirements for the degree of **Master of Science** in **Metallurgical and Materials Engineering, Middle East Technical University** by,

Prof. Dr. Naci Emre Altun
Dean, Graduate School of **Natural and Applied Sciences**   _____

Prof. Dr. Ali Kalkanlı
Head of the Department, **Met. and Mat. Eng.**   _____

Assoc. Prof. Dr. Çiğdem Toparlı
Supervisor, **Met. and Mat. Eng., METU**   _____

Examining Committee Members:

Prof. Dr. Kadri Aydınol
Metallurgical and Materials Eng., METU   _____

Assoc. Prof. Dr. Çiğdem Toparlı
Metallurgical and Materials Eng., METU   _____

Prof. Dr. Hüsnü Emrah Ünalan
Metallurgical and Materials Eng., METU   _____

Prof. Dr. Yunus Eren Kalay
Metallurgical and Materials Eng., METU   _____

Assoc. Prof. Dr. Burak Ülgüt
Chemistry, Bilkent Uni.   _____

Date: 22.11.2024

I hereby declare that all information in this document has been obtained and presented in accordance with academic rules and ethical conduct. I also declare that, as required by these rules and conduct, I have fully cited and referenced all material and results that are not original to this work.

Name Last name : Cem Aşcı

Signature :

ABSTRACT

HIGH ENTROPY SULFIDES AS CATHODE MATERIALS FOR THERMAL BATTERIES

Aşcı, Cem
Master of Science, Metallurgical and Materials Engineering
Supervisor: Assoc. Prof. Dr. Çiğdem Toparlı

November 2024, 135 pages

Thermal batteries are primary batteries and are mostly utilized in military applications such as power supply for electronic units in guided missiles or satellites, and ejection seats in fighters. They exhibit high power density, long shelf life, which can be more than 25 years, and can perform under challenging operation conditions such as high acceleration and shock. Research on thermal batteries primarily focuses on developing new cathode materials to enhance electrochemical performance and meet evolving demands. Recently, high entropy materials have gained attention due to their unique properties arising from core effects like synergistic effect, lattice distortion, and sluggish diffusion. Although high entropy sulfides have been investigated in a few studies, there is obscurity on their applicability in batteries operating at elevated temperatures and requiring high current density profiles. This study focused on determining the electrochemical characteristics of these sulfides as thermal battery cathodes and investigated the effects of multiple equimolar cations on the electrochemical performance. High entropy sulfides were synthesized via solvothermal and mechanochemical methods. Single cell tests showed that these

materials significantly enhance open-circuit voltage, specific capacity, and energy at different discharge temperatures. Furthermore, their electrochemical characteristics were effectively manipulated by substituting primary elements such as chromium and manganese with copper and titanium, and by adjusting the molar fraction of the principal element cobalt. These results suggest high entropy sulfides can be tailored for thermal batteries requiring higher platform voltages with shorter operation times, lower discharge voltages with extended times, or high operating temperatures by modifying principal elements.

ÖZ

ISIL PİLLERDE KATOT MALZEMELERİ OLARAK YÜKSEK ENTROPİLİ SÜLFÜRLER

Aşcı, Cem
Yüksek Lisans, Metalurji ve Malzeme Mühendisliği
Tez Yöneticisi: Doç. Dr. Çiğdem Toparlı

Kasım 2024, 135 sayfa

Isıl piller, güdümlü füzelerdeki veya uydulardaki elektronik üniteler için güç kaynağı olarak ya da savaş uçaklarındaki fırlatma koltukları gibi çoğunlukla askeri uygulamalarda kullanılan birincil pillerdir. Bu piller yüksek güç yoğunluğu, 25 yılı aşabilen uzun raf ömrü ve yüksek ivme, şok gibi zorlayıcı çalışma koşullarında performans gösterebilme gibi özelliklere sahiptir. Isıl piller için yapılan araştırmalar, elektrokimyasal performansı artırmak ve zamanla gelişen gereksinimleri karşılayabilmek amacıyla genellikle yeni katot malzemeleri geliştirmeye odaklanmaktadır. Yüksek entropili malzemeler de sinerjik etki, kafes bozulması ve ağırlaşmış difüzyon gibi temel etkiler sayesinde sahip olduğu özgün özellikleriyle son dönemde ilgi çekmektedir. Yüksek entropili sülfürler az sayıdaki bazı araştırmalarda incelenmiş olsa da yüksek sıcaklıklarda çalışan ve yüksek akım yoğunluğu gereksinimleri bulunan pillerdeki uygulanabilirlikleri konusunda belirsizlikler bulunmaktadır. Bu çalışma, yüksek entropili sülfürlerin ısıl pil katotları olarak elektrokimyasal özelliklerinin belirlenmesine ve çok sayıda eşit mole sahip

katyonun elektrokimyasal performans üzerindeki etkilerinin araştırılmasına odaklanmıştır. Yüksek entropili sülfürler, solvotermal ve mekanokimyasal yöntemlerle sentezlenmiştir. Tek hücre testleri, bu malzemelerin farklı deşarj sıcaklıklarında açık devre gerilimini, spesifik kapasiteyi ve enerjiyi önemli ölçüde artırdığını göstermiştir. Ayrıca, bu malzemelerin elektrokimyasal özellikleri, krom ve mangan gibi temel elementlerin bakır ve titanyum ile değiştirilmesi veya kobaltın mol kesriyle oynanmasıyla etkili bir şekilde manipüle edilebilmiştir. Bu sonuçlar, yüksek entropili sülfürlerin temel elementlerinin değiştirilerek yüksek platform gerilimi ve daha kısa çalışma süresi, daha uzun çalışma süresi ve daha düşük deşarj gerilimi ya da yüksek çalışma sıcaklıkları gerektiren farklı ısıl pil uygulamaları için özel olarak tasarlanabileceğini önermektedir.

Anahtar Kelimeler: Isıl Pil, Yüksek Entropili Sülfür, Yüksek Entropi, Katot

Dedicated to my love and to my family…

ACKNOWLEDGMENTS

Lastly, my infinite appreciation and passion go to my fiancé, my constant inspiration, Bensu, for the countless weekends spent studying together, our insightful discussions, and for always uplifting me, even when I doubted myself. Your unwavering support and presence are the most essential part not only in this journey but in every moment of my life.

TABLE OF CONTENTS

LIST OF TABLES

TABLES

LIST OF FIGURES

FIGURES

LIST OF ABBREVIATIONS

ABBREVIATIONS

BET	Brunauer-Emmett-Teller
EDS	Energy Dispersive Spectroscopy
HRTEM	High-Resolution Transmission Electron Microscopy
ICP-OES	Inductively Coupled Plasma Optical Emission Spectroscopy
PPM	Parts Per Million
RH	Relative Humidity
RPM	Revolutions Per Minute
SAED	Selected Area Electron Diffraction
SEM	Scanning Electron Microscopy
TAA	Thioacetamide
TEM	Transmission Electron Microscopy
TGA	Thermogravimetric Analysis
Wt.	Weight
XPS	X-ray Photoelectron Spectroscopy
XRD	X-ray Diffraction

LIST OF SYMBOLS

SYMBOLS

C	Specific capacity [mAh/g]
G	Gibbs free energy [J/mol]
H	Enthalpy [J/mol]
S	Entropy [J/(K.mol)]
T	Temperature [°C, K]
α	Alpha phase
β	Beta phase
θ	Angle between the incident beam and diffracting planes
ε	Specific energy [Wh/kg]
%	Percentage
$\geq$	Greater than or equal to

CHAPTER 1

INTRODUCTION

Batteries are one of the essential technologies for energy applications. Their demand is expected to increase significantly in the following decade, and there have been a significant number of studies on that topic [1-2]. Thermal batteries are one type of primary, non-rechargeable batteries, and their applications are mostly restricted to military applications such as power supply for electronic units in guided missiles or satellites, and ejection seat applications in fighter jets [3-6]. They are rugged, durable, and have the capability to perform under extreme operation conditions such as high acceleration, shock, electromagnetic interference, vacuum, and different climates without any maintenance requisite [3,6,7]. Before activation, they can have a long shelf life that can be more than 25 years thanks to their special structure [7-9]. Thermal batteries use conversion mechanisms and mostly contain FeS_2 (pyrite), CoS_2, and NiS_2 as cathode materials, LiSi, LiAl as anode materials, eutectic salts with melting points between 300-450 ℃ as electrolytes, and iron powders with potassium perchlorate as heat pellets [3,4,7,10-14]. Developing new cathode materials is an important approach for improving the performance of thermal batteries and there have been various studies to find new cathodes having a reduction potential coherent with the electrolytes stability window, being stable at high temperatures, acting as electrical conductors, having low solvability in the liquefied electrolyte, and showing a high density of exchange current [13-65].

High entropy materials with more than five nearly equimolar elements have been studied recently. If the configurational entropy is high enough to categorize the material as high entropy, obtaining a single phase becomes easier and the resultant material can have unexpected properties thanks to inherent effects of high entropy such as lattice distortion, sluggish diffusion, and cocktail effect [66-72]. Although

the high entropy concept was started with high entropy alloys, it was then implemented in high entropy ceramics [67]. Some examples of these high entropy ceramics are oxides, carbides, nitrides, silicides, borides, fluorides, and sulfides [73-114]. High entropy sulfides are a new class of high entropy ceramics and there has been little research on that topic. They seem to be potential substitutes for metal sulfides having a wide variety of applications in electrochemistry thanks to their good specific capacities [115,116]. Synthesis methods of high entropy sulfides, however, has been a difficulty because of their proneness to reactions. Some of the reported high entropy sulfide production methods are pulse thermal decomposition or precursor decomposition [117,118], pressing under high temperature [115,119], high energy ball milling [74,120,121], cation exchange [122-124], solvothermal [125-128], thermal injection [129], and magnetron sputtering [130]. Although high entropy sulfides are mostly studied as oxygen evolution or reduction reaction electrocatalysts, their applications in batteries are limited [74,115-118,121,123-129]. In these few studies, high entropy sulfides showed interesting properties and enhanced the lithium-ion and sulfur-ion batteries performance [115,116,121,124].

However, the effects of high temperature or high current densities on the electrochemical characteristics of high entropy sulfides in batteries have not yet been determined. On the other hand, the possible synergistic contributions of high entropy sulfides with multiple equimolar cations to the electrochemical performance of thermal batteries and the feasibility of using them as thermal battery cathodes have also not yet been established.

In this context, the objective of this thesis is to determine the electrochemical characteristics of high entropy sulfides as thermal battery cathodes operating at high temperatures and to investigate the synergistic effects of multiple equimolar cations on the electrochemical performance of these batteries.

CHAPTER 2

LITERATURE REVIEW

In this part, a comprehensive overview of energy field, batteries, thermal batteries, high entropy concept, high entropy ceramics, and high entropy sulfides is performed. The literature survey is presented to show theoretical background of these relevant topics with the thesis.

2.1 Energy

Fossil fuels are still used as the energy source for energy generation, prevailingly. However, they create environmental pollution, and they have negative impacts on the climate. Expected difficulties for their extraction in the future, and the declining trend in reserves lead to develop alternative electricity-generating systems [1]. Batteries are one of the most growing technologies for current and future energy applications. The consumption of batteries is expected to be a quintuple increment in the following decade, and a diverse range of topics for different types of batteries have been studied [2].

2.2 Batteries

Batteries store energy by converting chemical energy to electrical energy. They consist of electrochemical cells which are composed of cathode, anode, and electrolyte materials. Separators are also used to prevent short circuits by separating the cell components both from the electrochemical cell they are in and between the other cells. Reduction process occurs in the cathode and the oxidation process occurs in the anode [1].

Batteries can be mainly categorized by their chemistry involved, execution or application area, and utilization type. Some examples such as lithium based batteries, nickel-based batteries may be given for the chemistry-type of classification. Industrial batteries, and stationary batteries can also be given as two examples for the classification with the applications of the batteries [2]. The other classification approach shows up from the utilization type of the batteries. In this type of classification, the batteries can be divided into two fundamental parts named as the primary batteries and the secondary batteries. Primary batteries are disposable, single use, one-shot batteries that can not be recharged. Because, in the discharging period of the primary batteries, the chemical degradation is irreversible. On the other hand, thanks to the reversibility of the chemical degradation process in the discharging stage, secondary batteries are rechargeable batteries, and can be utilized multiple times. These rechargeability in these types of batteries can be achieved by employing a reverse current for retrieving the building materials charging attributes [1,2]. The electrons are transported from anode to the cathode in charging process, while they are transported from cathode to the anode in the discharging period [1].

2.3   Thermal Batteries

2.3.1   Chronicle

Thermal batteries, also known as the thermally activated primary batteries, were initially designed, and utilized in the timezone of the second world war. During the war, the scientists in Germany aimed, and accomplished by the invention of the thermal batteries, at finding a new battery that does not need any preparation before use and can stand up to the flight dynamics [3,4]. V2 rockets were the first ammunitions containing the thermal batteries. In these pioneer thermal batteries, the heat needed to maintain the electrolyte's phase as molten is provided by the rocket's exhaust heat. After the war, the research and development of the thermal battery technology was mainly carried out in the United States as a result of the interrogation

of the scientists from Germany, and these batteries become unrivaled for the major military energy applications [3].

2.3.2 Applications of Thermal Batteries

The thermal battery application area is mostly restricted to military applications. They have critical roles in guided missiles and bombs, projectiles, proximity fuzes, torpedoes, military planes, spaceflights, and nuclear weapons [3-5]. They are majorly utilized in guided missiles for supplying power to critical electronic components such as guidance, radar, navigation, control, and fin motors. They are used in proximity fuzes for equipping and safeing procedures. In prolonged spaceflights, they are chosen as power sources for supplying energy to crucial electronic units. In some types of military planes hydraulics systems, they supply power in case of emergency [3,5]. Because of their remote actuation characteristic, they are also suitable for ejection seat applications in fighter jets [4]. Besides those applications, they can also be rarely utilized in marine execution areas, satellites, gas and oil boring, and some launch or ground vehicles [6].

2.3.3 Properties of Thermal Batteries

Thermal batteries are primary energy devices containing a molten salt separator in their cells and functioning between nearly 300 °C and 600 °C [3,7]. The functioning temperature is that high due to the salt mixture electrolyte used in these batteries which becomes molten when heated [6]. As a result of that intrinsic high temperature operation feature, their case temperatures can also be high during their performance and the generated heat may harm the adjacent systems to thermal batteries in their applications. The resultant heat can damage neighboring electronic components and infrared signatures. The batteries activation period alters with their dimensions and application areas and may vary from less than 50 milliseconds to more than a few tenths of a second. Their other beneficial features are being rugged, and durable and

having capabilities to perform under extreme operation conditions such as high acceleration, shock, electromagnetic interference, vacuum, and different climates without any maintenance requisite [3,6,7]. Until activation of the thermal batteries, they are inert, and the hermetic sealing technology ensures their inertness and provides them a significantly long shelf life that can be more than 25 years. After activation of the battery, they can generate and distribute power at exceptionally elevated values nearly 2 A/cm^2 on an average [3,7]. A single thermal battery is also able to supply different output voltages, and suitable for both constant loads and pulsed operations [6]. As the reaction of the anodes with the oxygen and damp is the principal degradation procedure of these type of batteries, preservation of the hermecity leads to a nearly limitless shelf life. They can also be stored and utilized in different extreme temperatures from -55 °C to +75 °C within their designed performance specification [3,7].

Thermal batteries are designed specially for the implementation. Special design requirements may alter the activation system and time, mounting type, electrical features, operation temperatures and parameters. Thus, those special type of batteries design and manufacturing parts are difficult and time consuming. Their designing and delivery time can be at least more than a half year [4,6]. On the other hand, their safety and reliability maintain their importance especially in military applications. They do not have an explosion risk for handling and conveyance, and the destruction procedures do not require special methods [6].

2.3.4 Structure of Thermal Batteries

The typical structure of a thermal battery and example products are given in Figure 2.1 [8].
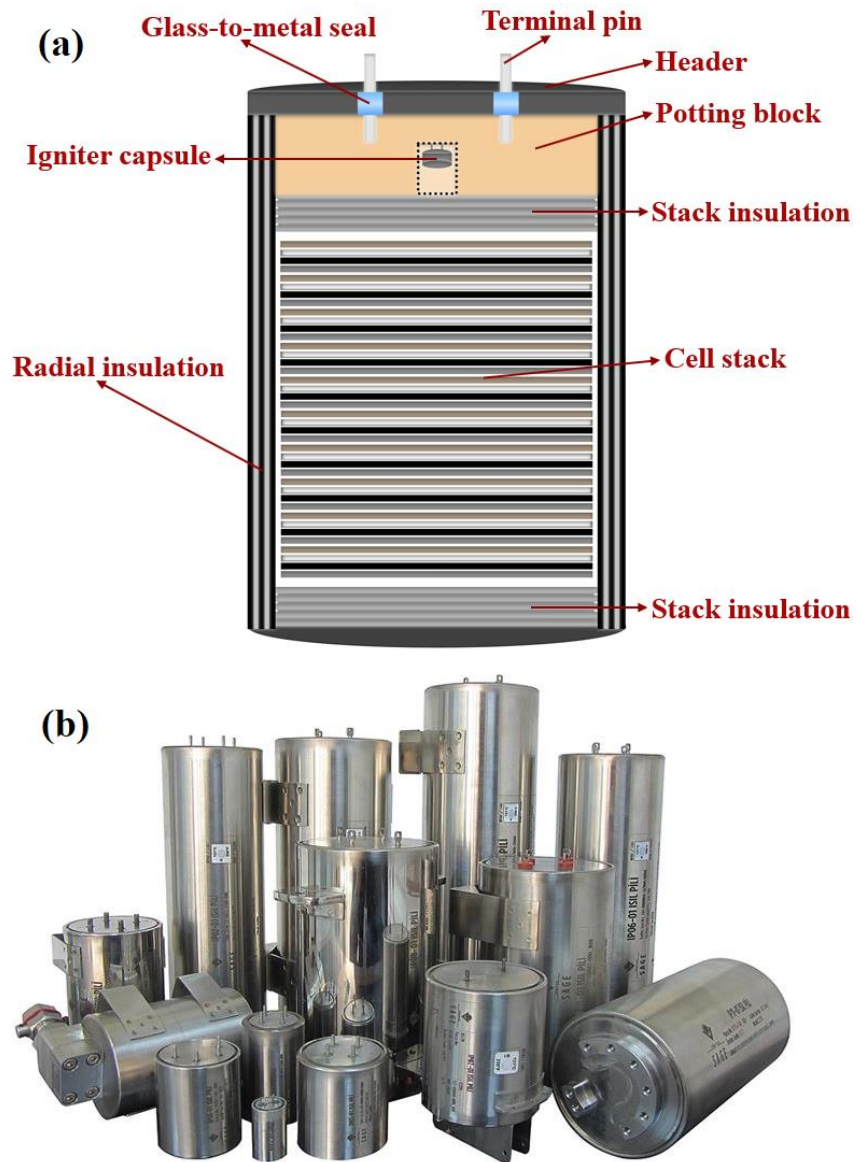
Figure 2.1. a) Illustration of structure, b) example products of thermal batteries [8].

In a thermal battery structure, there are repeating cells that each one of all having an anode, separator (electrolyte with a binder), cathode, and heat pellet. These cells can be assembled to cell stacks with parallel or series connections to design a thermal battery showing preferred voltage values [3,4,7]. These cell stacks voltage values are calculated by the open circuit voltages of the electrochemical pairs [7]. Representation of a thermal battery cell is given in Figure 2.2.
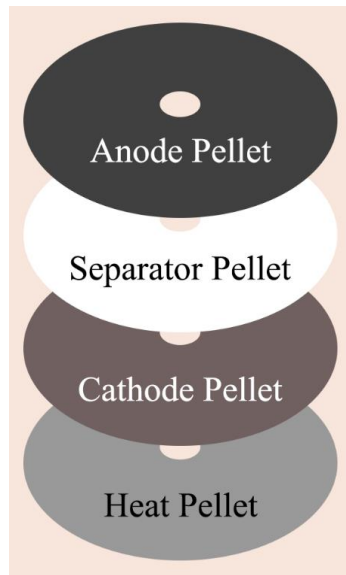
Figure 2.2. Representation of a thermal battery cell.

All of these cell components are in the solid phase at ambient temperature and, generally, they are manufactured by the powder-compaction technique from powders to pellets. These cells are surrounded by special insulation materials, and placed in a metal case. The particular thermal insulators surrounding the electrochemical cells in the thermal batteries are commercial composite materials named as Fiber Frax ® or Min-K ®. Aerogel insulations are also used as insulators. The metal case and cover located at the outmost part of the battery is mostly made of 304L stainless steel despite attempts with titanium or aluminum [3,4,9].

Due to comprising materials with hygroscopic properties, glass-to-metal sealing technology is used in thermal batteries to ensure spectacular shelf life. In those hermetic sealing procedures of thermal batteries, Corning 9013 or its equivalents are commonly used as the sealing glass. Thanks to the suitable thermal expansion coefficients and the other related coherent properties, special alloys named Alloy 52 or Kovar are generally utilized as terminal pins of the thermal batteries. Matching the Alloy 52 or Kovar terminal pins, Corning 9013 or equivalent glass, and the 304L stainless steel cover leads to a successful, and dependable glass-to-metal seal. Thus, this hermetic sealing technology used in thermal batteries is one of the primary reasons for their long shelf life [9].

While the commercially utilized cathode materials in thermal batteries are FeS_2 (pyrite), CoS_2, and NiS_2, the anode materials are mostly lithium based alloys. Lithium-silicon (LiSi) and lithium-aluminum (LiAl) are the most common examples of thermal battery anodes. In addition, LiB, and Li–Fe anodes are also utilized. The latter contains iron powders which hold liquid lithium in the anode structure to overcome the melting problem of the pure lithium at the thermal battery operating temperatures [7, 10].

As the electrolyte, the eutectic salts having melting points in the range of 300-450 °C are used. LiCl-KCl, LiF-LiCl-LiBr, LiCl-LiBr-KBr, LiCl-KCl-LiBr, and LiF-LiBr-KBr could be given as thermal battery electrolyte salts examples. In separator pellet, besides the electrolyte, magnesium oxide (MgO) powders are also used as binders [3, 4, 7].

Heat pellets are pyrotechnic materials and can be summarized as the mixtures of iron powders and potassium perchlorate ($KClO_4$) [7].

2.3.5 Working Principle of Thermal Batteries

Electrolytes used in thermal batteries are ionically nonconductive in their solid phases. If they change to their molten state, they become ionically conductive. In addition to solid electrolytes nonconductivity, being hermetically sealed makes thermal batteries completely inert before the activation [3, 4, 6].

The activation of the thermal batteries is performed by the ignition of the heat pellets that exist in each cells. Thermal battery cells and stacks are comprised of pellets having a hole in the centre position. The ignition of the battery is carried out by firing these holes with a pyrotechnic igniter or a fuse strip. This ignition mechanisms can include electric squibs or mechanical systems [4]. After the ignition of the heat pellets, they thermally decompose and distribute energy throughout every electrochemical cells and lead to a temperature raise in these cells. When the temperature exceeds the melting point of the salts (nearly 500°C), the electrolytes in

9

the separator pellets become molten and ionically conductive. Then, the resultant electrochemical reactions between the anode and cathode start leading to a power generation. As thermal batteries electrolytes have exceptional inherent ionic conductivities at the liquid state, the power arised can be transferred with greater rates than rival battery technologies. Current collectors and terminal pins located in the cover are utilized to convey the generated electrical current to the external connected systems. The operation of the thermal batteries can be finished by three main cases. The first case ending the operation is exhausting of the electroactive materials. Decrease of temperatures may lead freezing of the electrolytes, and that is another reason of the operation termination. Operation time differences are mostly originated from that reason, and the thermal insulation designs have a crucial impact on controlling the undesired heat transfer. The change of the electrolytes eutectic composition can also terminate the operation. Electrolytes composition can be changed by the precipitations occuring between the separator pellets and anodes resulting from the lithium ion concentration differences. Fast discharges of thermal batteries with high current densities increase the probability of the last case [3].

Prior the run of the thermal battery, the electrolyte is in the solid state. However, due to the melting of the electrolyte at the moment of the battery activation, the molten electrolyte must be kept in the pellet to prevent leakage between cell components. Magnesium oxide binders are utilized to hold the molten electrolyte in the separator pellets structure thanks to the capillary effect. In addition, the pellets mechanical characteristics have great importance on the behaviour of the electrolyte at the functioning temperatures. Because amount of the electrolyte and binder, powder compaction parameters and temperature have impacts on the mechanical properties of the separator pellets, all of these parameters affect the electrochemical performance of the battery [3].

During their operation period, thermal batteries must have a capacity to provide power constantly. Therefore, instead of intercalation mechanisms, conversion mechanisms are observed upon their functioning [11]. Following the activation, thermal battery electrolyte melts and ionic bridge between active materials is formed.

In the anode side, an oxidation reaction occurs, and positively charged ion with electron turns out. Conventionally used lithium-aluminum and lithium-silicon anode materials show different transition characteristics. Lithium-aluminum anode containing 20 wt. % Li show one transition from β (LiAl) to solid solution, α (Al). Based on these phases, the discharge mechanism for lithium-aluminum anode material is given in the following reaction [3, 4, 12]:

$$Li_{0.47}Al_{0.53} \rightarrow Li_{0.0578}Al_{0.53} + 0.411Li^+ + 0.411e^-$$ (2.1)

In contrast to lithium-aluminum, lithium-silicon anode shows more than one transition. The discharge steps of the lithium-silicon anode material are given [3, 4, 12]:

$$Li_{22}Si_5 \rightarrow Li_{13}Si_4 \rightarrow Li_7Si_3 \rightarrow Li_{12}Si_7$$ (2.2)
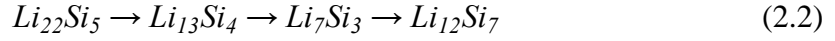
Since $Li_{22}Si_5$ is not convenient for processing in spite of containing more lithium, the transition from $Li_{13}Si_4$ to Li_7Si_3 is mostly preferred in thermal batteries. The preferred transition shows the following discharge mechanism [4, 12]:

$$Li_{13}Si_4 \rightarrow \frac{4}{3}Li_7Si_3 + \frac{11}{3}Li^+ + \frac{11}{3}e^-$$ (2.3)
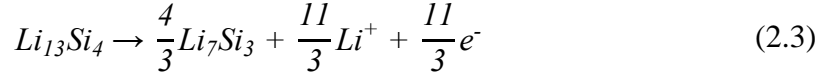
Then, the positively charged ion formed at the anode diffuses to the electrolyte and the cathode side. The positively charged ion, electron, and the cathode material trigger a reduction reaction at the cathode side, and complete the cell discharge mechanism. Pyrite (FeS_2), the mostly used cathode material of the thermal batteries, has more than one discharge steps. However, the thermal batteries application areas restrict their usage to only one mechanism since there are strict voltage demands. The FeS_2 cathode discharge occurs with the following reaction and approximately 2.1 V cell potential can be acquired [13]:

$$FeS_2 + \frac{3}{2}Li^+ + \frac{3}{2}e^- \rightarrow \frac{1}{2}Li_3Fe_2S_4$$ (2.4)
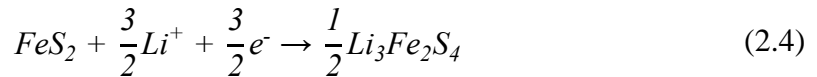
Cobalt disulfide (CoS_2) is the other commercially used cathode material in thermal batteries. Among CoS_2 cathodes different discharge steps, the serving one is given as follows [14]:

$$CoS_2 + \frac{4}{3}e^- \rightarrow \frac{1}{3}Co_3S_4 + \frac{2}{3}S^{-2} \tag{2.5}$$
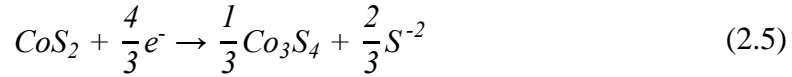
When the same electrolyte and lithium anode are utilized, the overall thermal battery cell voltage gained with the CoS_2 cathode is a little bit lower than the FeS_2 cathode. However, thermal battery cells using CoS_2 cathode materials show higher thermal stability and reduced internal resistance which brings important operational advantages.

2.3.6   Advances in Cathode Materials of Thermal Batteries

Since various complicated electrochemical and interdisciplinary mechanisms are involved in thermal batteries working principle, developments on the cathode electrode may lead to critical performance improvements. The most desired properties for thermal battery cathode materials are having a reduction potential coherent with the electrolytes stability window, being stable at high temperatures, acting as electrical conductors, having low solvability in the liquefied electrolyte, and showing a high density of exchange current [13]. Mostly, three main characteristics are crucial to determine whether a thermal battery cathode would be a high performance candidate. Thermal battery cathode materials thermal stability, capacity, and voltage should be high to achieve this object. The progress in the thermal battery cathodes can be based on different approaches. Modifying the surface structure is one of these approaches. The manufacturing method of the cell components can also be changed. In this manner, thin cathodes can be fabricated rather than the commercial pellet technology. Undoubtedly, searching for different materials or improving the available materials by compounding, alloying, or doping is the leading option in the thermal battery cathode development search field [15].

As previously mentioned in 2.3.4, FeS_2 is one of the predominantly used cathode materials in thermal batteries. Even though it can be utilized uncostly as a cathode after obtaining and purifying pyrite, its open circuit potential and thermal stability are evaluated as lower relative to other cathode candidates. There are various studies to enhance these properties and to improve the thermal batteries containing pyrite cathode [15]. In some of these studies, carbonaceous materials were used. One study about the addition of carbonaceous materials to the cathode is reported by Lee et al. [16]. They investigated the effect of the addition of multi-walled carbon nanotubes and carbon blacks on the performance of the batteries having FeS_2 cathode. Between different addition quantities starting from 0.1 wt. % (relative to the amount of cathode active material), the addition of 1 wt. % carbon nanotube or carbon black resulted in a thermal battery with the highest voltage and improved discharge time values over the entire range. Meanwhile, the internal resistance values of the cathode are decreased by the addition of these carbonaceous materials. These outcomes showed that carbon blacks or multi-walled carbon nanotubes may be used to enhance the electrochemical performance of the FeS_2 cathode by improving the conductivity.

Changing the manufacturing method of the FeS_2 cathode was also studied. The prevalent pellet cathodes have some disadvantages. The powder pressing requires thicker cathodes than the optimum value in terms of electrochemical properties to ensure the mechanical integrity of the finalized pellets. Since having a thicker cathode material lessen the utilization of the active material, making the electrode thinner has been an important approach to improve thermal battery performance. For instance, Yoon et al. [17] prepared and evaluated thinner cathodes instead of pellets by implementing the tape casting process. Firstly, they used ball millling to form a uniform mixture of slurry containing active material (FeS_2), organic binders (polysiloxane, silicic acid), and solvents (benzene, acetone). Then, with the doctor blade process, they applied the tape casting to achieve a thin cathode on a current collector substrate. The obtained flexible, thinner cathode preserved its mechanical strength under harsh deformation and comprised nearly 20 wt. % more active material with an increased utilization rate of the electrode material. Based on the

single cell electrochemical test results, the discharge capacity of the thinner FeS_2 cathode was nearly twice that of the equivalent pellet FeS_2 cathode with a cut-off voltage of 1.3 V. In spite of these advantages, containing organic binders can cause temperature related problems due to the high operation temperature of thermal batteries. Yoon et al. [18] have another study to remark and solve these binder-related problems on thin cathodes. While operating the thermal battery, due to the organic binders, gas generation occurs and the binder residuaries create resistivity leading to a performance decrease. To overcome these problems, they used multi-walled carbon nanotubes as the binders for the tape casting process. Using carbon nanotubes provided to decrease the binder amount one-fifth of the thin cathode containing polysiloxane and silicic acid binders, to increase active materials amount, thus increasing energy density. Multi-walled carbon nanotubes performed with successful mechanical strength, and better thermal stability than the former organic binders. In addition, the thin cathode having multi-walled carbon nanotubes as binders exhibited higher discharge capacity and lower internal resistance than the cathode with an identical thickness and organic binder. Similar approaches that include finding different manufacturing techniques compatible with the thermal battery cathode thickness and material requirements are also possible. They all aim to increase the active materials utilization rate by thinning the electrode and need specific studies to determine suitable materials with process parameters for obtaining successful thermal battery cathodes [15].

Decreasing the particle size of the FeS_2 cathode was another approach to improve the electrochemical characteristics. Sanchez et al. [19] investigated the effects of nanostructuring the FeS_2 on the discharge performance and thermostability. They utilized high-energy ball milling and obtained nanoscale FeS_2 cathodes having nearly 50 nm crystallite size, 2 μm mean particle size, and approximately 65 nm BET equivalent diameter. It was reported that, although the nano-sized cathode's thermal decomposition mechanism was identical to the conventional micron-sized cathode, the nano-sized FeS_2 thermal decomposition started in relatively lower temperatures which may negatively impact the thermal battery performance in higher

temperatures. The electrochemical test results confirmed that the performance comparison of these cathodes was altered by the temperature changes, and the nano-sized cathodes showed higher voltages with increased discharge time than the micron-sized cathodes up to 550 °C. After that temperature, micron-sized FeS_2 performed better.

CoS_2 is the other most used cathode material in thermal batteries. In contrast to FeS_2, it is produced in the laboratory causing it to be more expensive. Having a slightly lower (0.1 V for a cell) electromotive force than FeS_2 is another disadvantage. On the other hand, CoS_2 cathode material's lower impedance, higher electronic conductivity, lower solubility in eutectic salts, and higher thermal stability make them more suitable for applications having more operational times [14]. For the CoS_2 thermal battery cathode, there have been quite similar studies with the abovementioned papers, such as the addition of carbonaceous materials, and the implementation of different manufacturing methods to obtain thinner cathodes [20,21]. Apart from these similar approaches, there are also some compounding studies of CoS_2 and FeS_2 to benefit from their intrinsic advantages as a single cathode material. For instance, Zhu et al. [22] reported that $Fe_{0.5}Co_{0.5}S_2$ material can be synthesized by different methods and be used as a thermal battery cathode. They synthesized the new disulfide both with a mechano-milling process and by the sulfuration of a liquid precursor at a high temperature (approximately 700 °C). They notated the procedures as solid state and liquid phase, respectively. The electrochemical discharge tests showed $Fe_{0.5}Co_{0.5}S_2$ materials performance eliminated the performance of FeS_2 with a 1.25 V cut-off voltage at 0.3 A/cm^2. Moreover, the cathode synthesized with the liquid phase method was more successful in terms of specific capacity, thermal stability, and uniformity. A molten salt approach was also considered to synthesize that bimetallic disulfide by Liu et al. [23]. In the method, raw materials were thiourea, cobalt oxide, and iron oxide. And, the procedure comprised high-energy ball milling, retort furnace treatment, and calcination. They reported that the obtained product showed good environmental

stability even under excessive relative humidities together with enhanced specific capacity.

The abovementioned studies show that new cathode systems combining CoS_2 and FeS_2, which improve the thermal stability and conductivity of FeS_2, and lessen the necessary amount of expensive CoS_2, can serve new thermal battery designs thanks to altered electrochemical and physical properties.

After FeS_2 and CoS_2, the most regardable thermal battery cathode material is NiS_2. Its both electromotive force per cell and thermal decomposition properties are in the middle of the values of the two leading cathode materials. As it has reasonable electrochemical properties with a lower cost compared to CoS_2, it may replace CoS_2 depending on the application. However, NiS_2's electrochemical performance cannot highly dominate over FeS_2 if the cost difference is accounted for. These parameters encouraged some studies to improve the performance of NiS_2 [14]. Similarly to the FeS_2 and CoS_2 thermal battery cathode studies, carbon coatings and thinning of the NiS_2 cathodes for achieving flexible, thin cathodes were reported [24-26]. Unlike these researches, modifying the material structure was also one of the most highlighted approaches. For example, Fan et al. [27] investigated various structures to increase the contact between the electrolyte and NiS_2 cathode. Since nanocrystallization reduces the necessary distance of the lithium ions to move upon discharge, they studied three different nanostructures as a thermal battery cathode. The NiS_2 cathode structure types were nanostructure, globose structure, and hierarchic structure. The globose and hierarchic structures were containing both micro and nano groups. All of the structures were synthesized by a hydrothermal method starting with a nickel (II) chloride hexahydrate precursor. Although they all were sulfurized with thioacetamide (TAA) as the sulfide ion source, different chemicals were added to the starting precursor to obtain the globose and hierarchic structures. Following the synthesis of the different NiS_2 structures, a sintering process was applied to them. This process enhanced the electrochemical performance of NiS_2 cathodes by increasing the contact between the cathode and electrolyte and reducing the resistance. The thermal stability of the hiearchic

structure was worse than other structures because the hierarchic structure was a three dimensional network and able to hold remaining sulfur. In addition, the hierarchic structure was reported to be unsuitable for flowing and infiltrating the thermal battery electrolytes into that electrode. This resulted in a weaker electrochemical performance than the nanostructure and the globose structure, and the nanostructure performed the best capacity results with a 0.2 A/cm^2. The study underlined that not only the material types dictate the performance of cathodes but also the structure does. Besides the structural alterations, doping of NiS$_2$ with different elements was also studied [28-31]. In one of these studies, Zhou et al. [31] doped the cathode with Cu, Cr, Co, and Fe with a formula of Ni$_{0.8}$M$_{0.2}$S$_2$ where M stands for the doping elements. The synthesis of the doped powder was carried out by a ball milling process followed by a sintering mechanism. The doping of multiple metals decreased the particle size, increased the surface area, and created vacancy locations. It was reported that these doping effects led to a conductivity increase. One of the most important results was the increase of the thermal stability of the NiS$_2$ by doping these elements. The doped NiS$_2$'s (Ni$_{0.8}$M$_{0.2}$S$_2$) thermal decomposition was shifted more than 100 °C with the same mass decrease ratios. Thanks to the improvements in thermostability and electrical conductivity, the Ni$_{0.8}$M$_{0.2}$S$_2$ cathode performed better than NiS$_2$ under 0.1 A/cm^2 and 0.5 A/cm^2 which represented the constant current and pulse discharge tests, respectively with a 1.5 V cut-off voltage. The specific capacity increase was nearly 15%.

Alternative synthesis methods of the abovementioned, leading thermal battery cathodes were also studied. Zhao et al. [32] prepared each of the three most preferred cathode materials by a high temperature solid state approach with increased production effectiveness. In the synthesis, the related metal and sulfur monomer powders were roasted for less than 10 hours with temperatures different for each desired sulfide material, after a fast ball milling. Then, calcination and grinding procedures were performed to obtain single phase final products. They claimed that the production was easier, more efficient, and more suitable for scale-up requirements than the common sulfide synthesis methods.

Studies about thermal battery cathodes are mostly related to FeS_2, CoS_2, and NiS_2 materials because of their proven reliability developed over the years and mature production procedures. Nevertheless, there has also been research on finding new suitable materials, such as transition metal chlorides and transition metal fluorides, showing promising thermal and electrochemical properties which can provide size reduction of thermal batteries and expand their space and military applications [33].

$NiCl_2$ is one of the cathode materials studied except for the three leading disulfides. Its relative potential, gravimetric energy density, and discharge current are high with a low price. However, its excess solubility in thermal battery electrolytes and low electronic conductance restrict the usage of $NiCl_2$ as cathodes [15,33]. Several studies have been reported to investigate the feasibility of the material, eliminate the mentioned problems, and enhance the intrinsic advantages of $NiCl_2$ to make it a serious alternative thermal battery cathode material [34-42]. In one of these several studies, a composite material was designed with NiS_2 material by Zhou et al. [35]. They aimed to reduce the $NiCl_2$'s solubility in electrolytes and achieved a high voltage (nearly 2.8 V) with an increase of gravimetric energy density thanks to the less molten salt solubility. In addition to the high solubility in molten salts, low intrinsic conductivity negatively impacts the $NiCl_2$'s performance, as well. It causes slower activation of the battery and undesired voltage decreases. Moreover, $NiCl_2$ mostly comprises crystal water and its hydrolysis reaction product NiO also reduces the conductivity since it is an insulator [36]. Hu et al. [36], eliminated the water from the structure by roasting. Then, they reported a reduction method with hydrogen that the insulator product of the hydrolysis was altered to a conductor, Ni. As a result of that transformation, the conductivity of the cathode was increased, the pulse discharge characteristics were improved, and the activation became faster. In another approach, Liu et al. [39] reported that doping Br to $NiCl_2$ eased the ionic movements, increased the conductivity, and decreased the voltage drops. However, the thermostability of the cathode declined as the doping quantity increased, thus, the doping seemed to both have positive and negative impacts on the electrochemical performances of thermal battery operations. Zhao et al. [41], on the other hand,

designed a different $NiCl_2$ having a rhombohedral structure with a carbon barrier layer covering the outside of the active material. They coated the cathode powders with a dispersion of polyvinylpyrrolidone in ethanol and calcined the obtained product. The amorphous carbon coated $NiCl_2$ structure showed a higher specific surface area and mean size of pores leading to a better environment for electrochemical reactions. They reported that the structure also improved the structural stability and provided the ability of the cathode to maintain its integrity longer. These improvements enhanced the gravimetric energy density of the cathode. Liu et al. [42] showed that Co doping can also increase the conductivity and the capacity of the $NiCl_2$ cathode. The cathode material was synthesized with a nanosized sheet structure and it was reported that the capacity increase was provided by the enhanced height to diameter proportion with significant specific surface area leading to more electrochemically active positions.

In addition to $NiCl_2$, different transition metal chlorides including $PbCl_2$, Li_6VCl_8, Li_2MnCl_4, and $KNiCl_3$, were also studied [34, 43]. Shen et al. [43] reported that $PbCl_2$ provided a higher active material utilization ratio than the commercial cathodes and performed a stable discharging process. On the other hand, the main advantage of the other chlorides was their elevated cell voltages [34].

Similarly to the transition metal chlorides, fluorides have also been studied for thermal battery cathode applications. Their thermostability, voltage, and gravimetric energy density are high, giving them an opportunity to be thermal battery cathode material candidates [33]. FeF_3 is one of the reported qualifiable fluorides as a thermal battery cathode. Although it has a high open-circuit voltage, thermal stability, and cost-effectiveness, its electrical resistance is also elevated due to the intensive ionic bonds and it limits commercialization. Thus, the research on the FeF_3 has been mainly focused on enhancing the electrical conductance property [44,45]. Another fluoride, NiF_2, was reported as a suitable candidate by Zhou et al. [46] if there is a high power density requirement. The discharge tests with current densities up to 0.5 A/cm^2 showed that the fluoride's power density can reach nearly 17000 W/kg. Different from the suitability of NiF_2's high power applications, MnF_3 was also

reported as an accommodable cathode material for applications demanding higher voltage and running time. A study by Hu et al. [47] showed that the voltage of the MnF_3 cathode could reach approximately 3.5 V with an extended operation time. Moreover, it also successfully performed higher voltage values than the commercial cathodes under extreme current densities.

The other prospective materials that have been studied for increasing the thermal battery cell voltage and the specific capacity are oxides. For example, different copper vanadate materials were attempted as thermal battery cathodes [48-50]. Ein-Eli et al. [48] reported that although the thermal stabilities of $Cu_2V_2O_7$ and CuV_2O_6 were favorable and the voltage reached nearly 3.5 V with a low current density, the voltage values dropped when a high current density was applied. Reisner et al. [49] also studied similar materials as thermal battery cathodes. They synthesized $Cu_5V_2O_{10}$ and $Cu_3V_2O_8$ thin film cathodes. The prepared thin film copper vanadates reached better capacities in comparison with the pellet counterparts. Different than copper vanadates, the feasibility of vanadium oxides [51,52], copper oxides [53-55], nickel oxides [56,57], and lithium copper oxide compounds [58] have also been researched as thermal battery cathode active materials. Improving the electrical conductivity and decreasing the solubility in thermal battery electrolytes of V_2O_5, were the research aims of the example studies [51,52]. CuO was evaluated as a possible cathode candidate thanks to its good thermostability and specific energy with relatively lower costs [53-55]. As a result of NiO's high thermal stability, it performed as a promising thermal battery cathode even under 700 °C [56,57]. The specific capacity of $LiCu_2O_2$ outperformed the leading disulfides under 0.1 A/cm^2 with a 1.5 V cut-off voltage [58].

Not only have been studied chlorides, fluorides, and oxides to replace commercial thermal battery cathodes but also alternative sulfide materials were examined. Following the commercial disulfides FeS_2, CoS_2, and NiS_2, one of the most focused sulfide materials is WS_2 [59-62]. Wang et al. [59] prepared WS_2 with a nanosheet structure. Although the material showed spectacular thermal stability with only about 1 wt% mass loss under 1200 °C, a low cell voltage below 1.5 V was reported. Besides

the cell potential, WS$_2$'s electrical conductivity is also low because of the material's semiconducting nature [60]. One of the efforts to enhance the conductivity was made by Zhu et al. [60]. They incorporated sulfur vacancies into the structure and the electrochemical performance of the thermal batteries with WS$_2$ cathodes increased thanks to an improved electrical conductivity. In addition, the remarkable thermostability of WS$_2$ beyond 1000 °C was preserved after introducing these defects to the structure. Zhu et al. [62] also prepared composite materials containing both sulfur and oxygen vacancies. They reported that WS$_{2-x}$-WO$_{3-x}$ material's voltage, operation time, and compatibility for pellet pressing were better than WS$_2$.

MoS$_2$ is another sulfide studied as a thermal battery cathode. MoS$_2$'s inherent conductivity is lower than WS$_2$ and it negatively affects the comparison of the electrochemical performance between them [59]. Although MoS$_2$ is inferior to the thermal stability of WS$_2$, it has higher thermal stability, up to 700 degrees, than existing commercialized cathodes [63].

Despite the presence of studies about different sulfides such as ZrS$_3$ [64] and SnS$_2$ [65], the feasibility of using these materials as thermal battery cathodes has not been evaluated comprehensively, yet.

2.4   High Entropy Materials

The relation between the mixing enthalpy, entropy, and the expected phase stability can be interpreted from the Gibbs free energy of mixing calculated by the following equation [66,67]:

$$\Delta G_{mix} = \Delta H_{mix} - T\Delta S_{mix} \tag{2.6}$$

As the second term containing the temperature and the entropy of mixing is higher than the first term, which is the enthalpy of mixing, a negative Gibbs free energy of mixing value is obtained. This negative free energy means the mixing entropy excels the extra enthalpy necessary for creating a mixture of various elements, and results in the entropic stabilisation of the crystal lattice. The entropy of mixing can be

affected by different entropy elements. These are electronic, magnetic, vibrational, and configurational entropy. Among these, the configurational entropy has much more impact on the entropy of mixing, and the calculations for entropic stabilisation are mostly based on these types of entropy definitions. Although the vibrational element also may affect the configurational entropy, it is not enough to settle the stability of phases alone [66,68]. Higher solid solution components in numbers raise the mixing configurational entropy and this may increase the probability of achieving a single-phase material [69]. The generalised equation for calculating the mixing configurational entropy is given in the following generalised equation [66,67]:

$$\Delta S_{mix,conf} = -R \sum_{i=1}^{n} x_i \ln x_i \qquad (2.7)$$

In the equation, x_i stands for the molar fraction of the corresponding constituent, R represents the ideal gas constant, and n is the number of constituents [66,67]. The highest configurational entropy of mixing can be achieved with equimolar conditions and the equation can be simplified to the following formula in this case [67]:

$$\Delta S_{mix,conf} = R \ln n \qquad (2.8)$$

If the configurational entropy of mixing is equal to or higher than 1.5 R, the material can be categorized as high entropy. Thus, the high entropy materials contain minimum five primary elements having nearly equivalent atomic ratios [66,67,69]. Since the increment of the configurational entropy is less than 3% from 13 primary elements to 14 elements, the upper principal element limit is commonly accepted as 13 elements for practical applications. It is evaluated that increasing the number of primary elements beyond the practical upper primary element limit can lead to processing problems with an insufficient entropy gain [70].

Four fundamental concepts have been proposed to explain the mechanisms distinguishing the properties of high entropy materials from other materials. These concepts are defined for high entropy alloys preliminarily and then broadened for every high entropy material. The first mechanism, the high entropy effect, arises from the highness of entropy and is related to thermodynamics. Elemental phases

have low enthalpy and entropy of mixing, compounds have high enthalpy and low entropy of mixing. On the contrary, solid solutions have high mixing entropy and medium mixing enthalpy. Since the smaller free energy of mixing leads to stable states, solid solutions with several elements have the importance of creating equilibrium conditions, and higher mixing entropy values can improve the probability of obtaining steady solid solutions rather than different compounds. Thus, the structure of the materials having multiple elements can be stable and plain thanks to the high entropy effect. Similar atomic radii of the participating elements, greater entropy of mixing, and lower mixing enthalpy are crucial factors in increasing the probability of forming these unordered solutions [70].

The second core mechanism of high entropy materials is about kinetics and called as sluggish diffusion. In high entropy materials, various types of elements create different lattice energies among lattice positions. The positions with lower energies obstruct the diffusion of the elements and vacancies. That potential energy differences increase the necessary diffusion activation energy, makes the movements harder of the diffusing constituents, and slow down the mechanism. Additionally, the sluggish migration leads to slower phase transitions making microstructural engineering easier than conventional materials. The sluggish diffusion concept of the high entropy materials becomes more apparent when there are more participating elements in the structure. Higher creep strength, lower grain growth rate, and higher temperature of the recrystallisation are some of the helpful attributes resulting from that effect [70,71].

Distortion of the lattice, the other fundamental effect of high entropy materials has relevance to the structure. Because these materials contain several types of elements having different atomic radii, some stress and strain occur in the lattice. These diverse elements bond with adjacent atoms by different binding energies and it also causes fluctuations in the crystal structure. In addition, elements locations become unclear in the crystal structure due to these deformations which increases the configurational entropy. The lattice deformation effect leads to enhancements in mechanical properties thanks to the inherent solid solution strengthening

mechanism, and weakening of thermal and electrical conductions because of the scattering of the phonons and electrons. Besides the property alterations, it also affects X-ray crystallography results. Since X-ray scatters from the distorted crystal planes of high entropy materials, the intensity of the resultant peaks becomes lower. Beyond these, lattice distortions provide a temperature independency for the properties of the high entropy materials [70,72].

The last concept related to high entropy materials is the cocktail effect. That effect explains the superadvenient property changes based on the reciprocal influences of the wide range of different atoms. The high entropy materials properties can show better properties than expected thanks to interactions between the various elements and different phases at the atomic level, and they display high performance in a similar manner to the concept of composite materials [70]. A wide range of elements in the structure leads to complicated interactions in between, and surprising properties could be achieved it is not possible to ascribe one of the singular elements in the material. Therefore, modifying the compositions can provide important alterations to these complicated reciprocations and the material properties differ substantially [68].

A schematic illustration of the four core effects ascribed to the high entropy concept is given in Figure 2.3.
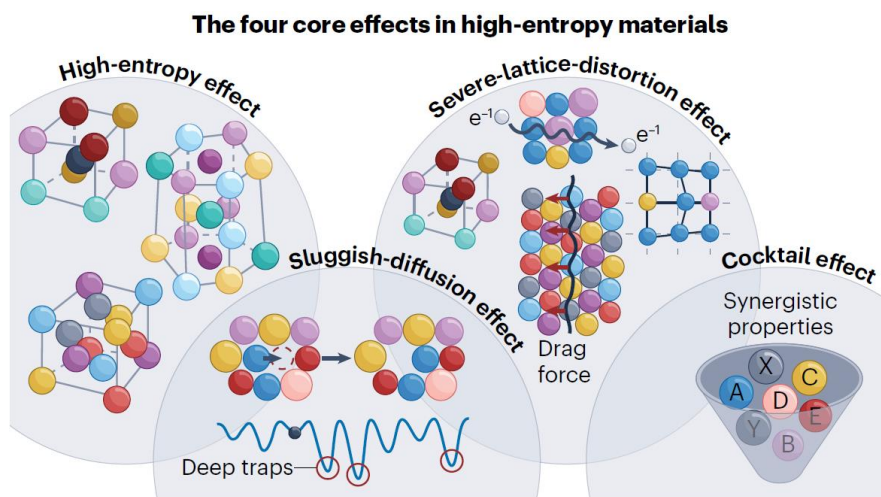
Figure 2.3 Illustration of high entropy materials four core effects [72].

2.4.1   High Entropy Ceramics

High entropy materials were initially studied as alloys and then the scope of the topic was extended by applying the entropy stabilization methods to ceramic materials. For the ceramics, the configurational entropy equation which was given as Equation (2.7) is modified to the following formulation [67]:

$$\Delta S_{mix,\ conf} = -R\left[\left(\sum_{i=1}^{n} x_i\ ln\ x_i\right)_{cation} + \left(\sum_{j=1}^{m} x_j\ ln\ x_j\right)_{anion}\right] \tag{2.9}$$

In the equation, x_i and x_j stand for the molar fraction of the corresponding constituents located in the cation and anion places, R represents the ideal gas constant, and n and m are the number of constituents [67]. The prominent high entropy ceramic materials are oxides, carbides, nitrides, silicides, borides, fluorides, and sulfides. In high entropy ceramics, single phase materials are obtained by utilizing multiple equimolar cations [67,73,74].

Initially studied high entropy ceramics, high entropy oxides production methods are exemplified as flash sintering, pulsed electric current sintering, solid state sintering, carbothermal shocking, physical vapor deposition, mechanical alloying (ball milling), spray pyrolysis, solution combustion, reduction, and reverse coprecipitation. Although some differences can be for the different ceramics, the other high entropy ceramics may also be synthesized by these [75]. High entropy oxides are the leading ceramics and are reported to have attractive properties such as modifiable band gaps, good lithium ion conductance in elevated temperatures, and worthwhile dielectric properties [76]. Their crystal structure can be single phase rock salt, spinel, perovskite, and fluorite with equimolar multi cations [76,77]. High entropy oxides have been researched mostly as potential candidates for sodium ion battery cathodes [78], lithium ion battery anodes [79-84], oxygen evolution or reduction reaction electrocatalysts [83,85-87], and carbon dioxide conversion photocatalysts [88-90].

High entropy carbides are the other promising high entropy ceramics. They can be manufactured by high energy mechanical alloying of carbide powders and sintering under pressure. The sintering step can also include a carbothermic process to achieve single phase high entropy carbides. Graphite with pure metals may also be used as precursors in high energy ball milling process to synthesize them [91]. The leading properties of high entropy carbides are elevated hardness, corrosion and radiation resistance, and alterable thermal conduction capability [91-92]. They have been reported as effective in hindering thermal conduction compared to the corresponding carbides [93]. High entropy carbides are seen as potential candidates to find applications in extraordinary conditions such as extremely high temperatures, irradiation, heat flux, and mediums containing gases [94-95].

High entropy nitrides are a further example of high entropy ceramics. They are widely investigated as functional coatings and thin films, and deposited by magnetron sputtering, vacuum arc, or cathodic arc [96-100]. Besides these, bulk high entropy nitrides can be synthesized by a combination of combustion or ball milling with pulsed electric current sintering methods [101,102]. High entropy nitrides can show extremely high corrosion resistance [96,100], attracting hardness, strength, and toughness [97-102], improved hydrophobicity [98], elevated temperature stability [102], and inferior resistivity for electrochemical utilization [103].

Similar to other high entropy ceramics, high entropy silicides have also been studied. High entropy silicides are mainly synthesized by ball milling or thermal reduction processes followed by a sintering method [104]. They can benefit from elevated melting temperature, resistance to creep and oxidation, hardness and toughness, and lowered electrical and thermal conductions [104-107].

High entropy borides are similar ceramics to high entropy carbides. They can be prepared by high energy ball milling, arc melting, borothermal or boro/carbothermal reduction with sintering [94,108]. Thanks to high entropy borides capability of having ultimate hardness [108], great mechanical stability under elevated pressures [109], decreased thermal conduction, and high corrosion resistance, they are

important candidates in extraordinary conditions such as hypersonic aircraft, atomic reactors, or turbines [94,95,109].

High entropy fluorides are another class of high entropy ceramics, and can show rutile and perovskite structures [110]. They can be synthesized by high energy ball milling [110-113], hydrothermal process [112,113], and coprecipitation method [114]. High entropy fluorides have been investigated as oxygen evolution reaction electrocatalysts [110]. Owing to their high level of theoretic specific capacities and tailorable features, they also are studied as cathodes or anodes for lithium ion batteries [111,113]. Moreover, they could be prepared as optically transparent for specific applications [114].

2.4.2   High Entropy Sulfides

High entropy sulfides are one of the latest high entropy ceramics studied. Replacing their binary similitudes with high entropy sulfides has been evaluated to enhance performance for varied applications. For instance, metal sulfides have broad applications in electrochemistry thanks to their good specific capacities but their relatively lower stability can deteriorate their performance. High entropy sulfides are potential candidates to increase their stability and provide beneficial properties thanks to the inherent effects of the high entropy concept [115].

Modifying the electronic features of high entropy sulfides is easier than the high entropy oxides because sulfur elements p orbitals have more intersections and energy coupling with metals d orbitals [77]. Therefore, ease of electronic structural modifications, oxides relatively lower conductivity, and higher electronegativity values are the main reasons that high entropy sulfides to be researched [116].

One of the primary challenges of high entropy sulfides is the lack of manufacturing methods providing products having good characteristics with high efficiency. Most of the synthesizing routes contain several stages and sulfurization steps and require high temperature or pressure conditions. In addition, sulfides are more prone to

reactions than most of the other ceramic counterparts restricting to utilization of some production techniques [117]. Some of the reported high entropy sulfide production methods are pulse thermal decomposition or precursor decomposition [117,118], pressing under high temperature [115,119], high energy ball milling [74,120,121], cation exchange [122-124], solvothermal [125-128], thermal injection [129], and magnetron sputtering [130].

High entropy sulfides have been studied recently for potential applications as oxygen evolution or reduction reaction electrocatalysts [74,117,118,123,125-129], lithium or sodium ion battery electrodes [115,116,121], and lithium sulfur battery electrocatalysts [124].

In one of these studies, Yamamoto et al. [119] produced $(FeNiCoCuRu)S_2$, $(FeNiCoCuMn)S_2$, $(FeNiCoCuZn)S_2$, and $(FeNiCoCuCd)S_2$ high entropy sulfides by using a cubic press with different elevated pressures up to half of one thousand ton. The sulfides were obtained by a quenching process after they were sintered at nearly 1000 °C under these pressures. Although Breitung et al. [121] successfully achieved a single pyrite phase of $(FeNiCoCuMn)S_2$ high entropy sulfide by high energy ball milling, Yamamoto et al. [119] obtained mixed phases rather than a pyrite phase for each high entropy sulfide they synthesized except $(FeNiCoCuRu)S_2$. This showed the impact of the manufacturing process on single phase high entropy sulfide syntheses with the same elemental compositions. Pyrite is a superabundant mineral and the pyrite phase is also noted for iron disulfide (FeS_2) material having this structure. The pyrite structure having Pa-3 symbol and 205 number is frequent for disulfides and shown in Figure 2.4 [119].
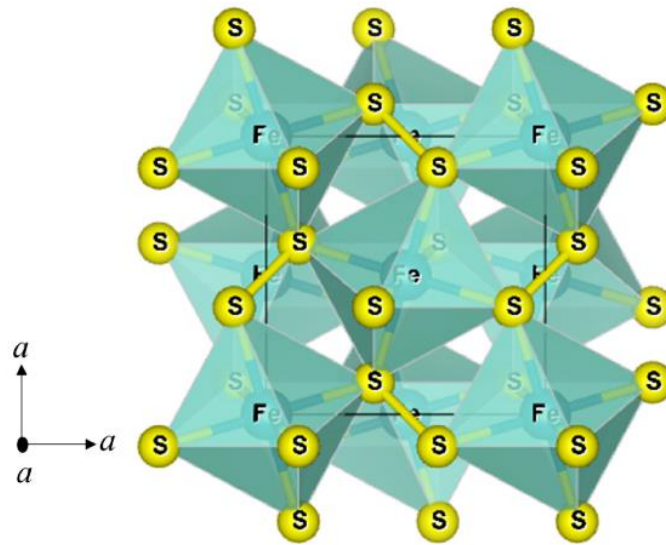
Figure 2.4. Representation of FeS_2 (pyrite) structure [119].

The study of Yamamoto et al. [119] showed that the method including a combination of sintering and cubic pressing could lead to $(FeNiCoCuRu)S_2$ high entropy sulfide with the pyrite type crystal structure. However, the substitution of Ru with other elements such as Mn, Zn, and Cd can cause multiple phases instead of a single pyrite phase showing the importance of the production parameters to achieve desired single phase high entropy sulfides.

In another high entropy sulfide study, Tang et al. [127] synthesized FeNiCoCrCu sulfides by a multistep solvothermal method. Firstly, they prepared a layered metal hydroxide by solvothermal method using Teflon lined stainless steel autoclave at 80 °C for 2 days. Then, the prepared hydroxide was sulfurized by another solvothermal process utilizing thioacetamide as the sulfurizing agent. The sulfurization process was performed at 100 °C for half a day. The surface of the sulfide was hydroxylated, and the structure of the obtained high entropy sulfide was reported as $(FeNiCoCrCu).xH_2O$. The high entropy material performed as a great pre-catalyst and the oxygen evolution reaction activity was increased.

Although the number of available studies is limited for the applications of high entropy sulfides as a part of batteries, there has also been some recent research in this area. Breitung et al. [121] utilized different metal sulfides and metal powders as

precursors and synthesized various equimolar, single phase high entropy sulfides by high energy ball milling. They successfully obtained $(FeNiTiCrMn)S_2$, $(FeNiCoCuMn)S_2$, $(FeNiCoCrMn)S_2$ having a single pyrite phase, and $(FeNiCoCrMn)S$ with an orthorhombic structure. In contrast, $(FeNiCoCrMn)_2S_3$, $(FeNiCoCrMn)_3S_4$, $(FeNiCoCrMn)_3S_2$, and $(FeNiTiCrMn)S$ showed multiphase rather than a single pyrite or orthorhombic phase. The synthesized high entropy sulfides were studied as lithium ion battery electrodes and they gave elevated specific capacities. Their specific capacities were better than both conventional sulfides and medium entropy counterparts having less than 5 equimolar atoms.

In addition to Bretiung et al. [121], Gou et al. [115] and Fu et al. [116] also studied high entropy sulfides utilization as lithium ion and sodium ion battery electrodes. Gou et al. [115] synthesized $(FeNiCoCuRu)S_2$ having a pyrite structure under high pressure and temperature using a cubic press. The prepared high entropy sulfide showed excellent specific capacities and structural stabilities. Fu et al. [116], on the other hand, used density functional theory to see the effect of lithium doping on $Na(MnFeCoNi)_{1/2}S$. Their theoretical calculations showed that lithium doping can increase structural stability and enhance the electrochemical performance of sodium ion battery cathodes.

CHAPTER 3

EXPERIMENTAL PROCEDURES

The experimental procedures and methods chapter is divided into two synthesis methods of different high entropy sulfides used in the thesis. Used materials, characterization, and test methods are explained in the chapter for each of these methods.

3.1   Solvothermal Method

High entropy $(FeNiCoCrMn)S_x \cdot aH_2O$ sulfide material was synthesized by a multistep solvothermal method. The high entropy sulfide was obtained from an as-synthesized layered metal hydroxide.

3.1.1   Materials

The chemicals utilized in the solvothermal method are given below. The materials were used in the experiments as bought from Sigma Aldrich (purity ≥ 99 %) without any process.

Ferric nitrate nonahydrate $[Fe(NO_3)_3 \cdot 9H_2O]$, nickel dinitrate hexahydrate $[Ni(NO_3)_2 \cdot 6H_2O]$, cobaltous nitrate hexahydrate $[Co(NO_3)_2 \cdot 6H_2O]$, chromium trinitrate nonahydrate $[Cr(NO_3)_3 \cdot 9H_2O]$, manganese dinitrate tetrahydrate $[Mn(NO_3)_2 \cdot 4H_2O]$, ethyl alcohol (CH_3CH_2OH), sodium carbonate (Na_2CO_3), sodium hydroxide $(NaOH)$, thioacetamide (CH_3CSNH_2).

3.1.2 Synthesis of (FeNiCoCrMn)S$_x$.aH$_2$O High Entropy Sulfide from Layered Metal Hydroxide

For synthesizing layered metal hydroxide, two separate solutions were prepared. To prepare the first solution, 0.004 moles of Fe(NO$_3$)$_3$ · 9H$_2$O, Ni(NO$_3$)$_2$ · 6H$_2$O, Co(NO$_3$)$_2$ · 6H$_2$O, Cr(NO$_3$)$_3$ · 9H$_2$O, and Mn(NO$_3$)$_2$ · 4H$_2$O were dissolved in 40 mL deionized water. The second solution was prepared by dissolution of Na$_2$CO$_3$ and NaOH in 40 mL of deionized water. The molar amounts were 0.032 and 0.078 mol, respectively. While preparing these solutions, both of them were magnetically stirred under 300 rpm. Then, the second solution was transferred to the first one by a micropipette slowly and stirred continuously for half an hour under 700 rpm. The final solution was poured into a 100 mL Teflon lined hydrothermal autoclave and held for two days at 80 °C. After the autoclave process was completed and the reactor cooled, the layered metal hydroxide powder product was centrifuged and cleaned three times with deionized water and two times with ethyl alcohol, each for 800 rpm and 5 minutes. Then, the final product was dried in a desiccator under vacuum.

To synthesize high entropy sulfide, a solution was prepared by dispersion of 1 g of the obtained high entropy layered metal hydroxide powder in 80 mL deionized water, and the addition of 7.513 g thioacetamide. The final solution was continuously stirred for half an hour and poured into the 100 mL Teflon lined hydrothermal autoclave. After holding it for half a day at 100 °C, the final high entropy sulfide powder was obtained. Following the cooling of the reactor, the powder was centrifuged and cleaned three times with deionized water at 9000 rpm for 30 minutes, and two times with ethyl alcohol at 9000 rpm for 20 minutes. The solvothermal methodology shown in Figure 3.1 was repeated three times to achieve the minimum powder amount necessary to be able to perform the following electrochemical tests.
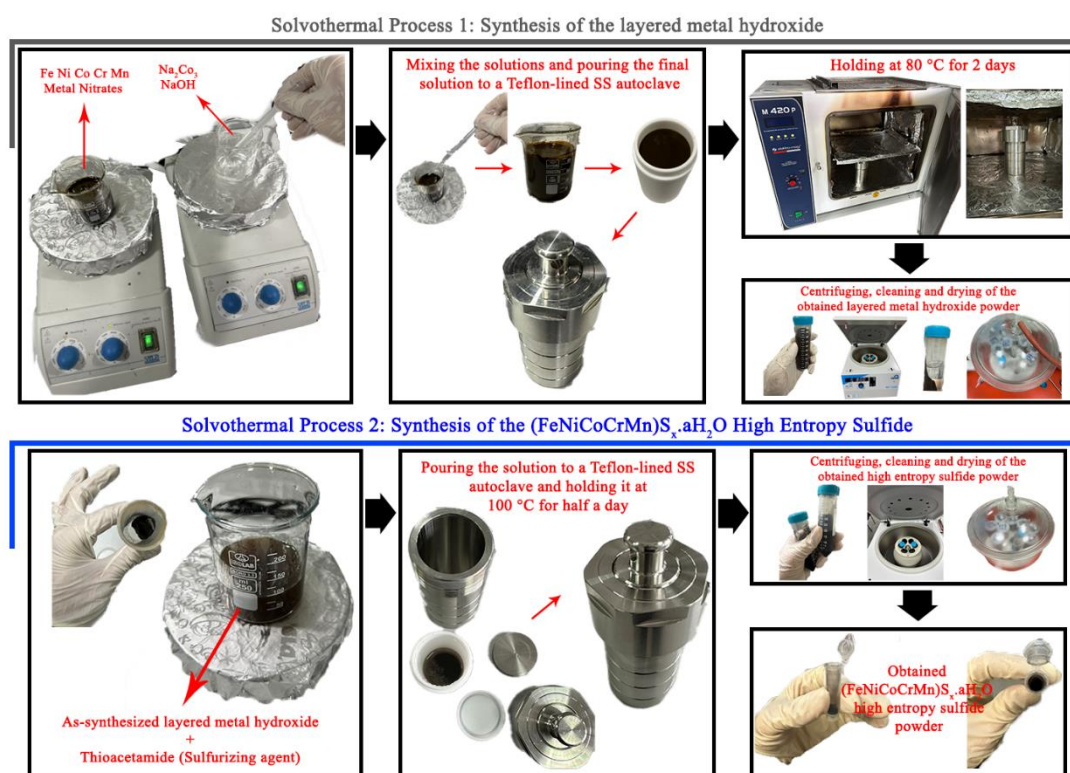
Figure 3.1. The solvothermal methodology performed to prepare
$(FeNiCoCrMn)S_x.aH_2O$ high entropy sulfide.

3.1.3 Characterization of the Synthesized $(FeNiCoCrMn)S_x.aH_2O$ High Entropy Sulfide Powder

Powder X-ray diffraction (XRD) was utilized to determine the crystal structures of the prepared $(FeNiCoCrMn)S_x.aH_2O$ powders. XRD was conducted between 2θ values of $20°$ and $90°$ at ambient temperature utilizing Cu-Kα radiation (wavelength of 1.5406 Å). Inductively coupled plasma optical emission spectroscopy (ICP-OES) was used to determine the elemental compositions of the synthesized high entropy disulfides. Thermogravimetric analysis (TGA) was conducted to examine the thermal stabilities of the samples.

3.1.4   Preparation of Thermal Battery Single Cell Components

As-synthesized $(FeNiCoCrMn)S_x.aH_2O$ high entropy sulfides were dried at 120 °C under a dynamic vacuum for 2 hours. Different types of cathode pellets containing $(FeNiCoCrMn)S_x.aH_2O$ and conventional FeS_2 (pyrite) as active materials were prepared for thermal battery single cell tests. Since a pellet thickness variation of nearly 0.2 mm was observed when $(FeNiCoCrMn)S_x.aH_2O$ and pyrite powders compacted with the same powder weights, two different types of pyrite pellets were prepared. One of the pyrite pellets was prepared with equal weight, and the other one was prepared with equal thickness as compared with the high entropy sulfide pellets. For synthesizing $(FeNiCoCrMn)S_x.aH_2O$ and equal weight pyrite pellets, 0.33 g cathode active material, 0.20 g LiF-LiCl-LiBr salt, and 0.13 g MgO were mixed in an agate mortar and sieved using a test sieve having a 150 μm mesh size. For synthesizing equal thickness pyrite pellets, 0.54 g cathode active material, 0.32 g LiF-LiCl-LiBr salt, and 0.22 g MgO were mixed in an agate mortar and sieved by using a test sieve having a 150 μm mesh size. All of the powder mixtures were distributed in a die with a 30 mm diameter and pressed utilizing a force of 20 tons as shown in Figure 3.2. The obtained pellets with 30 mm diameter were sliced into the final cathode pellets with 13 mm diameter under static pressure.

Figure 3.2. Preparing of the $(FeNiCoCrMn)S_x.aH_2O$ pellets with 30 mm diameter.

Li-Si anode pellets and separator pellets, containing LiF-LiCl-LiBr as eutectic salt and MgO as binder, were sliced into pellets with 13 mm diameter from as-compacted wafers with 30 mm diameter.

All of the single cell component preparation steps and compaction of the powders to pellets were conducted in a dry room having a relative humidity (RH) of less than 1% because of the hygroscopicity of some of the raw materials.

The average weights and thicknesses of the anode, separator, and cathode pellets used in the experiments are given in Table 3.1.

Table 3.1 Properties of the prepared thermal battery single cell components.

Single Cell Component	Weight (g)	Thickness (mm)
Anode Pellet (Li-Si alloy)	0.07	0.53
Separator Pellet (LiF-LiCl-LiBr and MgO)	0.13	0.42
Cathode Pellet with (FeNiCoCrMn)S_x.aH_2O	0.65	0.44
Cathode Pellet with conventional FeS_2 (Equal weight)	0.65	0.27
Cathode Pellet with conventional FeS_2 (Equal thickness)	1.08	0.44

3.1.5 Electrochemical Tests

In the electrochemical single cell tests, as-prepared anode, separator, and cathode pellets with 13 mm diameter were stacked between two nickel current collectors. Then, the assembled cell was inserted at the center of two pressure plates, which had the ability to apply constant temperature and pressure. Utilizing this testing method, a programmable electronic load with one channel was employed to discharge the cells in a dry room with a RH of less than 1%. Photos of the single cells before and after discharging are given in Figure 3.3.
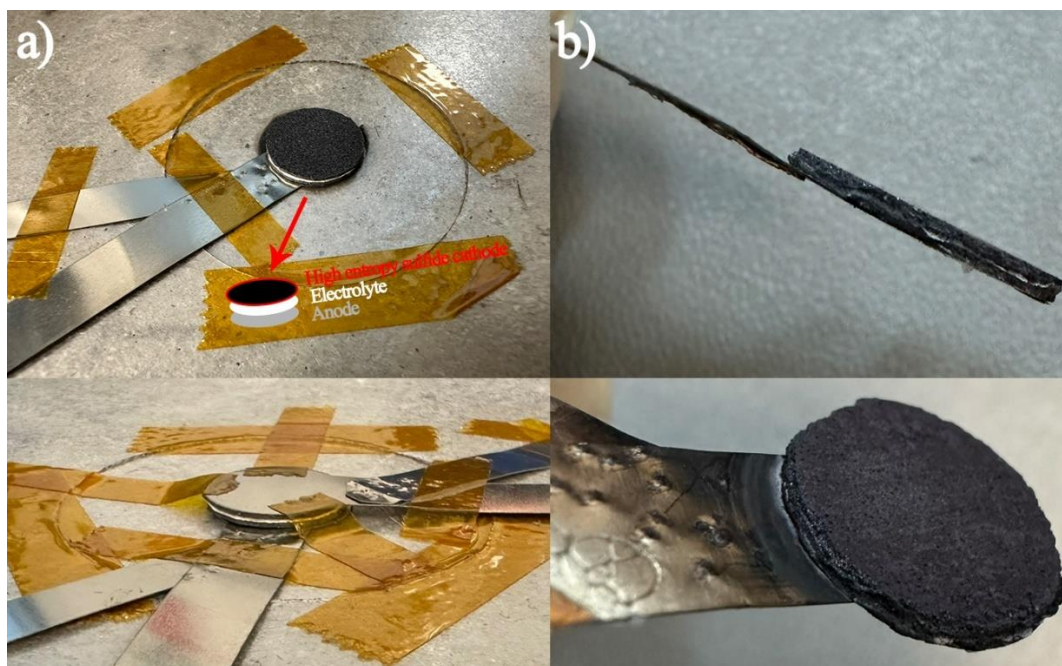
Figure 3.3. Photos of the single cells containing $(FeNiCoCrMn)S_x.aH_2O$ high entropy sulfide cathode (a) before and (b) after discharging.

Representation of the electrochemical single cell testing mechanism and the test parameters applied in the experiments are given in Figure 3.4 and Table 3.2, respectively.

Figure 3.4. Electrochemical single cell testing mechanism.

Table 3.2 Electrochemical single cell test parameters of $(FeNiCoCrMn)S_x.aH_2O$.

Cathode Active Material	Temperature (°C)	Applied Force (kg)	Current Profile
$(FeNiCoCrMn)S_x.aH_2O$	475 525	3	Constant load of 0.24 A (0.18 A/cm^2), and a pulse load of 1 A (0.75 A/cm^2) for 100 ms every 3 seconds
Conventional FeS$_2$ (equal weight)	475		
Conventional FeS$_2$ (equal thickness)	475		

3.2   High Energy Ball Milling Method

3.2.1   Materials and Equipments

Iron disulfide (FeS_2), nickel sulfide (Ni_3S_2), cobalt disulfide (CoS_2), chromium (Cr), manganese(II) sulfide (MnS), copper(II) sulfide (CuS), titanium(IV) sulfide (TiS_2), and sulfur (S) powders were utilized in the ball milling method. The metal sulfide and metal powders were used in the experiments (purity $\geq 99\%$) without any process.

The high energy ball milling processes were conducted in a planetary ball mill machine (Retsch PM400) using tungsten carbide (WC) vials and balls. The vial capacities were 50 mL and the balls diameters were 5 mm and 7 mm.

3.2.2   Synthesis of (FeNiCoCrMn)S$_2$ High Entropy Disulfides

(FeNiCoCrMn)S_2 high entropy sulfides were synthesized by high energy ball milling. FeS_2, Ni_3S_2, CoS_2, Cr, MnS, and S powders were mixed in an argon-filled glove box having H_2O and O_2 below 10 ppm and 5 ppm, respectively. The powders were mixed regarding stoichiometric ratios to achieve a 1:2 metal to sulfur atomic ratio with equimolar transition metals. The weight ratio of powder mix to WC balls was 1:40, and WC balls having 5 mm and 7 mm diameters were used in two different vials. After the mixing was completed, between the vials and the cap of the vials were sealed with Teflon tape in the glove box and the vials were transferred to the planetary high energy ball mill machine. They were ball milled at 300 rpm for 120 hours. The representation of the ball milling procedure performed to synthesize (FeNiCoCrMn)S_2 high entropy sulfides is shown in Figure 3.5.

Figure 3.5. Ball milling procedure performed to synthesize $(FeNiCoCrMn)S_2$ high entropy sulfides.

3.2.3 Characterization of the Synthesized $(FeNiCoCrMn)S_2$ High Entropy Disulfide Powders

Powder XRD was utilized to determine the crystal structures of the prepared $(FeNiCoCrMn)S_2$ powders. XRD was conducted between 2θ values of $10°$ and $80°$ at ambient temperature utilizing Cu-Kα radiation (wavelength of 1.5406 Å). The XRD analysis was conducted for as-prepared mixtures and ball milled mixtures for 35 hours, 85 hours, and 120 hours. The XRD analysis was also performed after the

discharge of the single cells to evaluate the post-discharge products. The sampling for XRD analyses was performed in an argon-filled glove box having H_2O and O_2 below 10 ppm and 5 ppm, except for the XRD analysis of post-discharge. The Rietveld refinement of the obtained patterns was executed using the GSAS software. High-resolution transmission electron microscopy (HRTEM) was also conducted to further investigate of the structural properties of the prepared high entropy disulfide powders. ICP-OES was used to determine the elemental compositions of the synthesized high entropy disulfides. The prepared high entropy sulfides chemical compositions on the surface and the oxidation numbers were investigated by X-ray photoelectron spectroscopy (XPS). TGA was conducted to examine the thermal stabilities of the samples. Scanning electron microscopy (SEM) analyses were performed to inspect the structural and morphological details of the materials.

3.2.4   Preparation of Thermal Battery Single Cell Components

As-prepared $(FeNiCoCrMn)S_2$ high entropy sulfides were divided into two categories $(FeNiCoCrMn)S_2 - 5$ mm and $(FeNiCoCrMn)S_2 - 7$ mm based on the size of the WC balls used in high energy ball milling process. The synthesized high entropy sulfides were dried at 120 °C under a dynamic vacuum for 2 hours. Three different types of cathode pellets containing $(FeNiCoCrMn)S_2 - 5$ mm, $(FeNiCoCrMn)S_2 - 7$ mm, and conventional FeS_2 (pyrite) as active materials were prepared for thermal battery single cell tests. Firstly, 0.55 g cathode active material, 0.33 g LiF-LiCl-LiBr salt, and 0.22 g MgO were mixed in an agate mortar and sieved by using a test sieve having a 150 μm mesh size. The mixture was distributed in a die with a 40 mm diameter and pressed utilizing a force of 40 tons as shown in Figure 3.6. The obtained pellets with 40 mm diameter were sliced into the final cathode pellets with 13 mm diameter under static pressure.
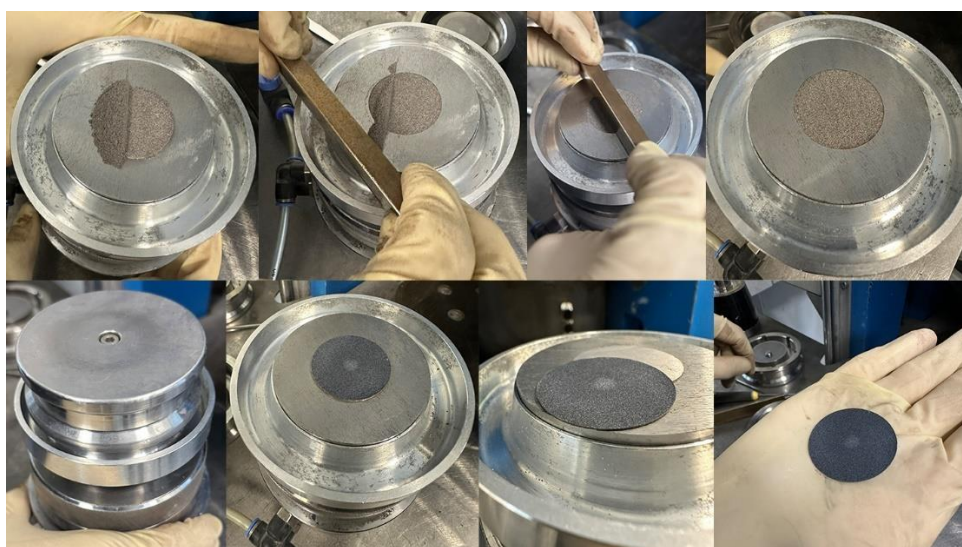
Figure 3.6. Preparing of the (FeNiCoCrMn)S$_2$ pellets with 40 mm diameter.

Li-Si anode pellets and separator pellets, containing LiF-LiCl-LiBr as eutectic salt and MgO as binder, were sliced into pellets with 13 mm diameter from as-compacted wafers with 40 mm diameter.

All of the single cell component preparation steps and compaction of the powders to pellets were conducted in a dry room having a RH of less than 1% because of the hygroscopicity of some of the raw materials.

The average weights and thicknesses of the anode, separator, and cathode pellets are given in Table 3.3.

Table 3.3 Properties of the prepared thermal battery single cell components.

Single Cell Component	Weight (g)	Thickness (mm)
Anode Pellet (Li-Si alloy)	0.06	0.43
Separator Pellet (LiF-LiCl-LiBr and MgO)	0.11	0.34
Cathode Pellet with $(FeNiCoCrMn)S_2$ – 5 mm	0.12	0.34
Cathode Pellet with $(FeNiCoCrMn)S_2$ – 7 mm	0.12	0.33
Cathode Pellet with conventional FeS_2 (pyrite)	0.12	0.32

3.2.5 Electrochemical Tests

In the electrochemical single cell tests, as-prepared anode, separator, and cathode pellets were stacked between two Nickel current collectors as shown in Figure 3.7.

Figure 3.7. The single cells containing $(FeNiCoCrMn)S_2$ high entropy disulfide cathode.

Then, the assembled cell was inserted at the center of two pressure plates, which had the ability to apply constant temperature and pressure. Utilizing this testing method, a programmable electronic load with one channel was employed to discharge the cells in a dry room with a RH of less than 1%. Representation of the electrochemical single cell testing mechanism and the test parameters applied in the experiments are given in Figure 3.4 and Table 3.4, respectively.
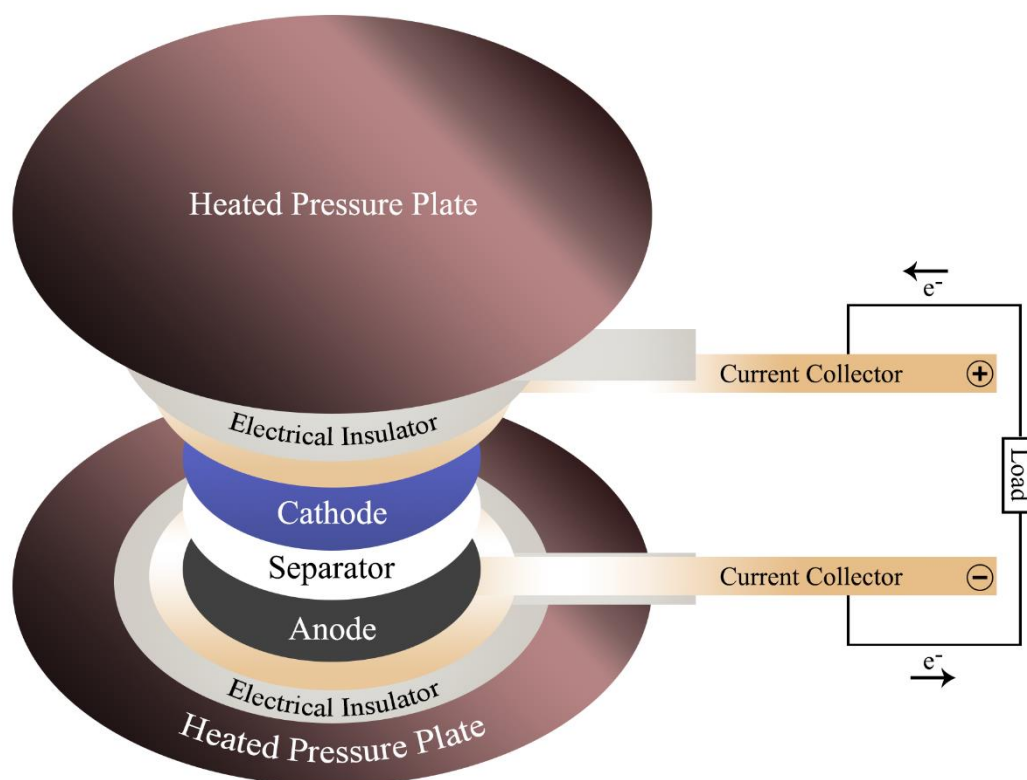
Table 3.4 Electrochemical single cell test parameters.

Cathode Active Material	Temperature (°C)	Applied Force (kg)	Current Profile
(FeNiCoCrMn)S_2-5 mm	475		
	525		
	575		Constant load of
(FeNiCoCrMn)S_2-7 mm	475		0.24 A (0.18 A/cm^2),
	525	3	and a pulse load of
	575		1 A (0.75 A/cm^2) for
Conventional FeS_2 (pyrite)	475		100 ms every 3 seconds
	525		
	575		

3.2.6 Synthesis of (FeNiCoCuTi)S_2 and (FeNiCo$_{0.35}$CrMn)S_2 High Entropy Disulfides

(FeNiCoCuTi)S_2 and (FeNiCo$_{0.35}$CrMn)S_2 high entropy sulfides were also synthesized by high energy ball milling. For preparing (FeNiCoCuTi)S_2 high entropy disulfide powder, FeS_2, Ni_3S_2, CoS_2, CuS, TiS_2, and S powders were mixed in an argon-filled glove box having H_2O and O_2 below 10 ppm and 5 ppm, respectively. (FeNiCo$_{0.35}$CrMn)S_2, on the other hand, was synthesized by mixing FeS_2, Ni_3S_2, CoS_2, Cr, MnS, and S powders with the same process conditions. The powders were mixed regarding stoichiometric ratios to achieve a 1:2 metal to sulfur atomic ratio. Although equimolar transition metals were used when the powders were mixed to synthesize (FeNiCoCuTi)S_2, more CoS_2 content was used relative to other transition metals in preparing (FeNiCo$_{0.35}$CrMn)S_2 to achieve the designed molar ratios. The weight ratio of powder mix to WC balls was 1:40, and WC balls having 5 mm and 7 mm diameters were used in two different vials. The balls with 5 mm diameter were

43

used to prepare $(FeNiCo_{0.35}CrMn)S_2$ and 7 mm diameter were used to $(FeNiCoCuTi)S_2$. After the mixing was completed, between the vials and the cap of the vials were sealed with Teflon tape in the glove box and the vials were transferred to the planetary high energy ball mill machine. They were ball milled at 300 rpm for 120 hours. The ball milling procedure was the same as preparing $(FeNiCoCrMn)S_2$ high entropy disulfides explained and represented in Figure 3.5.

3.2.7 Characterization of the Synthesized $(FeNiCoCuTi)S_2$ and $(FeNiCo_{0.35}CrMn)S_2$ High Entropy Disulfide Powders

Powder XRD was utilized to determine the crystal structures of the prepared $(FeNiCoCuTi)S_2$ and $(FeNiCo_{0.35}CrMn)S_2$ powders. XRD was conducted between 10° and 80° 2θ values at ambient temperature by utilizing Cu-Kα radiation (1.5406 Å). The XRD analysis was conducted for as-prepared mixtures and ball milled mixtures for 35 hours, 85 hours, and 120 hours. The XRD analysis was also performed after the discharge of the single cells to evaluate the post-discharge products. The sampling for XRD analyses was performed in an argon-filled glove box having H_2O and O_2 below 10 ppm and 5 ppm, except for the XRD analysis of post-discharge. The Rietveld refinement of the obtained patterns was executed using the GSAS software. ICP-OES was used to determine the elemental compositions of the synthesized high entropy disulfides. The prepared high entropy sulfides chemical compositions on the surface and the oxidation numbers were investigated by XPS. TGA was conducted to examine the thermal stabilities of the samples. SEM analyses were performed to inspect the structural and morphological details of the materials. High-resolution transmission electron microscopy was also conducted to further investigate of the morphological and structural properties of the prepared high entropy disulfide powders.

3.2.8   Preparation of Thermal Battery Single Cell Components

The synthesized $(FeNiCoCuTi)S_2$ and $(FeNiCo_{0.35}CrMn)S_2$ high entropy sulfides were dried at 120 °C under a dynamic vacuum for 2 hours. Three different types of cathode pellets containing $(FeNiCoCuTi)S_2$, $(FeNiCo_{0.35}CrMn)S_2$, and reference FeS_2 (pyrite) as active materials were prepared for thermal battery single cell tests. Firstly, 0.55 g cathode active material, 0.33 g LiF-LiCl-LiBr salt, and 0.22 g MgO were mixed in an agate mortar and sieved by using a test sieve having a 150 μm mesh size. The mixture was distributed in a die with a 40 mm diameter and pressed utilizing a force of 40 tons as previously shown in Figure 3.6. The obtained pellets with 40 mm diameter were sliced into the final cathode pellets with 13 mm diameter under static pressure.

Li-Si anode pellets and separator pellets, containing LiF-LiCl-LiBr as eutectic salt and MgO as binder, were sliced into pellets with 13 mm diameter from as-compacted wafers with 40 mm diameter.

All of the single cell component preparation steps and compaction of the powders to pellets were conducted in a dry room having a RH of less than 1% because of the hygroscopicity of some of the raw materials.

The average weights and thicknesses of the anode, separator, and cathode pellets are given in Table 3.5.

Table 3.5 Properties of the prepared thermal battery single cell components.

Single Cell Component	Weight (g)	Thickness (mm)
Anode Pellet (Li-Si alloy)	0.06	0.43
Separator Pellet (LiF-LiCl-LiBr and MgO)	0.11	0.34
Cathode Pellet with $(FeNiCoCuTi)S_2$	0.12	0.33
Cathode Pellet with $(FeNiCo_{0.35}CrMn)S_2$	0.12	0.34
Cathode Pellet with conventional FeS_2 (pyrite)	0.12	0.32

3.2.9　Electrochemical Tests

In the electrochemical single cell tests, as-prepared anode, separator, and cathode pellets were stacked between two Nickel current collectors as previously shown in Figure 3.7. Then, the assembled cell was inserted at the center of two pressure plates, which had the ability to apply constant temperature and pressure. Utilizing this testing method, a programmable electronic load with one channel was employed to discharge the cells in a dry room with a RH of less than 1%. The whole procedure and testing setup was same as the tests of $(FeNiCoCrMn)S_x.aH_2O$ and $(FeNiCoCrMn)S_2$ high entropy sulfides which was represented in Figure 3.4. The test parameters applied in the electrochemical single cell discharge tests of $(FeNiCoCuTi)S_2$ and $(FeNiCo_{0.35}CrMn)S_2$ sulfides are given in Table 3.6.

Table 3.6 Electrochemical single cell test parameters.

Cathode Active Material	Temperature (°C)	Applied Force (kg)	Current Profile
$(FeNiCoCuTi)S_2$	475		
	525		
	575		Constant load of
$(FeNiCo_{0.35}CrMn)S_2$	475		0.24 A $(0.18$ A/cm$^2)$,
	525	3	and a pulse load of
	575		1 A $(0.75$ A/cm$^2)$ for
Conventional FeS$_2$ (pyrite)	475		100 ms every 3 seconds
	525		
	575		

After the electrochemical discharge tests, the internal resistance of the single cells was calculated by the following formula [30, 36]:

$$R_{single\ cell} = \frac{(V_1 - V_2)}{(I_2 - I_1)} \qquad (3.1)$$

In the Equation (3.1), $R_{single\ cell}$, V_1, V_2, I_1, and I_2 are the internal resistance of the cell (Ω), baseload voltage (V), pulse voltage (V), baseload current (A), and pulse current (A), respectively.

The specific capacity and energy values of the cells were also calculated for further investigation of the electrochemical performances according to given formulas:

$$C = \frac{I \times t}{m} \qquad (3.2)$$

$$\mathcal{E} = \frac{\int V\,I\,dt}{m} \qquad (3.3)$$

where C, I, t, m, $\mathcal{E}$, and V are specific capacity (mAh g^{-1}), discharge current (mA or A), discharge time (h), mass of cathode active material (g or kg), specific energy (Wh kg^{-1}), and discharge voltage (V), respectively.

CHAPTER 4

RESULTS and DISCUSSION

The electrochemical discharge characteristics of high entropy sulfides synthesized by the solvothermal methodology and the high energy ball milling process were particularly examined. Since high entropy disulfides prepared by ball milling were substantially more promising, further investigations on the properties were performed in more depth for these disulfides rather than the solvothermally synthesized high entropy sulfide. The high entropy disulfides were characterized by XRD, ICP-OES, XPS, TGA, SEM, and TEM. Their electrochemical performances as thermal battery cathode materials were investigated by single cell tests. Regarding these tests, their specific capacities, specific energies, and internal resistances were examined in comparison with FeS_2, a conventional thermal battery cathode.

4.1 Analyses of the Crystal Structures of the High Entropy Sulfides

Crystal structures of the $(FeNiCoCrMn)S_x.aH_2O$ obtained by solvothermal method and $(FeNiCoCrMn)S_2$ prepared by mechanochemical approach are investigated separately based on the applied powder XRD characterization technique.

4.1.1 Phase Structure of the $(FeNiCoCrMn)S_x.aH_2O$ High Entropy Sulfide Synthesized by Solvothermal Method

Powder XRD patterns of the $(FeNiCoCrMn)S_x.aH_2O$ samples obtained from three production cycles are given in Figure 4.1.
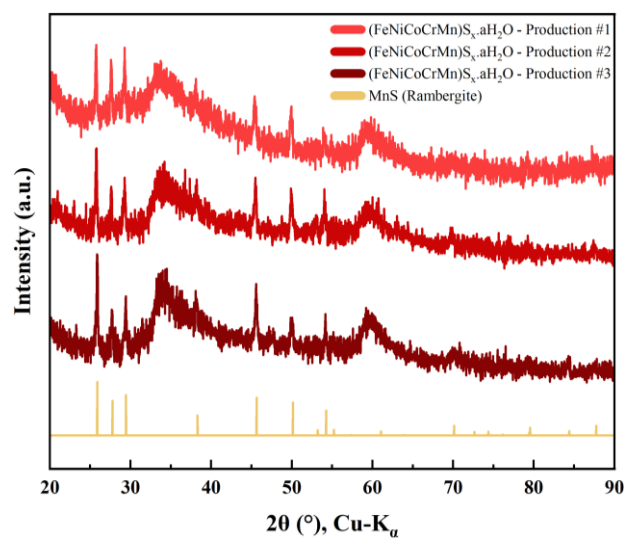
Figure 4.1. XRD patterns of the synthesized $(FeNiCoCrMn)S_x.aH_2O$ powders.

Based on the XRD patterns, the synthesized high entropy sulfide phase is ascribed to the MnS phase with P6(3)mc space group. However, the obtained material is not only a single phase sulfide but also some undesired additional peaks are present. These additional peaks may be attributed to lattice water, hydroxyl groups, or other oxides that can be formed in topotactic solvothermal routes [127].

4.1.2 Phase Structure of the High Entropy Disulfides Prepared By High Energy Ball Milling

4.1.2.1 Phase Structure of the $(FeNiCoCrMn)S_2$ High Entropy Disulfides

Powder XRD patterns of the synthesized $(FeNiCoCrMn)S_2$ – 5 mm and $(FeNiCoCrMn)S_2$ – 7 mm high entropy sulfides are given in Figure 4.2 and Figure 4.3, respectively. They are categorized according to the diameters of the WC balls utilized in their mechanochemical preparation route and they were characterized at 35 hours, 85 hours, and 120 hours high energy ball milling periods. Their mixtures were also characterized before the ball milling procedure. Sample obtaining was completed in an argon-filled glove box having H_2O and O_2 below 10 ppm and 5 ppm for the XRD experiments.

50

Figure 4.2. XRD patterns of 35 hours, 85 hours, and 120 hours ball milled (FeNiCoCrMn)S₂ – 5 mm high entropy disulfide.

Figure 4.3. XRD patterns of 35 hours, 85 hours, and 120 hours ball milled (FeNiCoCrMn)S₂ – 7 mm high entropy disulfide.

Powder XRD results indicate that each of the high entropy sulfides has a single pyrite phase. However, there are also small WC impurities arising from the high energy ball milling process. Although the hardness of WC balls is quite higher than most of the milling ball counterparts, high rpm values with extremely high milling times in planetary ball milling procedures lead to small amount of impurities, unavoidably [121,131,132]. Broad peaks observed in the XRD analyses are attributed to the small particle sizes of the materials.

The details of the crystal structures and lattice parameters of high entropy sulfides were examined using Rietveld refinements. The refinements were performed under the assumption that the cations are uniformly distributed within the pyrite structure. The results of the refinements, given in Figure 4.4, revealed that both (FeNiCoCrMn)S_2 – 5 mm and (FeNiCoCrMn)S_2 – 7 mm high entropy sulfides have single pyrite structures without including another phase except a small amount of WC impurity.
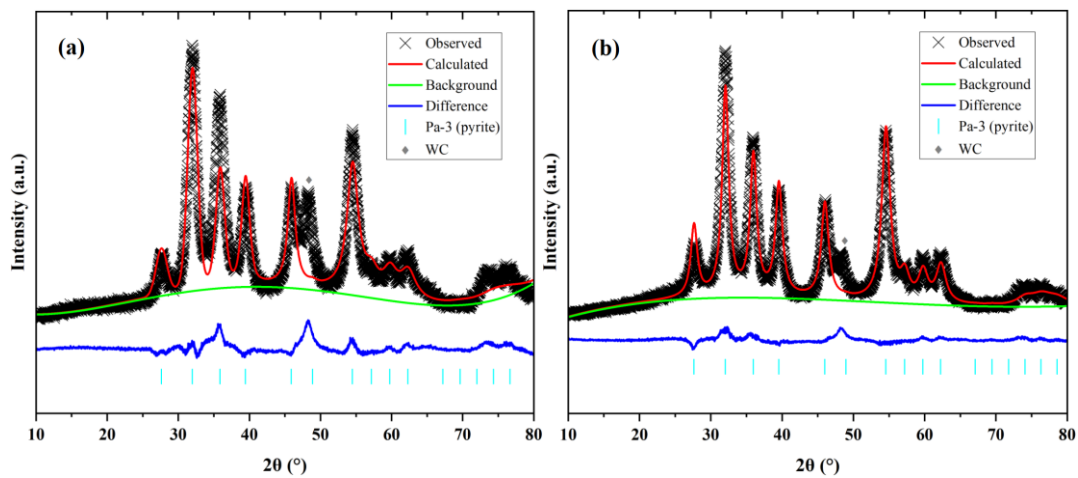
Figure 4.4. Rietveld refinement results of a) (FeNiCoCrMn)S_2 – 5 mm and b) (FeNiCoCrMn)S_2 – 7 mm high entropy disulfides.

The formed high entropy pyrite structures with Pa-3 space group display lattice constants (a) as 5.451 Å and 5.578 Å, respectively. The refinement results are given in detail in Table 4.1.

Table 4.1 Lattice parameters of $(FeNiCoCrMn)S_2$ – 5 mm and $(FeNiCoCrMn)S_2$ –
7 mm high entropy disulfides obtained from Rietveld refinement.

High Entropy Sulfide	Space Group	a (Å)	Unit Cell Volume (Å³)
$(FeNiCoCrMn)S_2$ – 5 mm	Pa-3	5.451	161.972
$(FeNiCoCrMn)S_2$ – 7 mm	Pa-3	5.578	173.564

In addition, the crystal structures of the $(FeNiCoCrMn)S_2$ – 5 mm and $(FeNiCoCrMn)S_2$ – 7 mm high entropy disulfides were further investigated by HRTEM and SAED. As shown in Figure 4.5(a) and Figure 4.6(a), the selected areas are attributed to (200) lattice planes of the FeS_2 structure for $(FeNiCoCrMn)S_2$ – 5 mm and $(FeNiCoCrMn)S_2$ – 7 mm with the measured lattice spacings nearly of 0.27 nm and 0.28 nm, respectively. SAED patterns given in Figure 4.5(b) and Figure 4.6(b) show that the diffraction rings match that of the pyrite structure and the lattice spacing measurements from these patterns are compatible with the XRD and Rietveld refinement results.
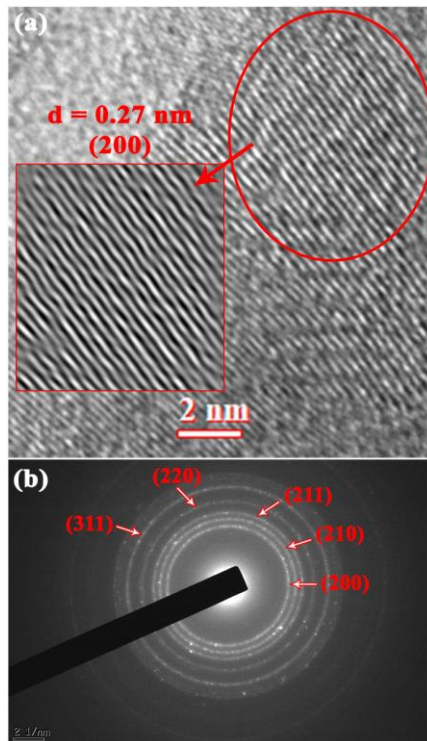
Figure 4.5 HRTEM image (a) and SAED pattern (b) of $(FeNiCoCrMn)S_2$ – 5 mm
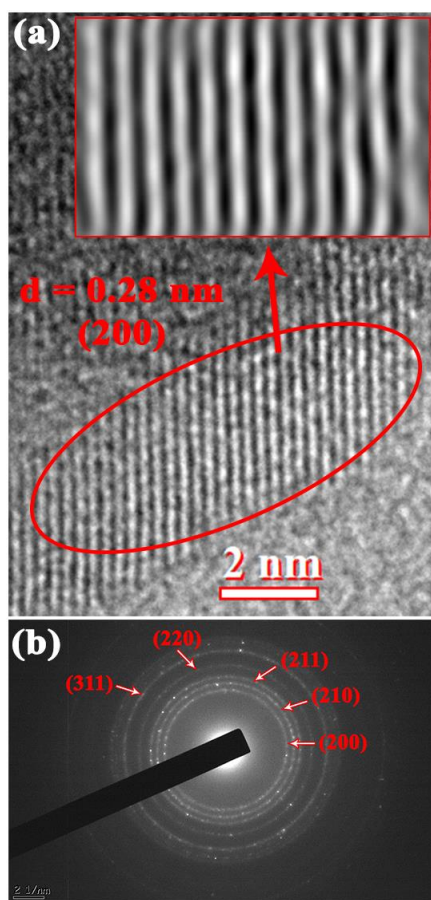
Figure 4.6 HRTEM image (a) and SAED pattern (b) of $(FeNiCoCrMn)S_2 - 7$ mm.

4.1.2.2 Phase Structure of the $(FeNiCoCuTi)S_2$ and $(FeNiCo_{0.35}CrMn)S_2$ High Entropy Disulfides

Powder XRD patterns of the synthesized $(FeNiCoCuTi)S_2$ and $(FeNiCo_{0.35}CrMn)S_2$ high entropy sulfides are given in Figure 4.7 and Figure 4.8, respectively. They were characterized at 35 hours, 85 hours, and 120 hours high energy ball milling periods. Their mixtures were also characterized before the ball milling procedure. Sample obtaining was completed in an argon-filled glove box having H_2O and O_2 below 10 ppm and 5 ppm for the XRD experiments.
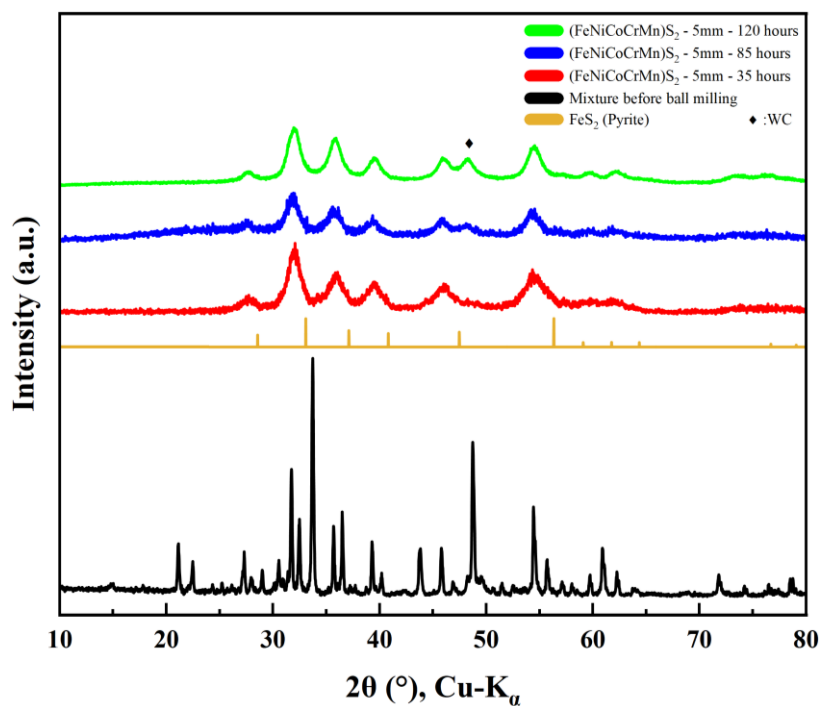
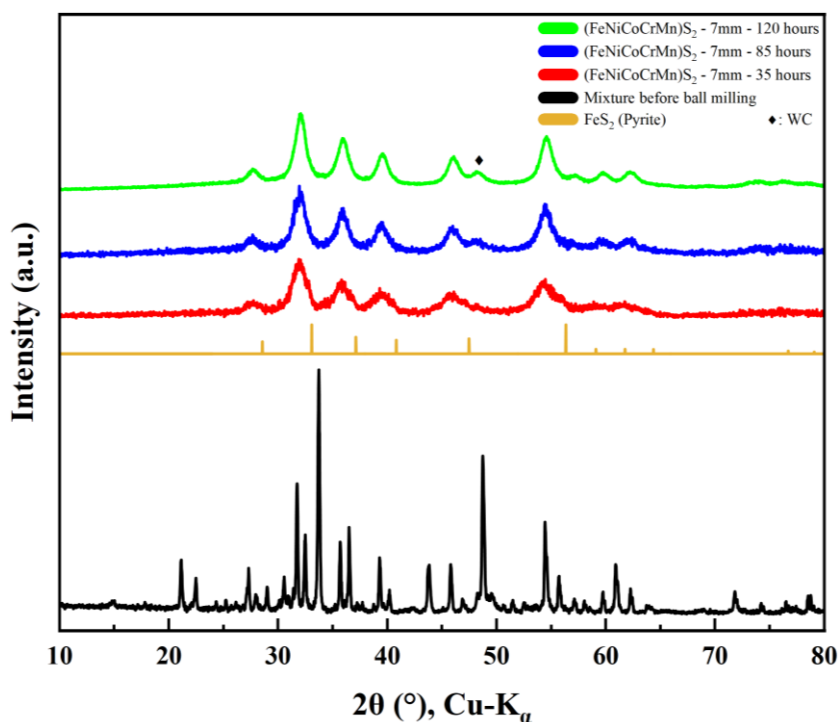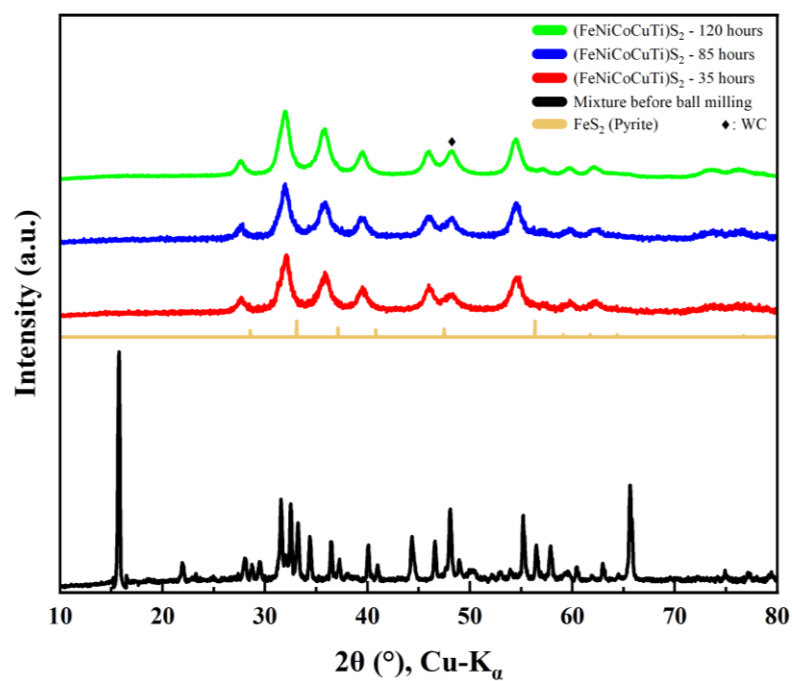Figure 4.7. XRD patterns of 35 hours, 85 hours, and 120 hours ball milled (FeNiCoCuTi)S$_2$ high entropy disulfide.
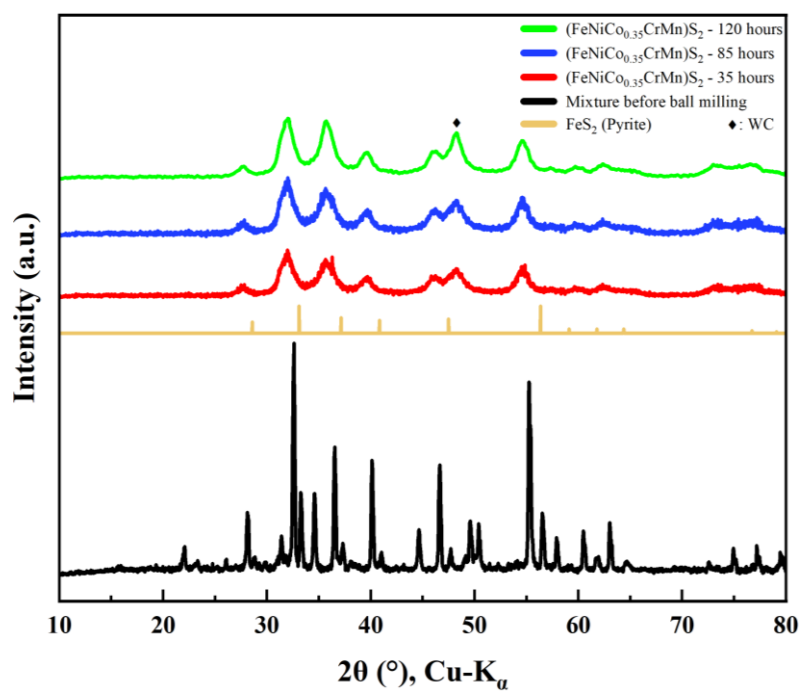
Figure 4.8. XRD patterns of 35 hours, 85 hours, and 120 hours ball milled (FeNiCo$_{0.35}$CrMn)S$_2$ high entropy disulfide.

Powder XRD results show that each of the high entropy sulfides has a single pyrite phase. However, there are again WC impurities coming from the high energy ball milling process. WC peaks are more apparent for $(FeNiCoCuTi)S_2$ and $(FeNiCo_{0.35}CrMn)S_2$ high entropy disulfides than that of $(FeNiCoCrMn)S_2$ – 5 mm and $(FeNiCoCrMn)S_2$ – 7 mm that is attributed to increased cumulative milling time of WC vials and balls. Broad peaks observed in the XRD analyses are attributed to the small particle sizes of the materials.

The details of the crystal structures and lattice parameters of high entropy sulfides were examined using Rietveld refinements. The refinements were performed under the assumption that the cations are uniformly distributed within the pyrite structure. The results of the refinements, given in Figure 4.9, revealed that both $(FeNiCoCuTi)S_2$ and $(FeNiCo_{0.35}CrMn)S_2$ high entropy sulfides have single pyrite structures without including another phase except the WC impurity.
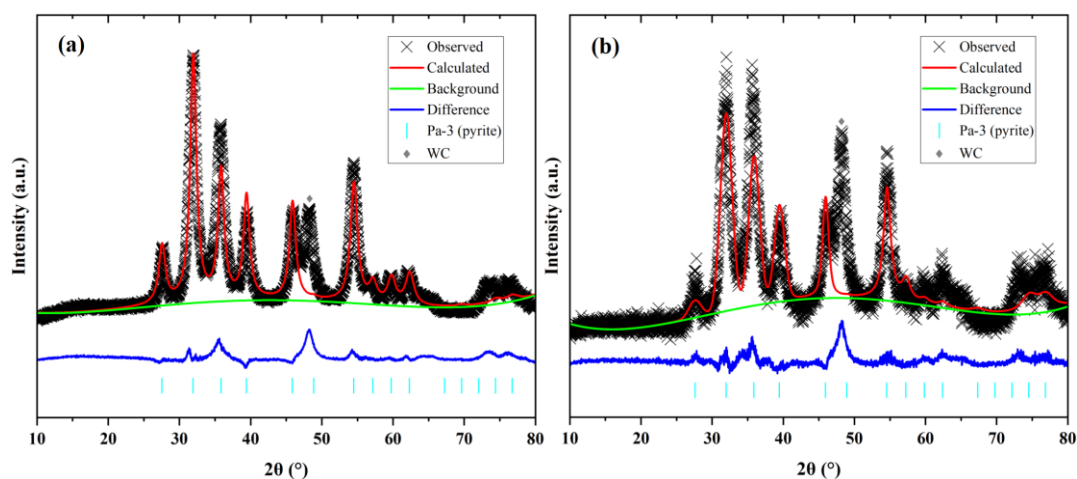
Figure 4.9. Rietveld refinement results of (a) $(FeNiCoCuTi)S_2$ and (b) $(FeNiCo_{0.35}CrMn)S_2$ high entropy disulfides.

The formed high entropy pyrite structures with Pa-3 space group display lattice constants (a) as 5.439 Å and 5.426 Å, respectively. The refinement results are given in detail in Table 4.2.

Table 4.2 Lattice parameters of $(FeNiCoCuTi)S_2$ and $(FeNiCo_{0.35}CrMn)S_2$ obtained from Rietveld refinement.

High Entropy Sulfide	Space Group	a (Å)	Unit Cell Volume (Å³)
$(FeNiCoCuTi)S_2$	Pa-3	5.439	160.933
$(FeNiCo_{0.35}CrMn)S_2$	Pa-3	5.426	159.785

In addition, the crystal structures of the $(FeNiCoCuTi)S_2$ and $(FeNiCo_{0.35}CrMn)S_2$ high entropy disulfides were further investigated by HRTEM and SAED. As shown in Figure 4.10(a) and Figure 4.11(a), the selected areas are attributed to (200) lattice planes of the FeS_2 structure for $(FeNiCoCrMn)S_2 – 5$ mm and $(FeNiCoCrMn)S_2 – 7$ mm with the measured lattice spacings approximately of 0.27 nm. SAED patterns given in Figure 4.10(b) and Figure 4.11(b) show that the diffraction rings match that of the pyrite structure and the lattice spacing measurements from these patterns are compatible with the XRD and Rietveld refinement results.
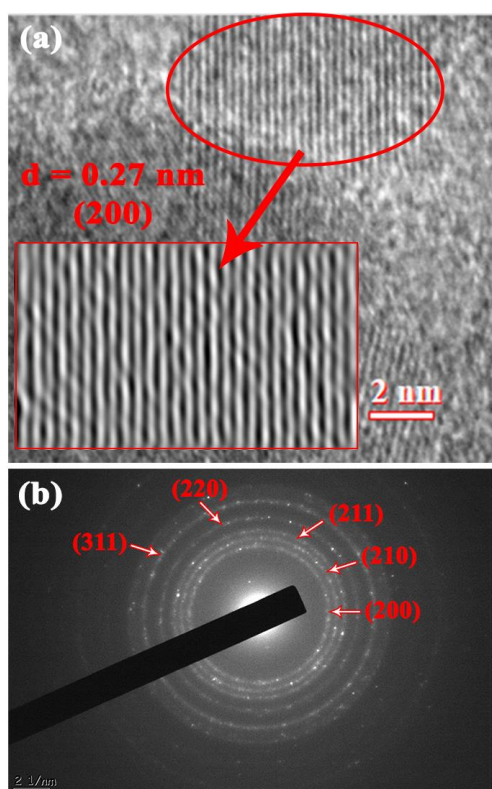
Figure 4.10 HRTEM image (a) and SAED pattern (b) of $(FeNiCoCuTi)S_2$.
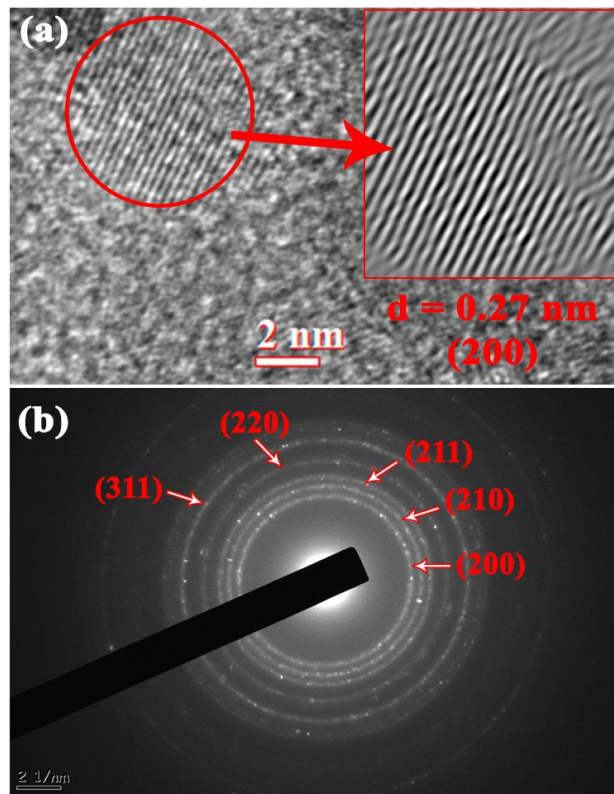
Figure 4.11 HRTEM image (a) and SAED pattern (b) of $(FeNiCo_{0.35}CrMn)S_2$.

4.2 Analyses of the Structural and Morphological Details of High Entropy Disulfides Prepared By High Energy Ball Milling

4.2.1 Analyses of the Structural and Morphological Details of $(FeNiCoCrMn)S_2$ High Entropy Disulfides

SEM analyses were conducted to investigate the structural and morphological information of $(FeNiCoCrMn)S_2 – 5$ mm and $(FeNiCoCrMn)S_2 – 7$ mm high entropy disulfides. The obtained SEM images are given in Figure 4.12 and Figure 4.13, respectively.
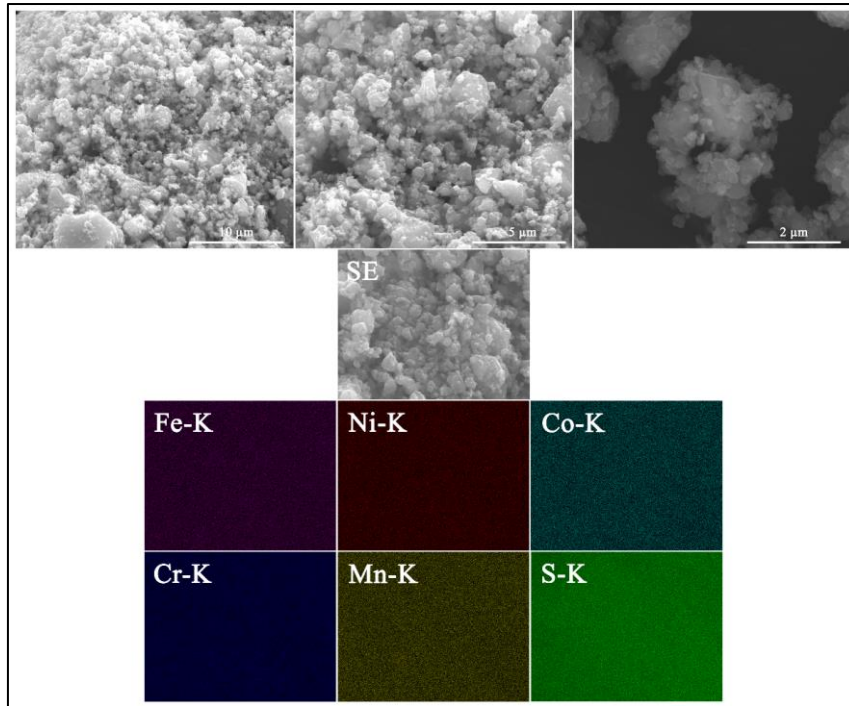
Figure 4.12. SEM image and EDS mapping of (FeNiCoCrMn)S$_2$ – 5 mm high entropy sulfide.
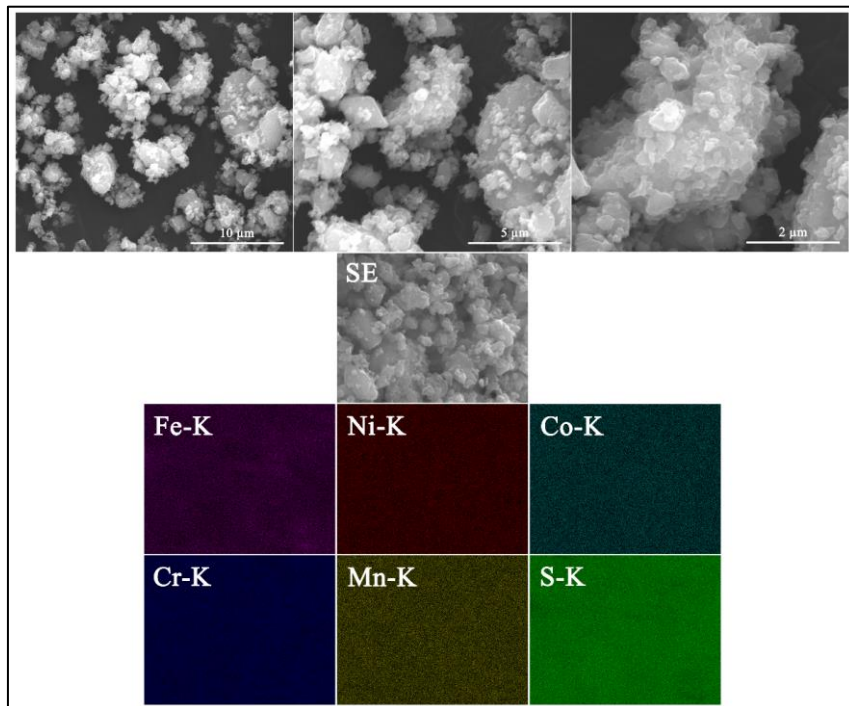
Figure 4.13. SEM image and EDS mapping of (FeNiCoCrMn)S$_2$ – 7 mm high entropy sulfide.

Although there are a few locations with different particle sizes and forms as a result of the inherent characteristics of the ball milling procedure, the SEM images display that the morphology of the synthesized high entropy sulfides is regular in most of the regions. The size of the particles of the $(FeNiCoCrMn)S_2$ – 5 mm powder seems to be a couple of one-tenth of microns. $(FeNiCoCrMn)S_2$ – 7 mm high entropy sulfides particle sizes are relatively larger than the $(FeNiCoCrMn)S_2$ – 5 mm but they are still in the submicron range.

EDS mapping shows that the distribution of the contributed elements is homogeneous both for the $(FeNiCoCrMn)S_2$ – 5 mm and $(FeNiCoCrMn)S_2$ – 7 mm high entropy sulfides. That homogeneity points to achieving maximum configurational entropy [121].

4.2.2 Analyses of the Structural and Morphological Details of $(FeNiCoCuTi)S_2$ and $(FeNiCo_{0.35}CrMn)S_2$ High Entropy Disulfides

SEM analyses were performed to examine the structural and morphological information of $(FeNiCoCuTi)S_2$ and $(FeNiCo_{0.35}CrMn)S_2$ high entropy disulfides. The obtained SEM images are given in Figure 4.14 and Figure 4.15, respectively.
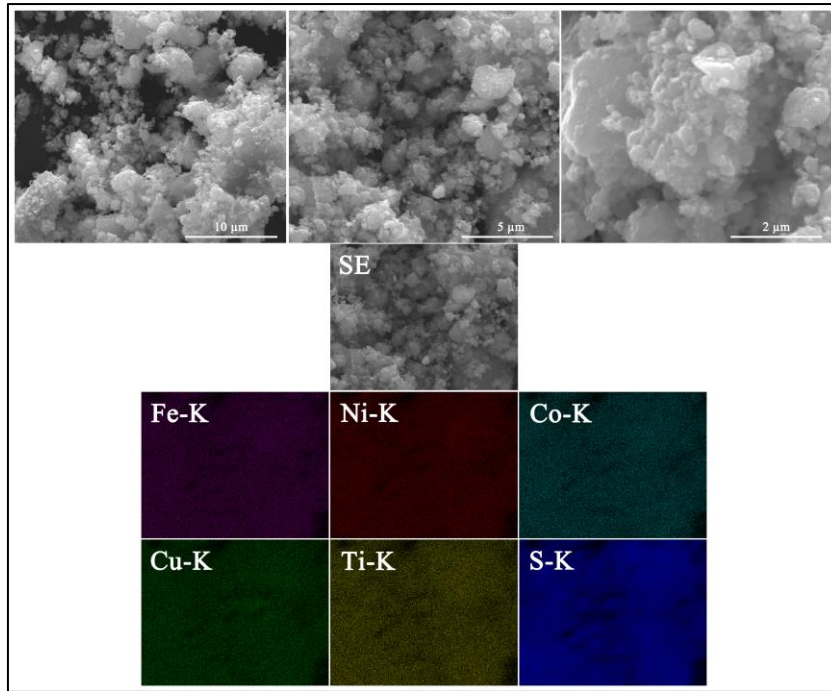
Figure 4.14 SEM image and EDS mapping of (FeNiCoCuTi)S_2 high entropy
sulfide.
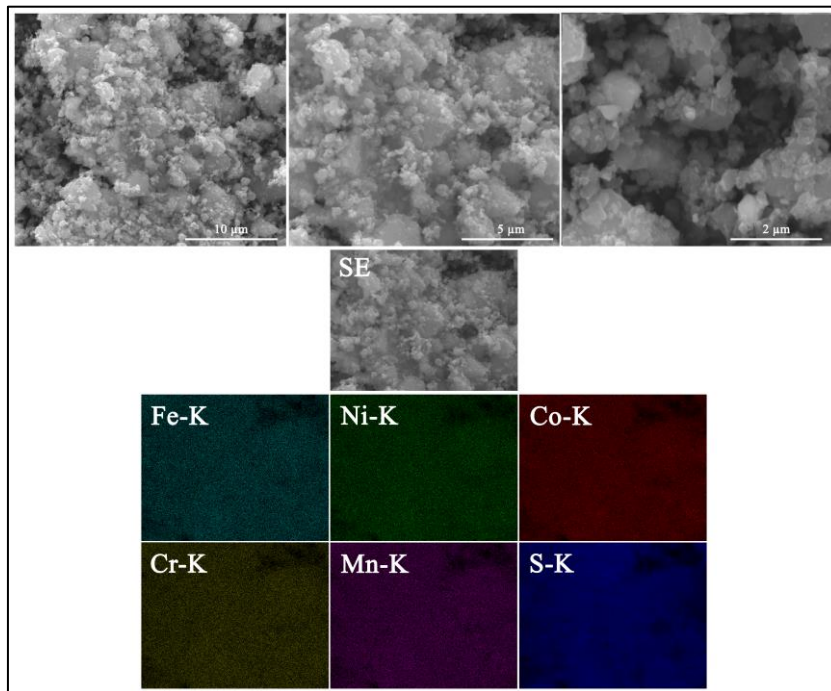
Figure 4.15 SEM image and EDS mapping of (FeNiCo$_{0.35}$CrMn)S_2 high entropy
sulfide.

The obtained SEM images and corresponding EDS mapping results are similar with that of (FeNiCoCrMn)S$_2$ – 5 mm and (FeNiCoCrMn)S$_2$ – 7 mm. Although there are a few locations with different particle sizes thanks to the ball milling procedure, the SEM images display that the morphology of the synthesized high entropy sulfides is regular in most of the regions with submicron particle size ranges.

EDS mapping also shows that the distribution of the contributed elements is homogeneous both for the (FeNiCoCuTi)S$_2$ and (FeNiCo$_{0.35}$CrMn)S$_2$ high entropy disulfides.

4.3   Analyses of the Elemental Compositions of the High Entropy Sulfides

The prepared sulfides elemental compositions were examined by ICP-OES analyses. The ICP-OES results were utilized to demonstrate these samples suitability for categorization as high entropy materials.

4.3.1   Elemental Compositions of the (FeNiCoCrMn)S$_x$.aH$_2$O High Entropy Sulfide

Molar fractions of elements for the sulfide powders obtained by the solvothermal method are attained based on the ICP-OES results and given in Figure 4.16.
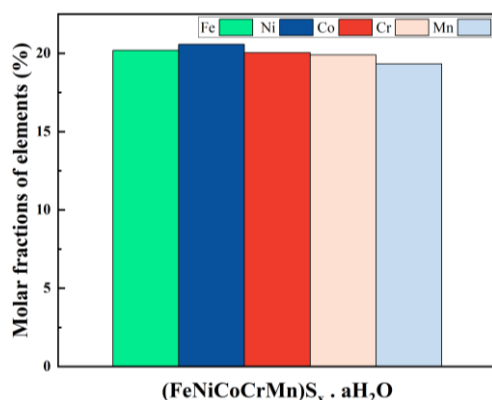
Figure 4.16 Molar fractions of the elements for the (FeNiCoCrMn)S$_x$.aH$_2$O sample.

The configurational entropy of the $(FeNiCoCrMn)S_x.aH_2O$ sulfide is calculated using the Equation (2.9) and found 1.609 R indicating the cations are equimolar and the material can be regarded as a high entropy material.

4.3.2 Elemental Compositions of the $(FeNiCoCrMn)S_2$ High Entropy Disulfides

Molar fractions of the elements for high entropy disulfides prepared by high energy ball milling are attained based on the ICP-OES results and given in Figure 4.17 and Figure 4.18, respectively.
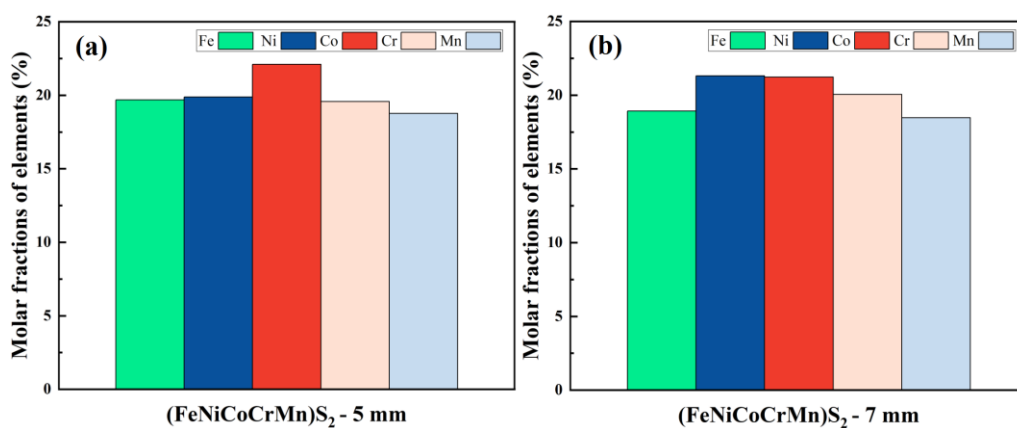
Figure 4.17 Molar fractions of the elements for (a) $(FeNiCoCrMn)S_2$ – 5 mm, (b) $(FeNiCoCrMn)S_2$ – 7 mm.
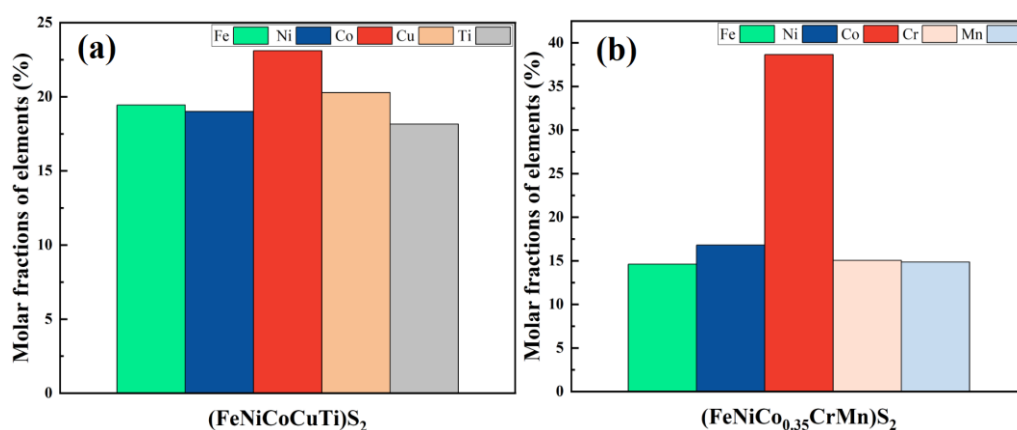
Figure 4.18 Molar fractions of the elements for (a) $(FeNiCoCuTi)S_2$, (b) $(FeNiCo_{0.35}CrMn)S_2$.

The configurational entropy of the $(FeNiCoCrMn)S_2$ – 5 mm, $(FeNiCoCrMn)S_2$ – 7 mm, $(FeNiCoCuTi)S_2$, and $(FeNiCo_{0.35}CrMn)S_2$ disulfides are calculated using Equation (2.9) and found 1.608 R, 1.608 R, 1.606 R, and 1.517 R, respectively. These results indicate each of the materials can be regarded as high entropy materials. Moreover, the stoichiometries of the synthesized high entropy sulfide powders are found as $(Fe_{0.10}Ni_{0.10}Co_{0.11}Cr_{0.10}Mn_{0.09})S_1$, $(Fe_{0.10}Ni_{0.11}Co_{0.11}Cr_{0.10}Mn_{0.09})S_1$, $(Fe_{0.11}Ni_{0.10}Co_{0.12}Cu_{0.11}Ti_{0.10})S_1$, and $(Fe_{0.08}Ni_{0.09}Co_{0.20}Cr_{0.08}Mn_{0.08})S_1$ by normalizing the cations atomic fractions to sulfur, respectively. The calculations showed that the stoichiometry of the materials fits with MS_2 (pyrite) stoichiometry.

4.4 Analyses of the Thermal Stabilites of the High Entropy Sulfides

The thermal stabilities of the produced high entropy sulfides up to 1000 °C were investigated by TGA.

4.4.1 Thermal Stability of the $(FeNiCoCrMn)S_x.aH_2O$ High Entropy Sulfide

Figure 4.19 displays the results of TGA of the $(FeNiCoCrMn)S_x.aH_2O$ high entropy sulfide.
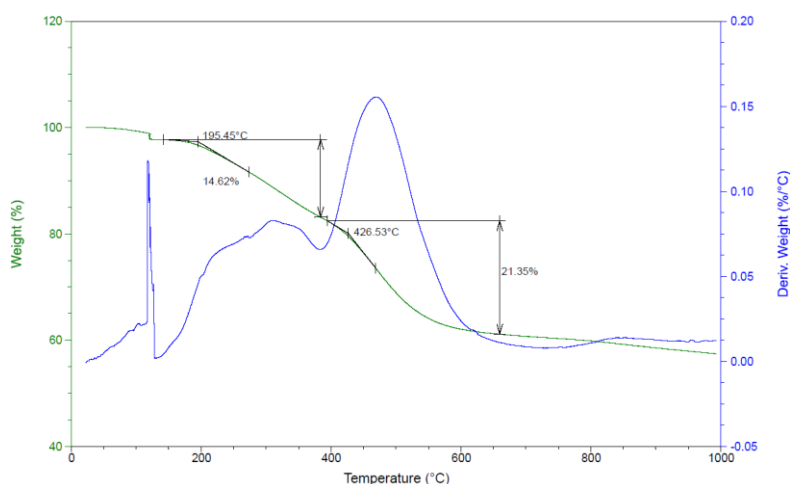
Figure 4.19. TGA curve of solvothermally synthesized $(FeNiCoCrMn)S_x.aH_2O$.

As shown in Figure 4.19, $(FeNiCoCrMn)S_x.aH_2O$ synthesized by solvothermal method has three intervals leading to weight losses. The first loss is nearly 4% between 100 °C and 150 °C, and attributed to physically bonded constituents vaporization and desorption. Other two temperature intervals involve the temperatures between 194 °C and 550 °C and leads to weight losses of approximately 14% and 22%, respectively. They are ascribed to the elimination of hydroxyl groups and structural water caused by the topotactic transformation of metal hydroxides during the solvothermal procedure [133]. Although these temperatures leading to weight losses are close to the theoretical reaction temperatures of these groups, there are some shifts to higher temperatures. The higher energy requirements for thermal decomposition events can be a result of the high configurational entropy of the material [134]. Before reaching 550 °C, nearly 40% of weight is lost. It leads to a lack of active material if that material be utilized as a cathode for thermal batteries, since the batteries operation temperatures are above 500 °C.

4.4.2 Thermal Stability of the $(FeNiCoCrMn)S_2$ High Entropy Disulfides

The TGA plot given in Figure 4.20 (a) shows that the thermal decomposition of $(FeNiCoCrMn)S_2 - 5$ mm starts at 408.43 °C and continues with additional two main intervals leading to 7.13% and 12.14% mass losses, respectively. By 700 °C and 1000 °C, nearly 22% and 24% of weight is lost, respectively.

Although a similar thermogram with $(FeNiCoCrMn)S_2 - 5$ mm is observed, the mass loss of $(FeNiCoCrMn)S_2 - 7$ mm high entropy disulfide begins at a higher temperature of approximately 427 °C, which can be seen in Figure 4.20 (b). Similar to the former disulfide, the latter also exhibits two following intervals and lost about 25% of total weight before 700 °C. The weight loss becomes nearly 29% at 1000 °C.
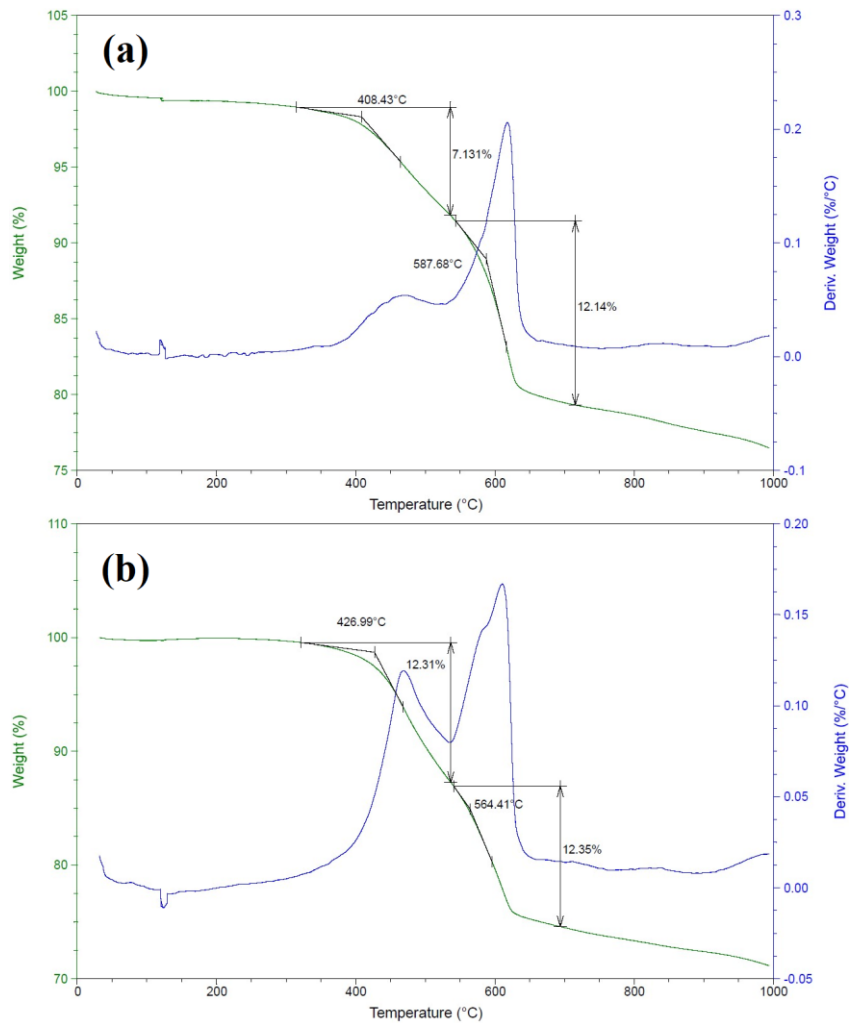
Figure 4.20 TGA curves of (a) (FeNiCoCrMn)S$_2$ – 5 mm and (b) (FeNiCoCrMn)S$_2$ – 7 mm high entropy disulfides synthesized by high energy ball milling.

4.4.3 Thermal Stability of the (FeNiCoCuTi)S$_2$ and (FeNiCo$_{0.35}$CrMn)S$_2$ High Entropy Disulfides

Figure 4.21 demonstrates the TGA results of (FeNiCoCuTi)S$_2$ and (FeNiCo$_{0.35}$CrMn)S$_2$ high entropy disulfides. As shown in Figure 4.21 (a), the thermal decomposition of (FeNiCoCuTi)S$_2$ has a relatively lower starting temperature of 296.7 °C. There are three main intervals that cause 4.61%, 3.49%, and 11.95% weight losses. By 700 °C and 1000 °C, about 21% and 24% of total weight is lost.

In a comparison with other synthesized disulfides, $(FeNiCo_{0.35}CrMn)S_2$ has a sufficiently higher initial thermal decomposition temperature of 465.83 °C, which can be seen in Figure 4.21 (b). The thermogram show there are two main intervals leading to 4.22% and 10.33% mass losses, respectively. The weight loss reaches about 15% and 18% of weight losses at 700 °C and 1000 °C, respectively.
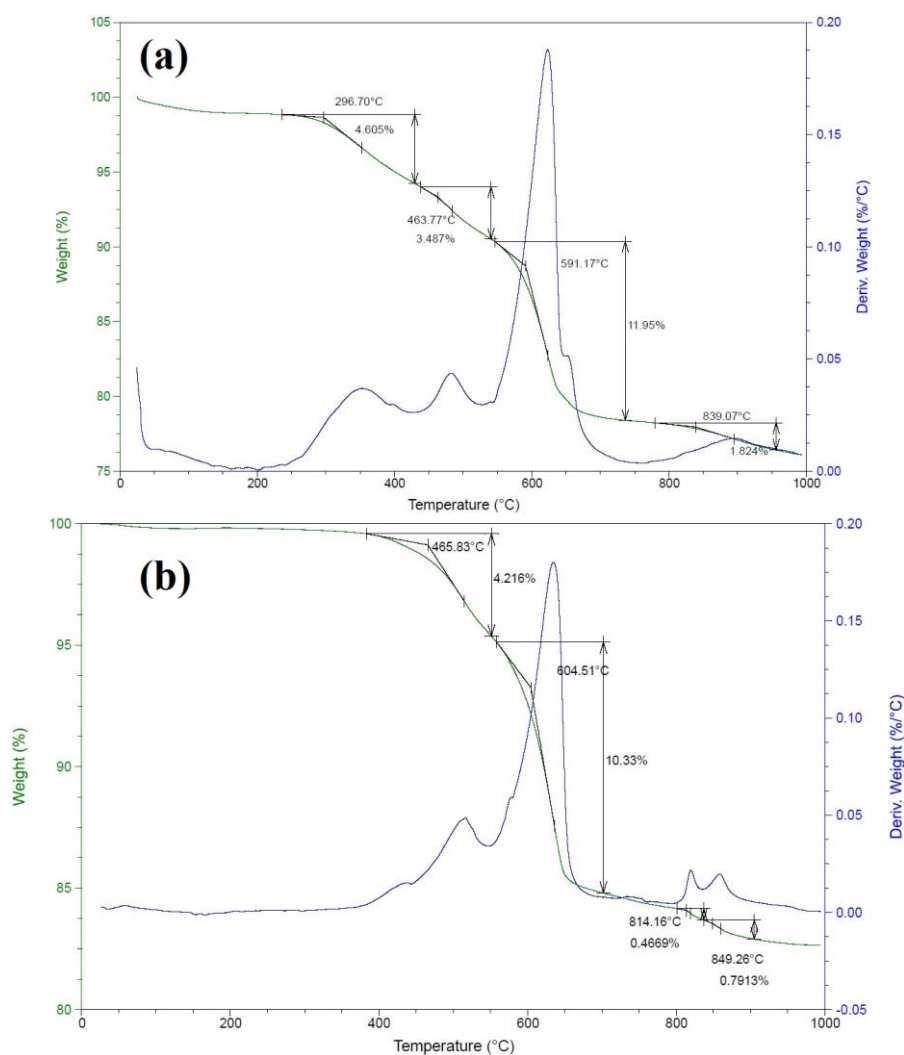
Figure 4.21 TGA curves of (a) $(FeNiCoCuTi)S_2$ and (b) $(FeNiCo_{0.35}CrMn)S_2$ high entropy disulfides synthesized by high energy ball milling.

The thermograms given in Figure 4.19, Figure 4.20, and Figure 4.21 also show that thermal decompositions and phase changes are not fast and require a temperature and time interval to occur for high entropy sulfides. This property may be ascribed

to the multiple different elements in their structure and suits the inherent properties of high entropy materials [132].

4.5   Analyses of the Surface Chemistry of High Entropy Disulfides

The surface chemistry and oxidation states of the produced $(FeNiCoCrMn)S_2 - 5$ mm, $(FeNiCoCrMn)S_2 - 7$ mm, $(FeNiCoCuTi)S_2$, and $(FeNiCo_{0.35}CrMn)S_2$ materials were examined with XPS. The obtained XPS survey spectra for each of the high entropy sulfides are shown in Figure 4.22.
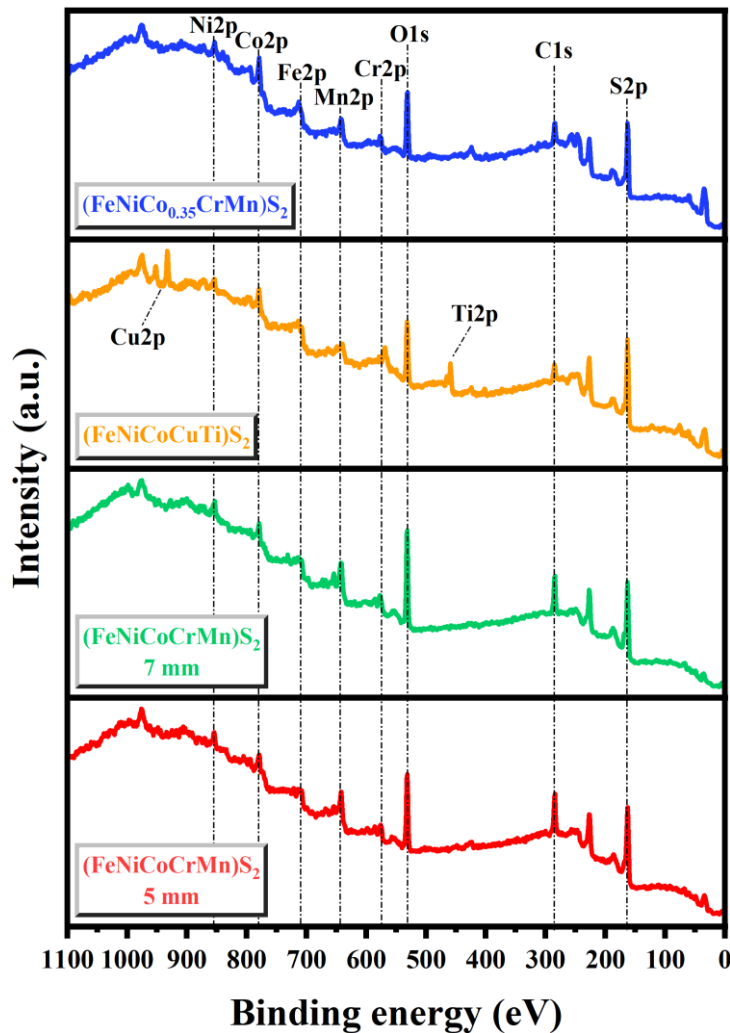
Figure 4.22 XPS survey spectra of $(FeNiCoCrMn)S_2 - 5$ mm, $(FeNiCoCrMn)S_2 - 7$ mm, $(FeNiCoCuTi)S_2$, and $(FeNiCo_{0.35}CrMn)S_2$ high entropy disulfides.

The surveys reveal that all of the high entropy disulfides contain S, Fe, Ni, and Co species. Cr and Mn also exist in their surface except (FeNiCoCuTi)S_2. The presence of Cu 2p and Ti 2p spectra and the absence of Cr 2p and Mn 2p spectra demonstrate that (FeNiCoCuTi)S_2 has a different elemental composition in comparison with the other high entropy disulfides.

XPS results also show that the materials have some oxygenated compounds on their surface. As given in Figure 4.23, the O 1s spectra of the sulfides have a primary peak at nearly 531.5 eV and two subpeaks at 530.5 eV and 534 eV. The primary peak may be attributed to metal hydroxides (MOH), sulfur oxides (SO_x), or carbonyl groups. The first subpeak placed nearly at 530.5 eV can be assigned to metal oxides (MO). That peak is more apparent for (FeNiCoCuTi)S_2 and (FeNiCo$_{0.35}$CrMn)S_2 and may be attributed to interactions at the surface that can occur with oxygen species before the analysis or sampling stage. The other subpeak with insignificant intensities may be attributed to carbon-oxygen bonds [121].
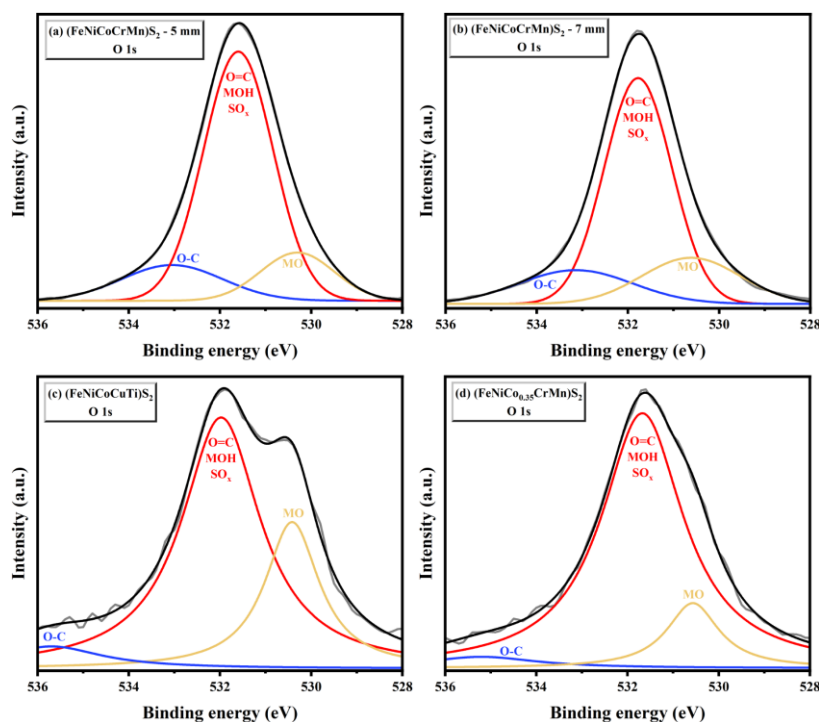
Figure 4.23 O 1s XPS spectra of (a) (FeNiCoCrMn)S_2 – 5 mm, (b) (FeNiCoCrMn)S_2 – 7 mm, (c) (FeNiCoCuTi)S_2, and (d) (FeNiCo$_{0.35}$CrMn)S_2.

The XPS signals of S 2p spectra are given in Figure 4.24. The deconvoluted spectra of S 2p show three peaks. The main peaks approximately at 162.5 eV represent disulfide ions (S_2^{2-}) whereas the subpeaks nearly at 164 eV show disulfide bonds (S-S). Other subpeaks roughly at 168.5 eV may be attributed to sulfur oxides (SO_x) [121].
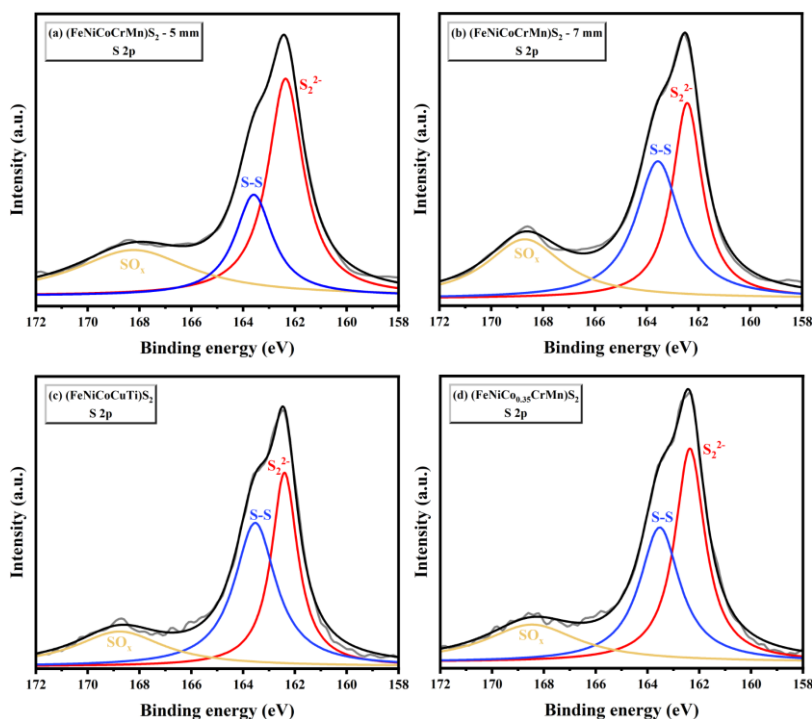
Figure 4.24 S 2p XPS spectra of (a) (FeNiCoCrMn)S_2 – 5 mm, (b) (FeNiCoCrMn)S_2 – 7 mm, (c) (FeNiCoCuTi)S_2, and (d) (FeNiCo$_{0.35}$CrMn)S_2.

The XPS spectra of Fe 2p, Ni 2p, and Co 2p are shown in Figure 4.25, Figure 4.26, and Figure 4.27, respectively. The Fe 2p spectra of high entropy sulfides are deconvoluted to two peaks of Fe 2p$_{3/2}$, two peaks of Fe 2p$_{1/2}$, and corresponding satellite (sat.) peaks. The peaks nearly at 707.5 eV and 711 eV may be attributed to Fe^{2+} and Fe^{3+} species of Fe 2p$_{3/2}$, respectively. The subpeaks of Fe 2p$_{1/2}$ roughly at 721 eV and 724 can also be associated with Fe^{2+} and Fe^{3+} species, respectively. The related satellite peaks are positioned at nearly 714 eV and 731 eV. The deconvoluted Ni 2p spectra display two peaks at almost 853 eV and 856 eV, which are attributed to Ni^{2+} and Ni^{3+} species of Ni 2p$_{3/2}$, respectively. The peaks related to Ni 2p$_{1/2}$

70

approximately at 871.2 eV and 875 eV are also associated with Ni^{2+} and Ni^{3+}, respectively. The corresponding satellite peaks of Ni 2p spectra are positioned roughly at 860 eV and 879 eV. The Co 2p spectra show two subpeaks of Co $2p_{3/2}$ at 778.5 eV and 781 eV which are attributed to Co^{3+} and Co^{2+} species, respectively. Other peaks linked to Co $2p_{1/2}$ at 794 eV and 798 eV can also be associated with Co^{3+} and Co^{2+} species, respectively. The related satellite signals are located at nearly 785 eV and 804 eV [129,135].
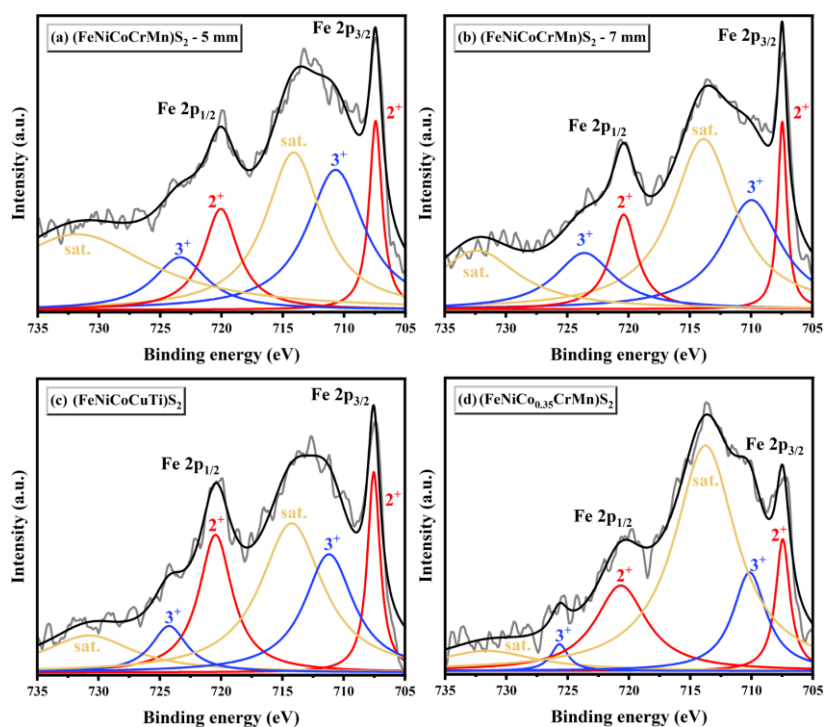
Figure 4.25 Fe 2p XPS spectra of (a) $(FeNiCoCrMn)S_2$ – 5 mm, (b) $(FeNiCoCrMn)S_2$ – 7 mm, (c) $(FeNiCoCuTi)S_2$, and (d) $(FeNiCo_{0.35}CrMn)S_2$.
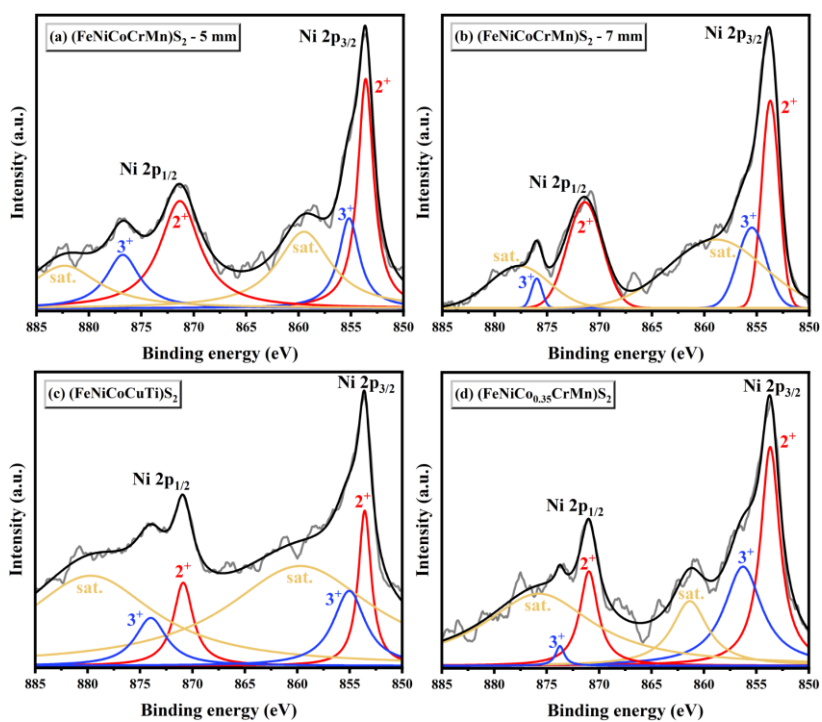
Figure 4.26 Ni 2p XPS spectra of (a) $(FeNiCoCrMn)S_2 - 5$ mm, (b) $(FeNiCoCrMn)S_2 - 7$ mm, (c) $(FeNiCoCuTi)S_2$, and (d) $(FeNiCo_{0.35}CrMn)S_2$.
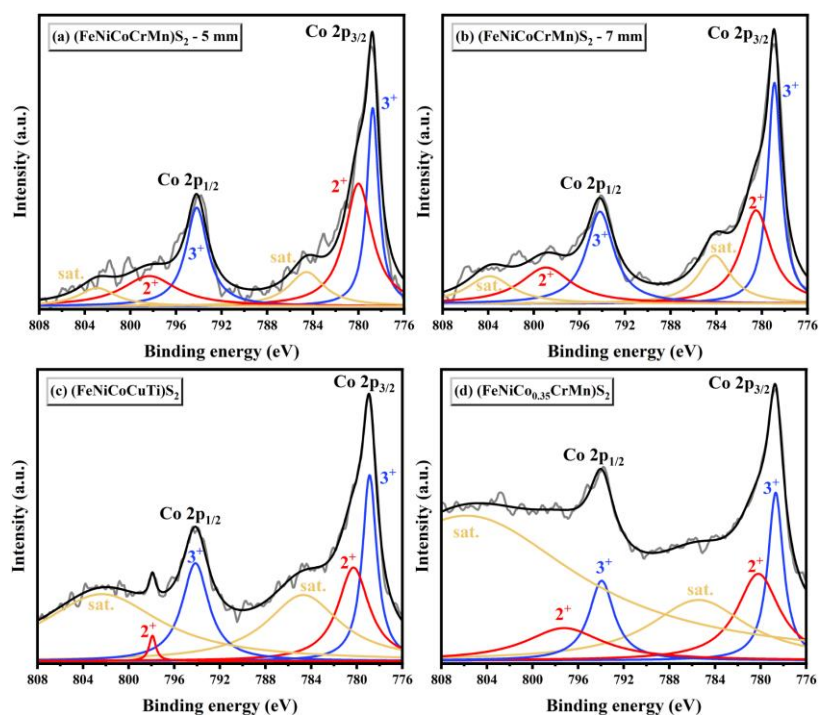
Figure 4.27 Co 2p XPS spectra of (a) $(FeNiCoCrMn)S_2 - 5$ mm, (b) $(FeNiCoCrMn)S_2 - 7$ mm, (c) $(FeNiCoCuTi)S_2$, and (d) $(FeNiCo_{0.35}CrMn)S_2$.

Cr 2p and Mn 2p spectra of $(FeNiCoCrMn)S_2 – 5$ mm, $(FeNiCoCrMn)S_2 – 7$ mm, and $(FeNiCo_{0.35}CrMn)S_2$ are presented in Figure 4.28 and Figure 4.29, respectively. Although Mn 2p spectra is deconvoluted similarly to Fe 2p, Ni 2p, and Co 2p, the Cr 2p spectra of high entropy disulfides exhibit two distinct peaks at almost 576.5 eV and 586 eV which are associated with the Cr^{3+} species of Cr $2p_{3/2}$ and $2p_{1/2}$, respectively [136]. The deconvoluted Mn 2p spectra exhibit two peaks at almost 641 eV and 644 eV, which can be attributed to Mn^{2+} and Mn^{3+} species of Mn $2p_{3/2}$, respectively. The subpeaks of Mn $2p_{1/2}$ at nearly 653 eV and 655 eV are also associated with Mn^{2+} and Mn^{3+} species, respectively. The observed satellite peaks of Mn 2p spectra are roughly at 646 eV and 658 eV [135,137].
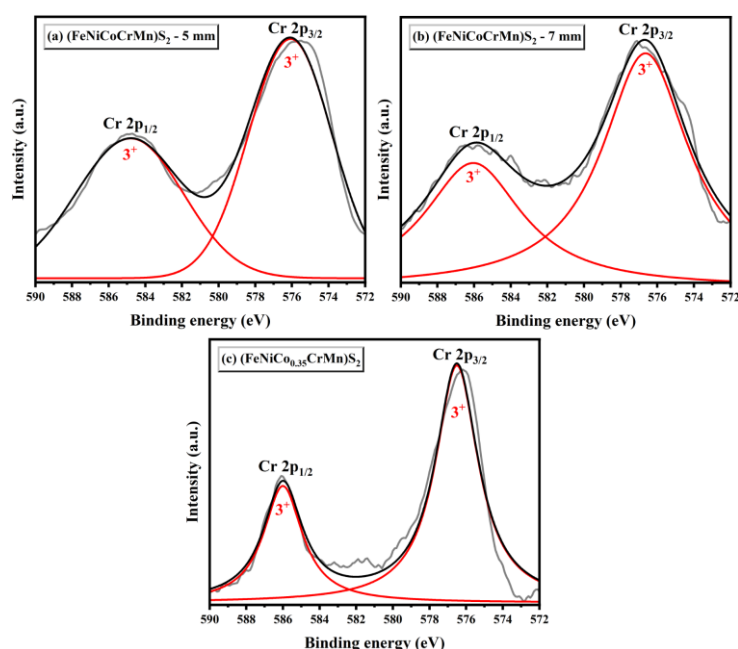
Figure 4.28 Cr 2p XPS spectra of (a) $(FeNiCoCrMn)S_2 – 5$ mm, (b) $(FeNiCoCrMn)S_2 – 7$ mm, and (c) $(FeNiCo_{0.35}CrMn)S_2$.

Cu 2p and Ti 2p spectra of $(FeNiCoCuTi)S_2$ are given in the Figure 4.30. Both of these signals have two distinct peaks and can be related to one state number. Cu 2p spectrum of $(FeNiCoCuTi)S_2$ high entropy disulfide exhibits two definite peaks at 932.4 eV and 952.4 eV which can be attributed to Cu^{2+} species of Cu $2p_{3/2}$ and Cu $2p_{1/2}$, respectively [135]. Furthermore, Ti 2p spectrum of $(FeNiCoCuTi)S_2$ shows

two apparent peaks at 458.9 eV and 464.6 eV which are associated with Ti^{4+} species of Ti $2p_{3/2}$ and Ti $2p_{1/2}$, respectively [138].
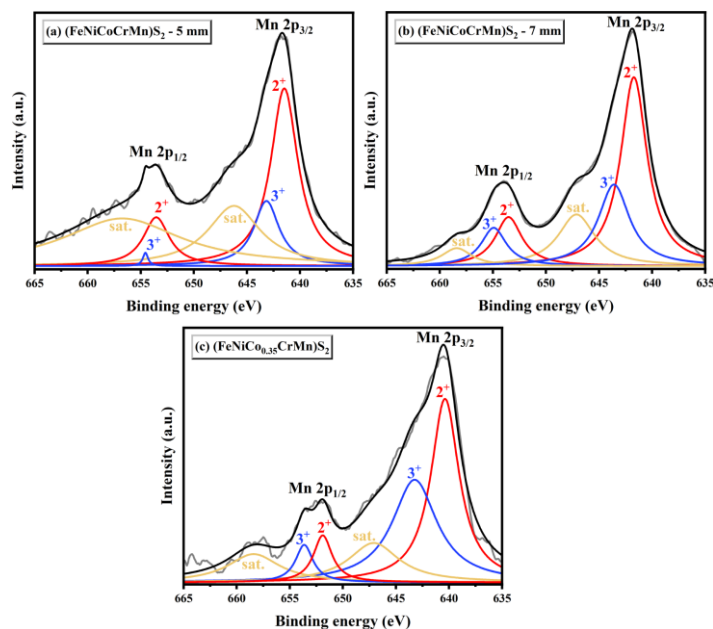
Figure 4.29 Mn 2p XPS spectra of (a) $(FeNiCoCrMn)S_2$ – 5 mm, (b) $(FeNiCoCrMn)S_2$ – 7 mm, and (c) $(FeNiCo_{0.35}CrMn)S_2$.
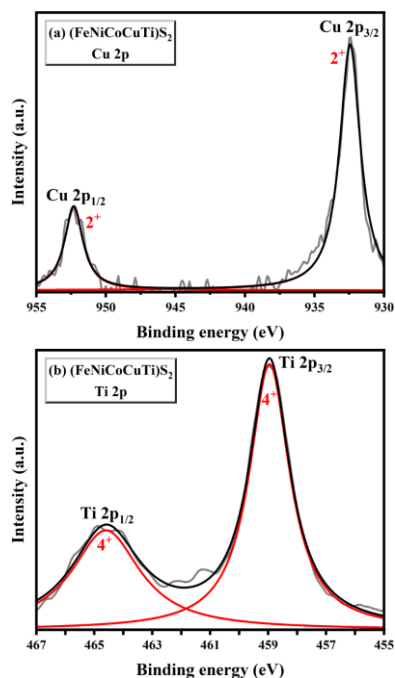
Figure 4.30 (a) Cu 2p, (b) Ti 2p XPS spectra of $(FeNiCoCuTi)S_2$ high entropy sulfide.

4.6   Analyses of the Electrochemical Characteristics of the High Entropy Sulfides

The current profile applied in the discharge tests of the prepared high entropy sulfides is shown in Figure 4.31. The applied profile includes a constant load of 0.24 A (0.18 A/cm^2) and a pulse load of 1 A (0.75 A/cm^2) for 100 ms every 3 seconds. The profile was applied after 10 seconds of discharge without load and terminated when the baseload voltage of 1.0 V was obtained in order to calculate the specific capacity and energy values at different cut-off voltages.
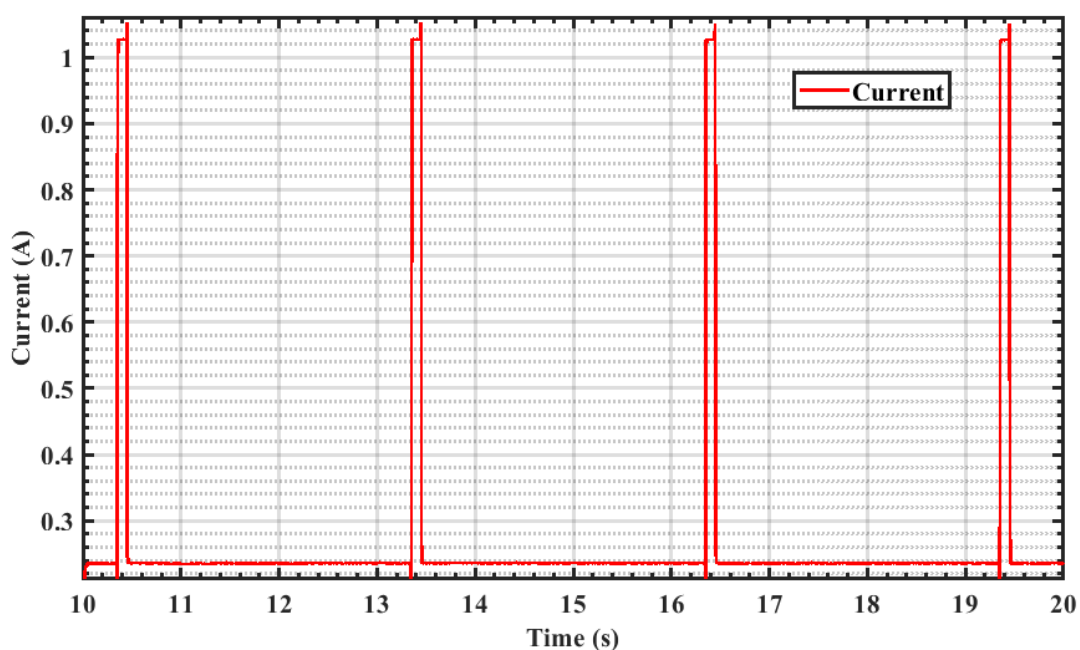
Figure 4.31. Current profile applied in the discharge tests of the prepared high entropy sulfides.

4.6.1   Electrochemical Performance of the (FeNiCoCrMn)S$_x$.aH$_2$O High Entropy Sulfide

Figure 4.32 demonstrates the discharge curves of (FeNiCoCrMn)S$_x$.aH$_2$O high entropy sulfide synthesized by the solvothermal method with a comparison of conventional FeS$_2$ at 475 °C.
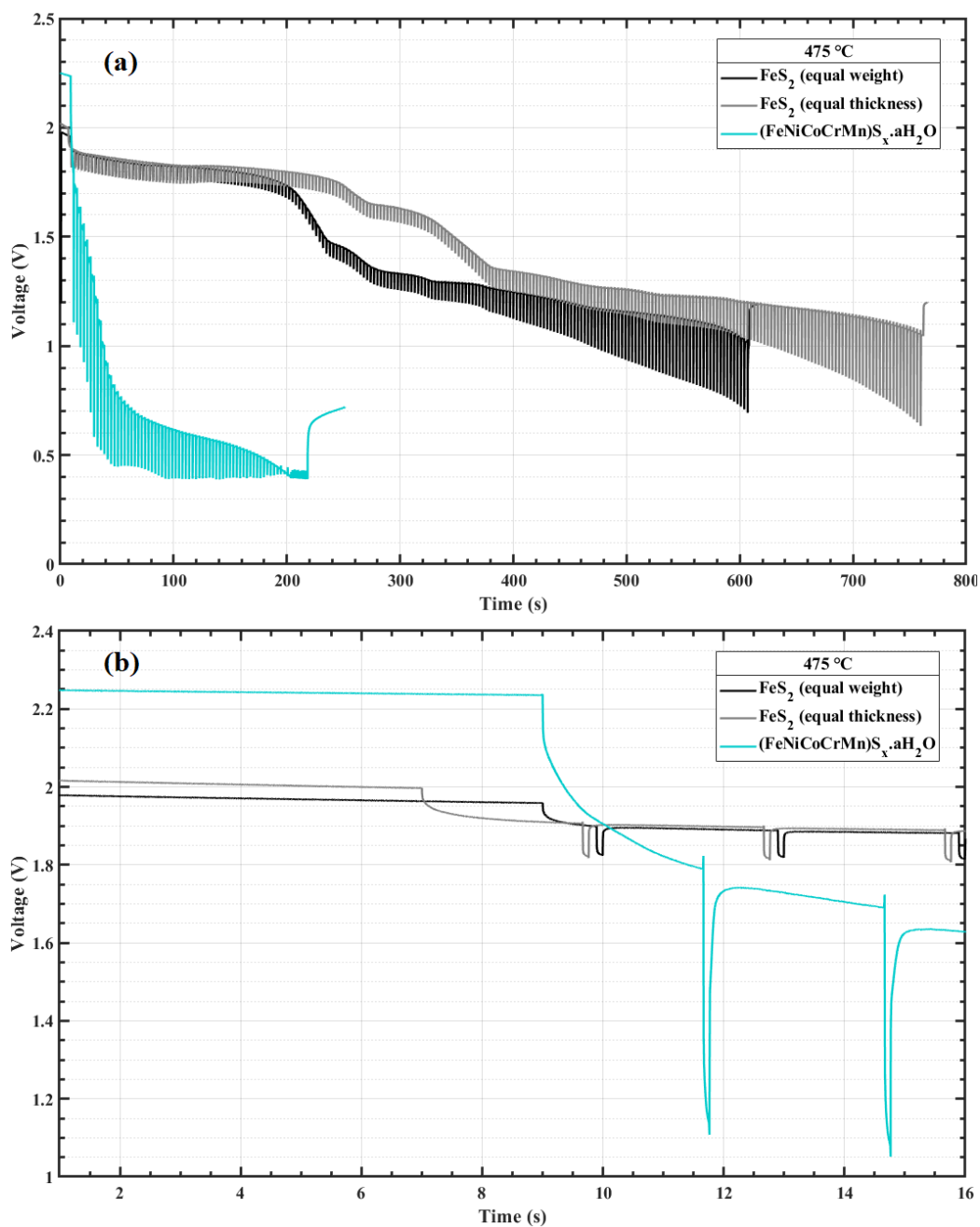
Figure 4.32. Discharge curves of single cells with $(FeNiCoCrMn)S_x.aH_2O$ and conventional FeS_2 cathodes a) at 475 °C, b) at 475 °C between 0-25s period.

The discharge results of $(FeNiCoCrMn)S_x.aH_2O$ indicate that the high entropy sulfide increased the open circuit voltage of the electrochemical cell from approximately 2 V to 2.25 V. However, once the load is applied the single cell with $(FeNiCoCrMn)S_x.aH_2O$ cathode discharged instantly. Sharp decreases in the

76

voltages when applying load is caused by relatively higher internal resistances of the material and it may be attributed to the low electrical conductivity of the material.

Moreover, a comparison of discharge curves of $(FeNiCoCrMn)S_x.aH_2O$ high entropy sulfide at 475°C and 525°C is given in Figure 4.33.
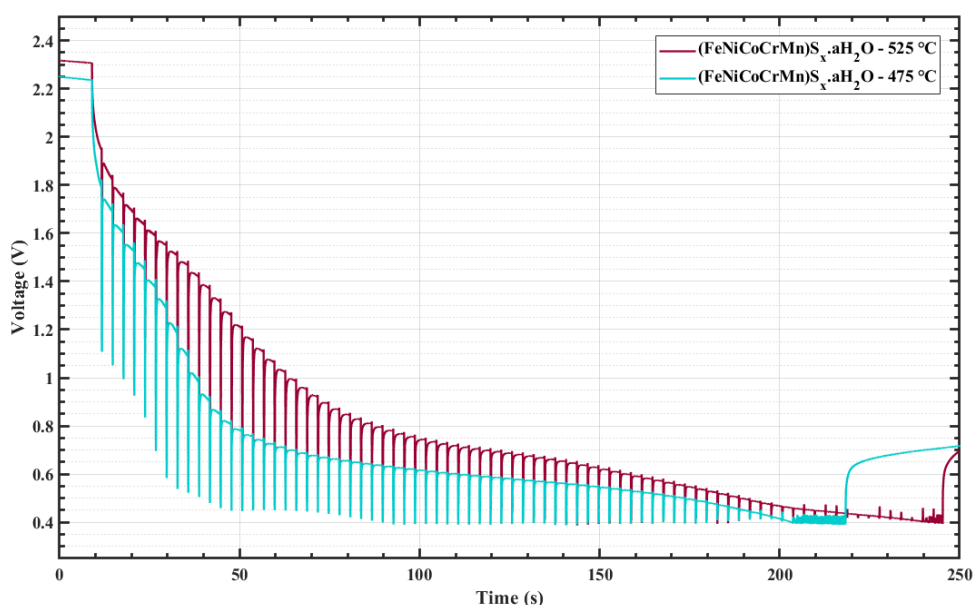
Figure 4.33 Discharge curves of $(FeNiCoCrMn)S_x.aH_2O$ high entropy sulfide a) at 475°C and 525°C, b) at 475°C and 525°C with a cuf-off voltage of 1.5V.

Although the electrochemical performance of the single cell with $(FeNiCoCrMn)S_x.aH_2O$ cathode is slightly increased at the elevated temperature, the overall performance is yet insufficient due to severe voltage drops, especially at pulses.

The single cell discharge tests of $(FeNiCoCrMn)S_x.aH_2O$ suggest that its relatively higher open circuit voltage may provide the high entropy sulfide to be utilized in applications requiring too short operation times such as 5 or 10 seconds. However, its poor electrochemical performance after applying load and relatively lower electrical conductivity suggest that different high entropy sulfides more suitable for thermal battery applications requiring high electrical conductivity and stability under high temperature conditions may be developed rather than this sulfide containing some groups lowering the electrical conductivity and prohibiting the longer

discharging times. Since the electrochemical results of $(FeNiCoCrMn)S_x.aH_2O$ cathode show a sharp decrease in voltage at the beginning of applying load and it cannot achieve feasible cut-off voltage values, the specific capacity, energy, and, internal resistance calculations could not be performed for this high entropy sulfide.

4.6.2 Electrochemical Performance of $(FeNiCoCrMn)S_2 – 5$ mm and $(FeNiCoCrMn)S_2 – 7$ mm High Entropy Disulfides

Figure 4.34 demonstrates the discharge curves of the single cells with $(FeNiCoCrMn)S_2 – 5$ mm and $(FeNiCoCrMn)S_2 – 7$ mm high entropy disulfide cathodes synthesized by high energy ball milling process with a comparison of conventional FeS_2 (pyrite) cathode at different single cell discharge temperatures of 475 °C, 525 °C, and 575 °C.

The discharge curves indicate that open circuit voltages of high entropy disulfide cathodes are superior compared to conventional FeS_2 cathodes. That effect is most apparent at 475 °C, at which the single cells with $(FeNiCoCrMn)S_2 – 7$ mm, $(FeNiCoCrMn)S_2 – 5$ mm, and conventional FeS_2 cathodes have open circuit voltages of 2.30 V, 2.19 V, and 1.93 V, respectively. The open circuit voltages of $(FeNiCoCrMn)S_2 – 7$ mm and $(FeNiCoCrMn)S_2 – 5$ mm cathodes at 525 °C are 2.14 V and 2.09 V showing also significant increases relative to the FeS_2 with an open circuit voltage of 1.91 V. However, the elevation of open circuit voltages lessens when the discharge temperature becomes higher. The higher voltage advantage is lost especially for $(FeNiCoCrMn)S_2 – 5$ mm cathodes with a 1.93 V open circuit voltage, nearly the same as FeS_2 at 575 °C discharge temperature. $(FeNiCoCrMn)S_2 – 7$ mm cathodes still show the highest open circuit voltage of 2.10 V among these cathodes but the voltage value decreases at elevated temperatures. Relatively lower thermal stabilities may lead to these voltage drops because the amount of active materials decreases and sulfur appears at higher temperatures. Yet, high entropy disulfides still have higher maximum voltages than the reference pyrite at every discharge temperature.
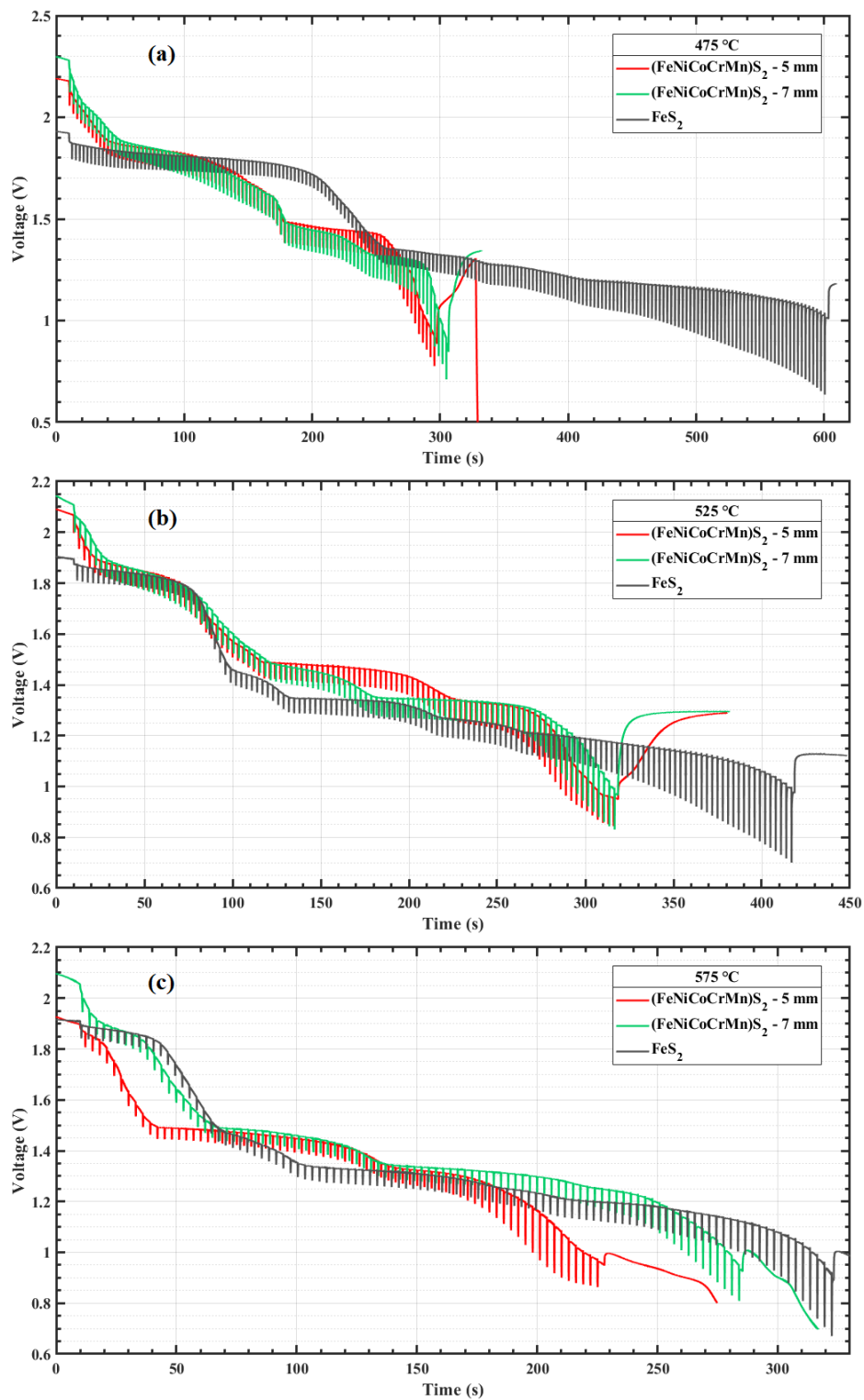
Figure 4.34 Discharge curves of single cells with (FeNiCoCrMn)S_2 – 5 mm, (FeNiCoCrMn)S_2 – 7 mm, and conventional FeS_2 cathodes at (a) 475 ℃, (b) 525 ℃, and (c) 575 ℃ discharge temperatures.

Moreover, these high entropy sulfides show different discharge characteristics when the temperature changes. In spite of achieving higher voltage values, the voltage drops are faster than conventional FeS_2 at 475 °C decreasing the operation time. At this temperature, high entropy disulfides start with higher discharge voltages, however, their performance gradually decreases after nearly 100 seconds. Elevating the discharge temperature to 525 °C increases their discharge performance dramatically. They outperform the conventional FeS_2 until 300 seconds comprising the meaningful voltage ranges for thermal battery applications. The discharge results at 575 °C depict that $(FeNiCoCrMn)S_2$ – 7 mm cathode mostly preserves its high performance but $(FeNiCoCrMn)S_2$ – 5 mm cathode weakens at some regions of the discharge with a comparison of conventional FeS_2. That performance and voltage loss may be attributed to the thermal decomposition of the active materials at elevated temperatures. Nevertheless, the results of the single cell discharge tests suggest that both $(FeNiCoCrMn)S_2$ high entropy disulfides have great potential as thermal battery cathode materials, especially for applications requiring high voltages with relatively lower operation times.

From the discharge results shown in Figure 4.34, the internal resistances were calculated by Equation (3.1). The internal resistance calculations were performed at the start and end of the pulses separately. The former region is investigated to observe the immediate resistance reflected by the cells, whereas the latter region is investigated to determine the kinetic effects. The trend of internal resistance changes is given in Figure 4.35.

As given in Figure 4.35 (a-b), the resistance values of the cells at 475 °C show similar trends at the start and end of the pulses, however, the resistance values are higher at the end of the pulses than at the beginning. Although there are few regions between 0-100 seconds where high entropy disulfides have lower resistance than reference FeS_2, at most of the discharge periods, they show higher resistance values. The resistance values of high entropy disulfides are higher than the pyrite for nearly all of the discharge periods at 525 °C, as shown in Figure 4.35 (c-d). The difference in the resistance values between the high entropy disulfides and conventional FeS_2

becomes higher at the end of the pulses. At 575 °C, shown in Figure 4.35 (e-f), (FeNiCoCrMn)S_2 – 7 mm shows similar resistance values with FeS_2 for almost 250 seconds discharge time, however, (FeNiCoCrMn)S_2 – 5 mm show higher resistances after 150 seconds. These results indicate they have relatively less conductivity and enhancing this property may increase the cell performance and expand operation times.
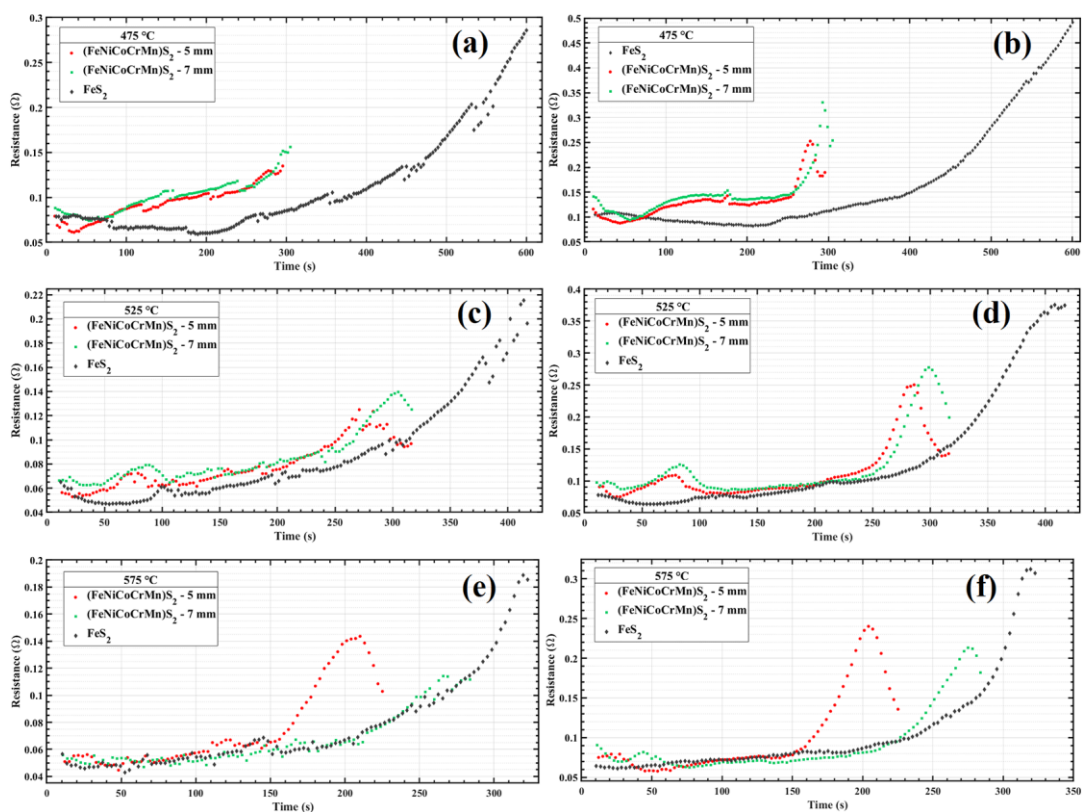
Figure 4.35 Internal resistances of single cells with (FeNiCoCrMn)S_2 – 5 mm, (FeNiCoCrMn)S_2 – 7 mm, and conventional FeS_2 cathodes at 475 °C (a, b), 525 °C (c, d), and 575 °C (e, f) discharge temperatures, calculated at the start of the pulses (a, c, e) and the end of the pulses (b, d, f).

Based on the discharge curves in Figure 4.34, several cut-off voltages are chosen to compare specific capacities and energies of (FeNiCoCrMn)S_2 – 5 mm and (FeNiCoCrMn)S_2 – 7 mm high entropy disulfides with the reference FeS_2. The chosen cut-off voltages are given in Table 4.3.

Table 4.3 Cut-off voltages chosen for comparison of the specific capacities and energies of (FeNiCoCrMn)S$_2$ – 5 mm, (FeNiCoCrMn)S$_2$ – 7 mm, and conventional FeS$_2$ cathodes at different discharge temperatures.

Single Cell Test Temperature (°C)	Cut-off Voltage (V)
475	1.80
	1.75
525	1.80
	1.30
575	1.30

The confined discharge results obtained with selected cut-off voltages at discharge temperatures of 475 °C, 525 °C, and 575 °C are shown in Figure 4.36.

From the confined discharge results shown in Figure 4.36, the specific capacities and energies at different cut-off voltages are calculated by Equation (3.2) and Equation (3.3), respectively. The capacity and energy results are given in Table 4.4.
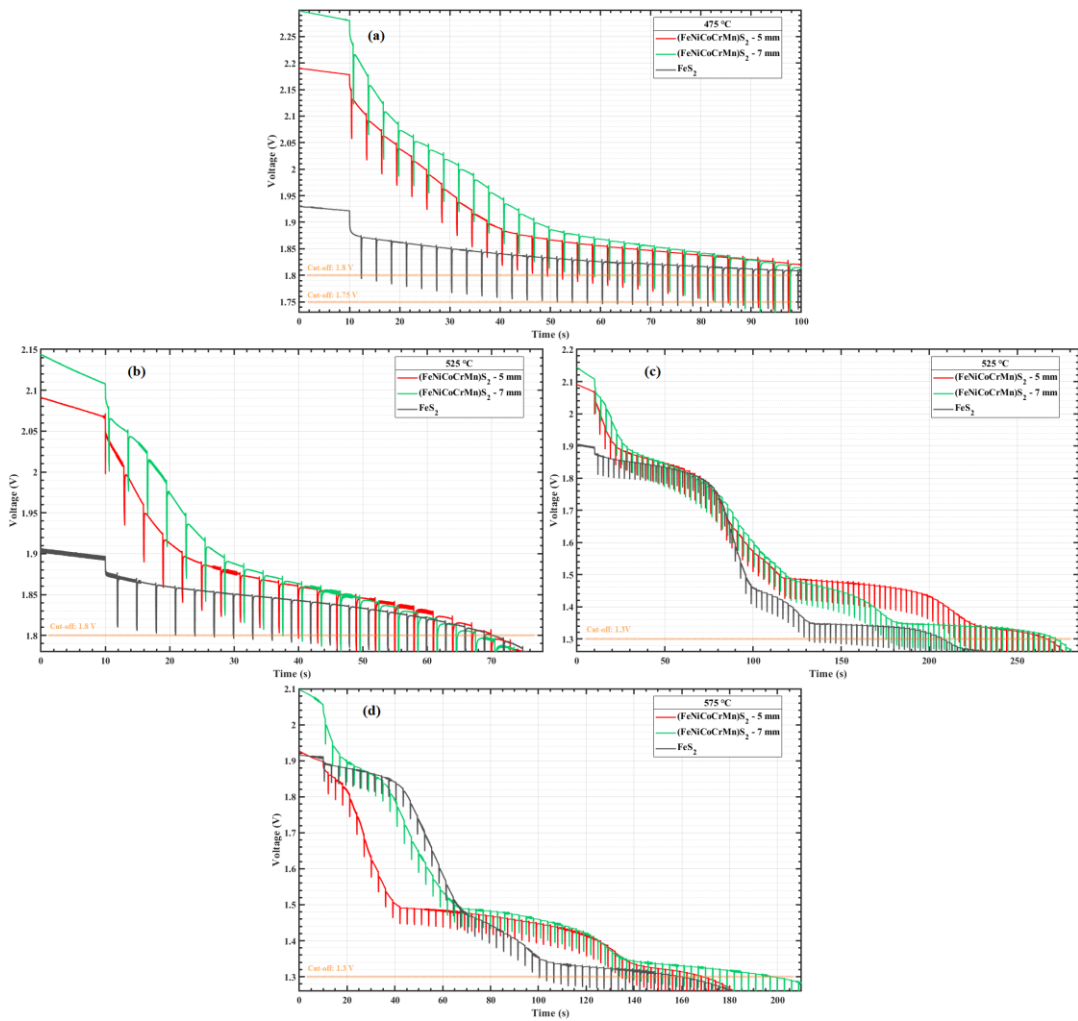
Figure 4.36 Discharge curves of single cells with (FeNiCoCrMn)S_2 – 5 mm, (FeNiCoCrMn)S_2 – 7 mm, and conventional FeS_2 cathodes at (a) 475 °C, (b-c) 525 °C, and (d) 575 °C discharge temperatures with different cut-off voltages.

Table 4.4 Specific capacity and energy results of single cells with (FeNiCoCrMn)S_2 – 5 mm, (FeNiCoCrMn)S_2 – 7 mm, and conventional FeS_2 cathodes at different discharge temperatures and cut-off voltages.

Cathode Material	Single Cell Test Temperature (°C)	Open Circuit Voltage (V)	Cut-off Voltage (V)	Specific Capacity (mAh g⁻¹)	Specific Energy (Wh kg⁻¹)
(FeNiCoCrMn)S_2 5 mm	475	2.19	1.80	49.18	96.71
			1.75	92.84	177.05
	525	2.09	1.80	39.37	75.19
			1.30	262.33	422.74
	575	1.93	1.30	159.94	241.87
(FeNiCoCrMn)S_2 7 mm	475	2.30	1.80	62.42	124.46
			1.75	92.62	180.15
	525	2.14	1.80	36.44	71.01
			1.30	209.75	347.95
	575	2.10	1.30	162.66	257.71
FeS_2	475	1.93	1.80	3.12	5.88
			1.75	50.43	92.90
	525	1.91	1.80	15.37	28.62
			1.30	154.81	260.11
	575	1.92	1.30	115.35	189.91

As shown in Table 4.4, the specific capacity and energy of single cells with (FeNiCoCrMn)S_2 – 7 mm cathode at 475 °C with the cut-off voltage of 1.75 V is 83.6% and 93.9% higher than conventional FeS_2, respectively. If the operation time is decreased and the cut-off voltage is chosen as 1.8 V, the specific capacity and energy difference becomes extremely high which are 1900% and 2015.1% thanks to high entropy sulfides elevated maximum voltages. The specific capacity and energy

of (FeNiCoCrMn)S_2 – 5 mm cathodes are also superior to FeS_2 with these conditions. When the cut-off voltage is 1.75 V, single cells with (FeNiCoCrMn)S_2 – 5 mm cathode have 84.1% and 90.6% higher specific capacity and energy than pyrite, respectively. These values become 1475.7% and 1543.5% if the operation time shortens with the cut-off voltage of 1.8 V.

When the discharge temperature is 525 °C, the dominance of discharge performances of high entropy disulfides broadens from lower operation times to expanded times. Owing to relatively higher open circuit voltages, they still exhibit superior specific capacity and energy to FeS_2 when the cut-off voltage is 1.8 V. The specific capacity and energy of single cells with (FeNiCoCrMn)S_2 – 5 mm cathode are 156.2% and 162.7% higher than conventional FeS_2, respectively. The electrochemical performance of (FeNiCoCrMn)S_2 – 7 mm cathodes is also excellent compared to reference pyrite with these conditions. Single cells with (FeNiCoCrMn)S_2 – 7 mm cathode have 137.1% and 148.1% higher specific capacity and energy than pyrite, respectively. As distinct from the results of 475 °C, increasing the discharge time at 525 °C still preserves the significant capacity and energy increases of high entropy disulfides. When the cut-off voltage is 1.3 V, the specific capacity and energy of (FeNiCoCrMn)S_2 – 5 mm and (FeNiCoCrMn)S_2 – 7 mm are substantially better than that of the conventional FeS_2. The specific capacity and energy of single cells with (FeNiCoCrMn)S_2 – 5 mm cathode with the cut-off voltage of 1.3 V are 69.4% and 62.5% higher than pyrite, respectively. Under the same conditions, (FeNiCoCrMn)S_2 – 7 mm cathode also performs 35.5% and 33.8% higher discharge capacity and energy than that of pyrite, respectively.

Elevating the discharge temperature from 525 °C to 575 °C negatively affects the performance at lower operation times. However, further operation times with the cut-off voltage of 1.3 V reflect attractive specific capacity and energy difference between the high entropy disulfide and the conventional pyrite cathodes. (FeNiCoCrMn)S_2 – 7 mm presents 41% and 35.7% higher specific capacity and energy than that of pyrite. In these conditions, (FeNiCoCrMn)S_2 – 5 mm have 38.7% and 27.4% higher capacity and energy in comparison with FeS_2.

These results suggest that high entropy disulfides may provide significant electrochemical performance improvements under specific discharge conditions. Although their internal resistances are mostly higher throughout the discharge period and their thermal stabilities are relatively lower than that of pyrite, the higher operation voltages and synergistic effects of multiple principal elements may compensate for the disadvantages and also provide important specific capacity and energy enhancements.

4.6.3 Electrochemical Performance of the $(FeNiCo_{0.35}CrMn)S_2$ and $(FeNiCoCuTi)S_2$ High Entropy Disulfides

Figure 4.37 demonstrates the discharge curves of the single cells with $(FeNiCo_{0.35}CrMn)S_2$ and $(FeNiCoCuTi)S_2$ high entropy disulfide cathodes synthesized by high energy ball milling process with a comparison of conventional FeS_2 (pyrite) cathode at different single cell discharge temperatures of 475 °C, 525 °C, and 575 °C. Similar to single cells with $(FeNiCoCrMn)S_2$ cathodes, both $(FeNiCo_{0.35}CrMn)S_2$ and $(FeNiCoCuTi)S_2$ cathodes have also higher open circuit voltages than that of conventional FeS_2 cathodes. The maximum voltage difference is distinct at 475 °C, where the single cells with $(FeNiCo_{0.35}CrMn)S_2$, $(FeNiCoCuTi)S_2$, and reference FeS_2 cathodes exhibit 2.22 V, 2.08 V, and 1.93 V, respectively. The open circuit voltages of $(FeNiCo_{0.35}CrMn)S_2$ and $(FeNiCoCuTi)S_2$ cathodes at 525 °C are 2.11 V and 2.08 V showing elevated maximum voltages than that of FeS_2 with an open circuit voltage of 1.93 V. The decreasing of open circuit voltage values at 575 °C observed in single cell tests of $(FeNiCoCrMn)S_2$ cathodes is also seen remarkably for $(FeNiCo_{0.35}CrMn)S_2$ and $(FeNiCoCuTi)S_2$ cathodes. At this temperature, the open circuit voltage of $(FeNiCoCuTi)S_2$ cathodes becomes 1.91 V which is lower than the reference pyrite having a 1.93 V maximum voltage. Although $(FeNiCo_{0.35}CrMn)S_2$ performed better than these with an open circuit voltage of 1.94 V, the difference between the high entropy sulfide cathodes with the pyrite is decreased. However, the results indicate that by modifying the high entropy

sulfide structure by changing the principal elements or molar ratios of the elements complying with the high entropy requirements, open circuit voltages may be tuned for desired applications.

Figure 4.37 Discharge curves of single cells with (FeNiCo$_{0.35}$CrMn)S$_2$, (FeNiCoCuTi)S$_2$, and conventional FeS$_2$ cathodes at (a) 475 °C, (b) 525 °C, and (c) 575 °C discharge temperatures.

Figure 4.37 also depicts that $(FeNiCoCuTi)S_2$ significantly enhances the operation times and shows the capability of high entropy sulfides at relatively longer discharge periods. Although its maximum voltage values are lower than that of $(FeNiCo_{0.35}CrMn)S_2$, the $(FeNiCoCuTi)S_2$ cathode exhibits superior performance and outperforms the conventional pyrite regarding discharging times at 525 °C and 575 °C. Despite the single cell with conventional pyrite cathode having a longer discharging time than that of $(FeNiCoCuTi)S_2$ cathode at 475 °C, the more stable discharging characteristics of $(FeNiCoCuTi)S_2$ can also be clearly seen compared to $(FeNiCo_{0.35}CrMn)S_2$ which shows faster voltage drops after nearly 100 seconds. $(FeNiCo_{0.35}CrMn)S_2$, on the other hand, exhibits a substantial discharge performance at 575 °C. This enhanced high temperature performance may be attributed to relatively higher cobalt content increasing the thermal stability of the material without losing the high entropy features such as the cocktail effect and improved stability.

From the discharge results shown in Figure 4.37, the internal resistances were calculated by Equation (3.1). The internal resistance calculations were performed at the start and end of the pulses separately. The former region is investigated to observe the immediate resistance reflected by the cells, whereas the latter region is investigated to determine the kinetic effects. The trend of internal resistance changes is given in Figure 4.38.

As shown in Figure 4.38 (a), at the discharge temperature of 475 °C, both of the high entropy disulfides show higher internal resistance values than FeS_2 at the start of the pulses except for $(FeNiCoCuTi)S_2$ before 60 seconds of discharge time. However, after applying the pulse loads for nearly 100 milliseconds, at the end of the pulses, the single cell with $(FeNiCoCuTi)S_2$ shows relatively decreased internal resistance values especially at higher operation times after 360 seconds as given in Figure 4.38 (b). In these regions, $(FeNiCoCuTi)S_2$ shows lower resistances than FeS_2, whereas $(FeNiCo_{0.35}CrMn)S_2$ shows relatively higher resistances. At 525 °C, as given in Figure 4.38 (c-d), the single cell with $(FeNiCo_{0.35}CrMn)S_2$ cathode again shows higher resistances for most discharge periods than conventional FeS_2 cathode. As

distinct from $(FeNiCo_{0.35}CrMn)S_2$, $(FeNiCoCuTi)S_2$ high entropy disulfides exhibit relatively lower resistances and enhance the conductivity of the cells even at the end of the pulses. That positive effect on conductivity is mostly apparent for discharge periods after 250 seconds where the single cells with $(FeNiCoCuTi)S_2$ cathode have distinctively lower resistances than conventional FeS_2. When the discharge temperature is 575 °C, as shown in Figure 4.38 (e-f), the resistance values of $(FeNiCo_{0.35}CrMn)S_2$ substantially decrease and become lower than FeS_2 after 150 seconds of discharge time both at the start and end of the pulses. For $(FeNiCoCuTi)S_2$ cathode, the internal resistance calculations show similar results with FeS_2 but since it shows expanded operation times, it reflects relatively lower resistance values at increased discharge times. The reduced resistances may result from the inherent low electrical resistivity and thus high conductivity of the copper. The results suggest that even if only one principal element having high electrical conductivity such as copper is incorporated in the structure, the relatively high resistance of the high entropy disulfides can be decreased and operation times can be enlarged.
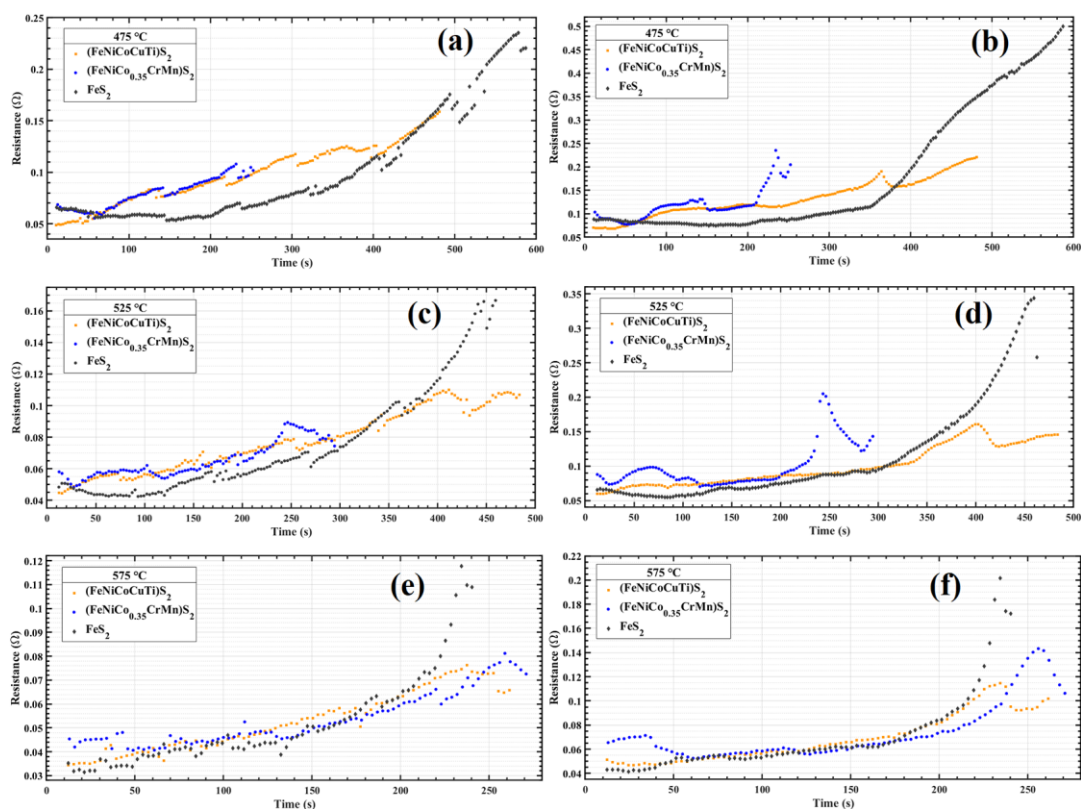
Figure 4.38 Internal resistances of single cells with $(FeNiCo_{0.35}CrMn)S_2$, $(FeNiCoCuTi)S_2$, and conventional FeS_2 cathodes at 475 °C (a, b), 525 °C (c, d), and 575 °C (e, f) discharge temperatures, calculated at the start of the pulses (a, c, e) and the end of the pulses (b, d, f).

Based on the discharge curves in Figure 4.37, several cut-off voltages are chosen to compare specific capacities and energies of $(FeNiCo_{0.35}CrMn)S_2$ and $(FeNiCoCuTi)S_2$ high entropy disulfides with the reference FeS_2. The chosen cut-off voltages are given in Table 4.5.

Table 4.5 Cut-off voltages chosen for comparison of the specific capacities and energies of $(FeNiCo_{0.35}CrMn)S_2$, $(FeNiCoCuTi)S_2$, and conventional FeS_2 cathodes at different discharge temperatures.

Single Cell Test Temperature (°C)	Cut-off Voltage (V)
475	1.80
525	1.35
	1.10
575	1.40

The confined discharge results obtained with selected cut-off voltages at discharge temperatures of 475 °C, 525 °C, and 575 °C are shown in Figure 4.39.

From the confined discharge results shown in Figure 4.39, the specific capacities and energies at different cut-off voltages are calculated by Equation (3.2) and Equation (3.3), respectively. The capacity and energy results are given in Table 4.6.
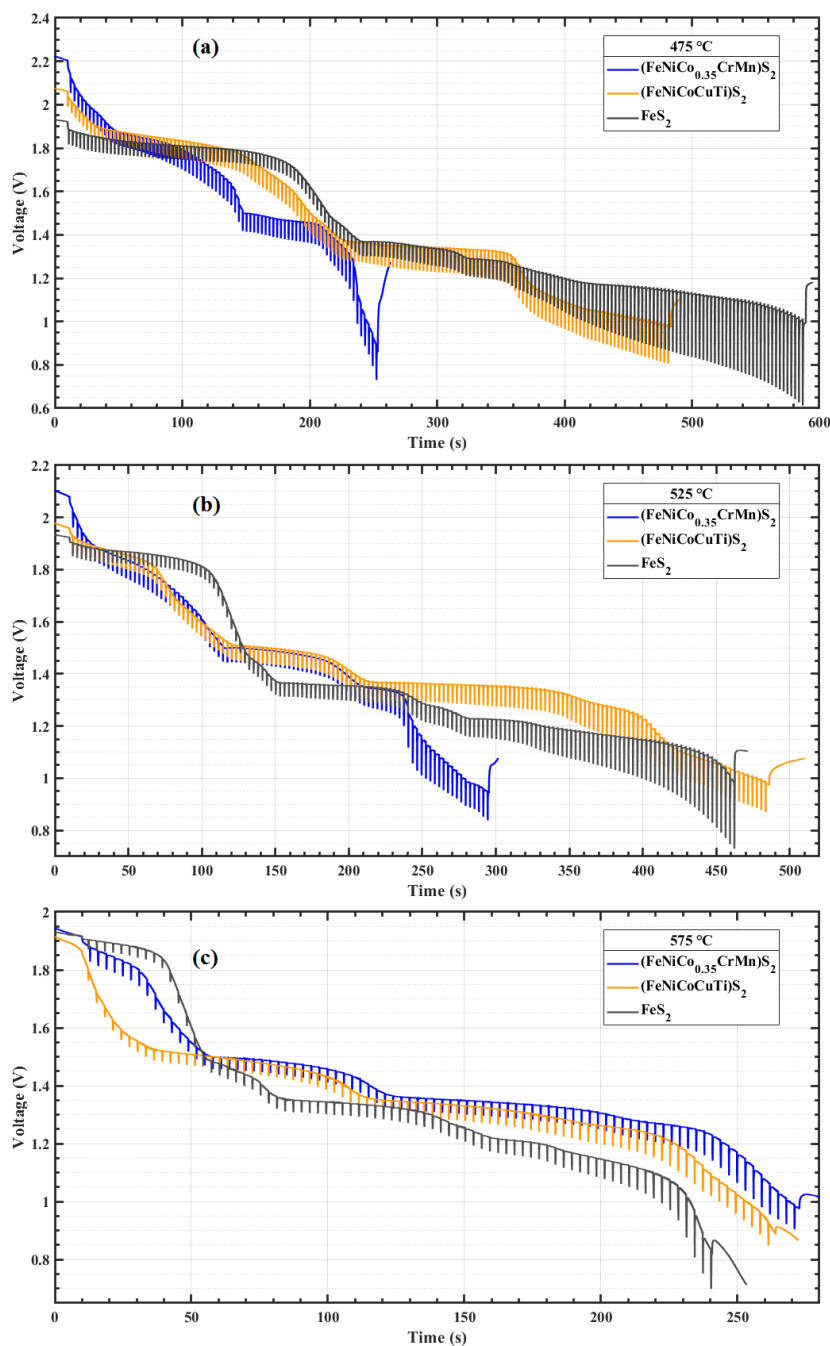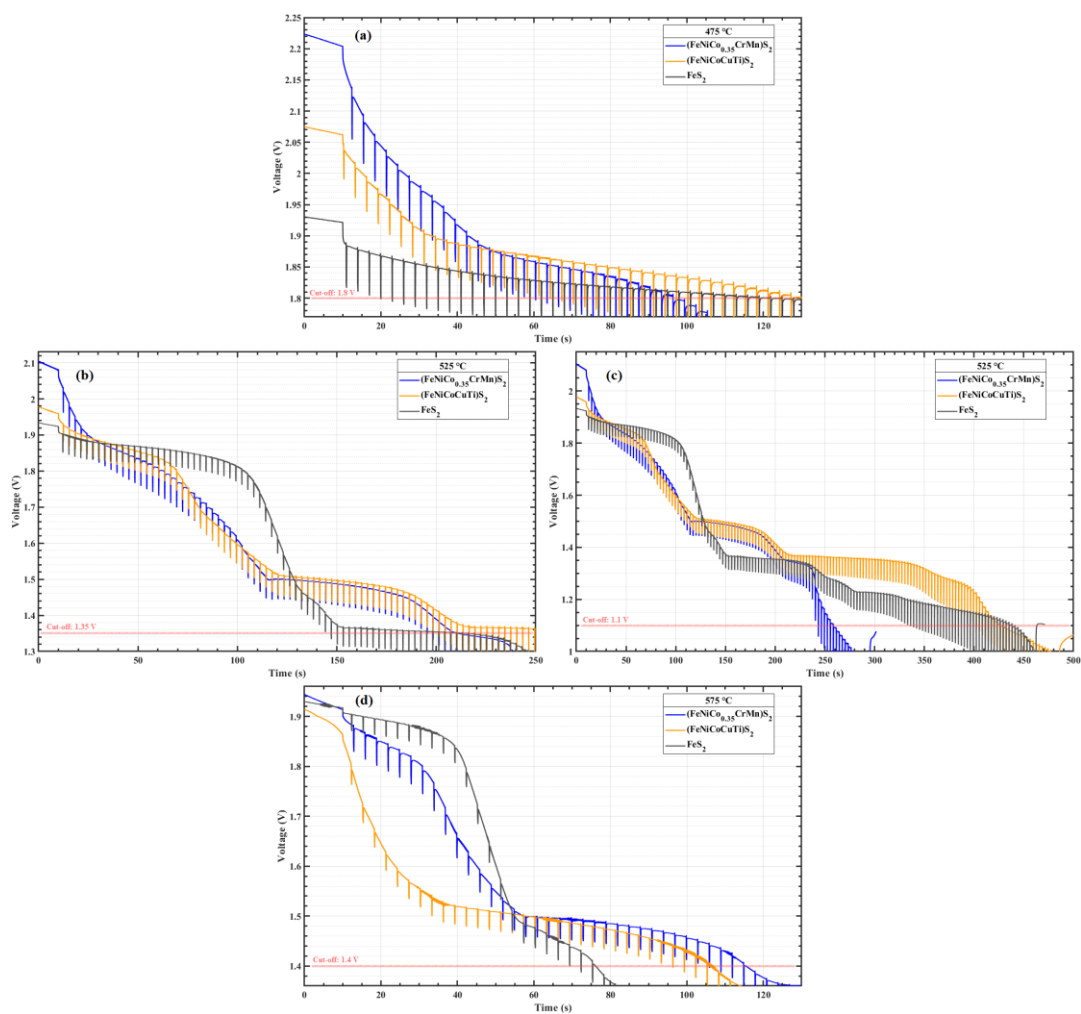
Figure 4.39 Discharge curves of single cells with $(FeNiCo_{0.35}CrMn)S_2$, $(FeNiCoCuTi)S_2$, and conventional FeS_2 cathodes at (a) 475 °C, (b-c) 525 °C, and (d) 575 °C discharge temperatures with different cut-off voltages.

Table 4.6 Specific capacity and energy results of single cells with $(FeNiCo_{0.35}CrMn)S_2$, $(FeNiCoCuTi)S_2$, and conventional FeS_2 cathodes at different discharge temperatures and cut-off voltages.

Cathode Material	Single Cell Test Temperature (°C)	Open Circuit Voltage (V)	Cut-off Voltage (V)	Specific Capacity (mAh g⁻¹)	Specific Energy (Wh kg⁻¹)
$(FeNiCo_{0.35}CrMn)S_2$	475	2.22	1.80	57.79	113.00
	525	2.11	1.35	219.67	360.10
			1.10	276.14	435.23
	575	1.94	1.40	115.72	184.75
$(FeNiCoCuTi)S_2$	475	2.08	1.80	61.61	117.50
	525	1.98	1.35	224.70	367.66
			1.10	460.78	680.31
	575	1.91	1.40	103.92	159.08
FeS_2	475	1.93	1.80	13.28	24.87
	525	1.93	1.35	160.01	282.20
			1.10	380.93	566.71
	575	1.93	1.40	71.42	123.15

As shown in Table 4.6, the specific capacity and energy of single cells with $(FeNiCoCuTi)S_2$ cathode at 475 °C with the cut-off voltage of 1.80 V are 363.8% and 372.5% higher than conventional FeS_2, respectively. That enhanced electrochemical performance of high entropy disulfides for relatively lower discharge times with the cut-off voltage of 1.80 V is also seen for $(FeNiCo_{0.35}CrMn)S_2$ cathode. It shows 335.1% and 354.4% higher specific capacity and energy than pyrite, respectively.

If the discharge temperature is changed to 525 °C, high entropy disulfides show better overall performances than the reference pyrite, especially $(FeNiCoCuTi)S_2$

considering the total discharge time. The single cell containing $(FeNiCoCuTi)S_2$ cathode reaches 40.4% and 30.3% higher specific capacity and energy values than conventional FeS_2, respectively with a cut-off voltage of 1.35 V. Even if the cut-off voltage is 1.10 V, the high entropy disulfide performs 21% and 20% higher specific capacity and energy than that of pyrite, respectively. These results suggest that $(FeNiCoCuTi)S_2$ may be utilized for applications that require longer operating times to achieve higher discharge capacity and energy performance with relatively lower weights than pyrite. Besides $(FeNiCoCuTi)S_2$, $(FeNiCo_{0.35}CrMn)S_2$ cathode also shows higher specific capacity and energy than FeS_2 with the cut-off voltage of 1.35 V. The single cell with $(FeNiCo_{0.35}CrMn)S_2$ cathode exhibits 37.3% and 27.6% higher specific capacity and energy than conventional FeS_2, respectively.

The discharge evaluation at 575 °C argues that $(FeNiCo_{0.35}CrMn)S_2$ cathode outperforms reference FeS_2 for most of the discharging periods. Although the electrochemical performance difference between the single cells with $(FeNiCo_{0.35}CrMn)S_2$ cathode and pyrite can be seen for the entire discharging time, the difference is most obvious when the cut-off voltage is 1.40 V. Under these conditions, the specific capacity and energy of $(FeNiCo_{0.35}CrMn)S_2$ cathode is 62% and 50% higher than that of FeS_2, respectively. The results show that $(FeNiCo_{0.35}CrMn)S_2$ is especially more suitable for high temperature applications in comparison with the other high entropy sulfides. In addition, despite the electrochemical performance of $(FeNiCoCuTi)S_2$ being relatively lower than that of $(FeNiCo_{0.35}CrMn)S_2$, $(FeNiCoCuTi)S_2$ cathode also exhibit 45.5% and 29.2% higher specific capacity and energy than reference pyrite at 575 °C with the cut-off voltage of 1.40 V.

These results propose that by changing the elemental compositions, the disadvantages of high entropy disulfides faced in the first single cell discharge tests explained in 4.6.2 may be eliminated. Their relatively higher internal resistances are successfully decreased by incorporating copper to the structure and lower thermal decomposition temperatures are increased by elevating the molar ratio of the cobalt.

Thus, it can be deduced that the electrochemical performance of the high entropy sulfides could be manipulated to fulfill the requirements of the specific applications.

4.6.4 Comparison of Electrochemical Performances of High Entropy Disulfides Synthesized with the Same Ball Diameters

Since the single cells containing reference FeS_2 cathodes showed similar electrochemical characteristics within the limits of production repeatability in the experiments, it is evaluated that a comparison between high entropy sulfides prepared by WC balls having the same diameters within each other can be made. These comparisons explain the effect of compositional fractions and different primary materials in detail for high entropy disulfides.

4.6.4.1 Comparison of Electrochemical Performances of High Entropy Disulfides Synthesized with 5 mm Diameter WC Balls

Figure 4.40 shows the discharge curves of the single cells with $(FeNiCoCrMn)S_2$ and $(FeNiCo_{0.35}CrMn)S_2$ high entropy disulfide cathodes synthesized using WC balls with 5 mm diameter in high energy ball milling process at different single cell discharge temperatures of 475 °C, 525 °C, and 575 °C.

The discharge plots depict that increasing the molar fraction of the cobalt element slightly increase open circuit voltage of $(FeNiCoCrMn)S_2$ cathodes. The open circuit voltages of $(FeNiCo_{0.35}CrMn)S_2$ cathode are 2.22 V, 2.11 V, and 1.94 V at 475 °C, 525 °C, and 575 °C, respectively. At these discharge temperatures $(FeNiCoCrMn)S_2$ cathodes show 2.19 V, 2.09 V, and 1.93 V, respectively. Although the open circuit voltage difference is low, the results indicate that altering the molar fractions directly affects the open circuit voltage values and leads to tunability of maximum voltages of the cells.

Figure 4.40 Discharge curves of single cells with (FeNiCoCrMn)S_2 and (FeNiCo$_{0.35}$CrMn)S_2 cathodes which are synthesized by WC balls with 5 mm diameters at a) 475 ℃, b) 525 ℃, and c) 575 ℃ discharge temperatures.

96

Furthermore, a comparison of the discharge performances of $(FeNiCoCrMn)S_2$ and $(FeNiCo_{0.35}CrMn)S_2$ cathodes shows that $(FeNiCoCrMn)S_2$ mostly performs better than $(FeNiCo_{0.35}CrMn)S_2$ at relatively lower temperatures. On the contrary, $(FeNiCo_{0.35}CrMn)S_2$ outperforms $(FeNiCoCrMn)S_2$ at higher discharging temperatures thanks to the contribution of more cobalt elements in the structure. Having a slightly higher open circuit voltage leads $(FeNiCo_{0.35}CrMn)S_2$ to perform better than $(FeNiCoCrMn)S_2$ at 475 °C for a limited short time before nearly 20 seconds of the discharge. Then, $(FeNiCoCrMn)S_2$ outperforms the former cathode for most of the discharge periods with an expanded operating time. At 525 °C, the performance difference between $(FeNiCo_{0.35}CrMn)S_2$ and $(FeNiCoCrMn)S_2$ is similar to that of 475 °C. $(FeNiCoCrMn)S_2$ shows better discharge performance, especially with longer discharging times. Nevertheless, improved thermal stabilities of $(FeNiCo_{0.35}CrMn)S_2$ provide an enhanced discharge performance at 575 °C. For almost the entire discharge period, the single cell with $(FeNiCo_{0.35}CrMn)S_2$ cathode exhibits much better electrochemical performance than the single cell with $(FeNiCoCrMn)S_2$ and reflects substantially increased discharging time.

From the discharge results shown in Figure 4.40, the internal resistances were calculated by Equation (3.1). The internal resistance calculations were performed at the start and end of the pulses separately. The former region is investigated to observe the immediate resistance reflected by the cells, whereas the latter region is investigated to determine the kinetic effects. The trend of internal resistance changes is given in Figure 4.41.

The internal resistance curves given in Figure 4.41 (a-b) show that at discharge temperature of 475 °C, $(FeNiCo_{0.35}CrMn)S_2$ shows relatively lower resistance values at the start of the pulses whereas at the end of pulses with higher discharge times than 200 seconds, the resistance values $(FeNiCoCrMn)S_2$ becomes lower than that of $(FeNiCo_{0.35}CrMn)S_2$. As given in Figure 4.41 (c-d), at 525 °C discharge temperature, similar internal resistance trends are obtained at 475 °C. However, elevating the discharge temperature to 575 °C leads to more significant differences in resistance values. As shown in Figure 4.41 (e-f), $(FeNiCo_{0.35}CrMn)S_2$ cathode has

remarkably lower internal resistances than that of (FeNiCoCrMn)S_2 cathodes both for the beginning and the end of the pulse regions. These results suggest that increasing the cobalt content reduces the internal resistances and increases the overall conductivity for most of the discharge periods at elevated discharge temperatures. The enhancement of the conductivity may be attributed to the highest inherent electrical conductivity of cobalt when compared to the other elements in the structure.
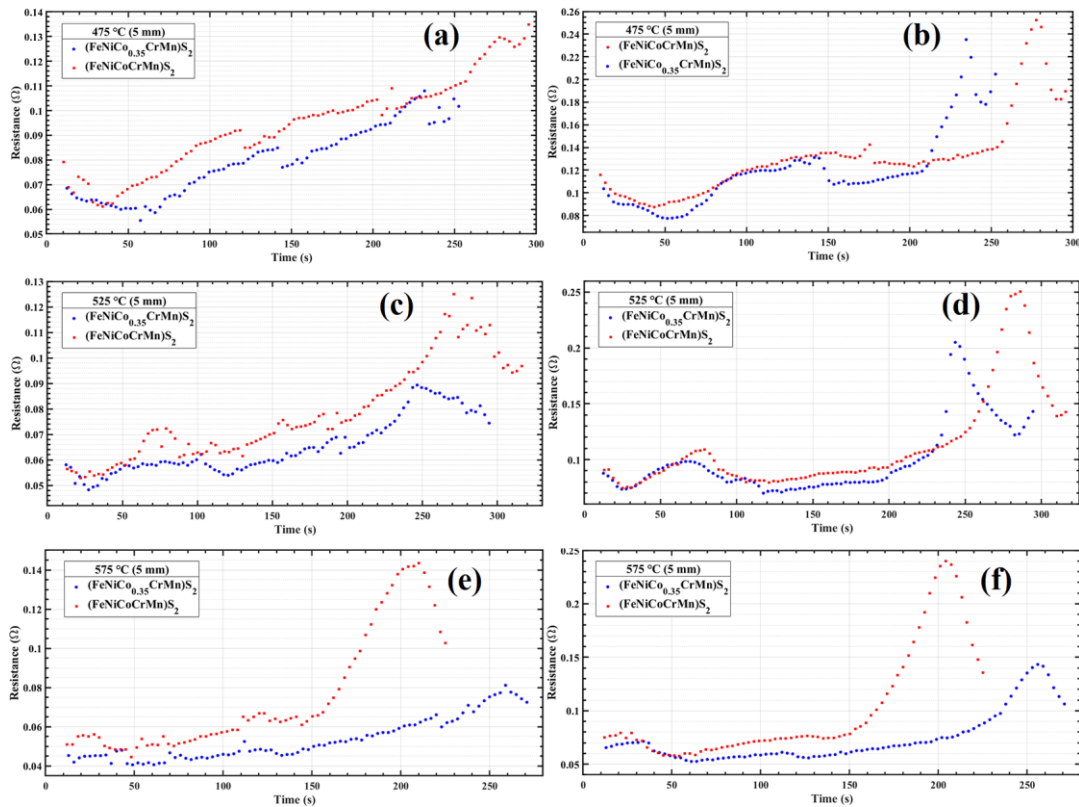
Figure 4.41 Internal resistances of single cells with (FeNiCoCrMn)S_2 and (FeNiCo$_{0.35}$CrMn)S_2 cathodes which are synthesized by WC balls with 5 mm diameters 475 °C (a, b), 525 °C (c, d), and 575 °C (e, f) discharge temperatures, calculated at the start of the pulses (a, c, e) and the end of the pulses (b, d, f).

Based on the discharge curves in Figure 4.40, several cut-off voltages are chosen to compare specific capacities and energies of (FeNiCoCrMn)S_2 and (FeNiCo$_{0.35}$CrMn)S_2 high entropy disulfides. The chosen cut-off voltages are given in Table 4.7.

Table 4.7 Cut-off voltages chosen for comparison of the specific capacities and energies of $(FeNiCoCrMn)S_2$ and $(FeNiCo_{0.35}CrMn)S_2$ cathodes at different discharge temperatures.

Single Cell Test Temperature (°C)	Cut-off Voltage (V)
475	1.80
	1.50
	1.20
525	1.20
575	1.80
	1.50
	1.20

The confined discharge results obtained with selected cut-off voltages at discharge temperatures of 475 °C, 525 °C, and 575 °C are shown in Figure 4.42.

From the confined discharge results shown in Figure 4.42, the specific capacities and energies at different cut-off voltages are calculated by Equation (3.2) and Equation (3.3), respectively. The capacity and energy results are given in Table 4.8.
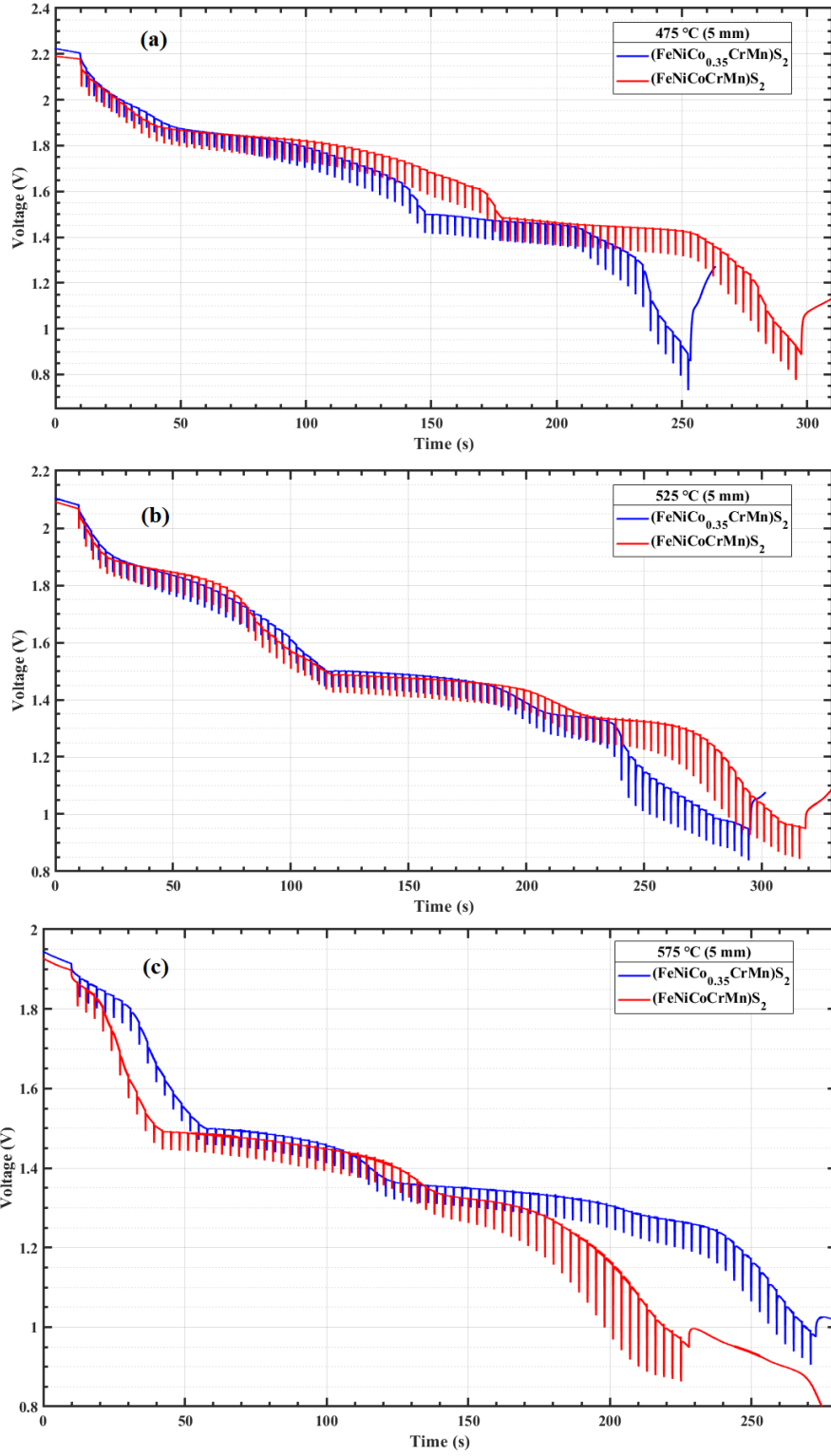
99
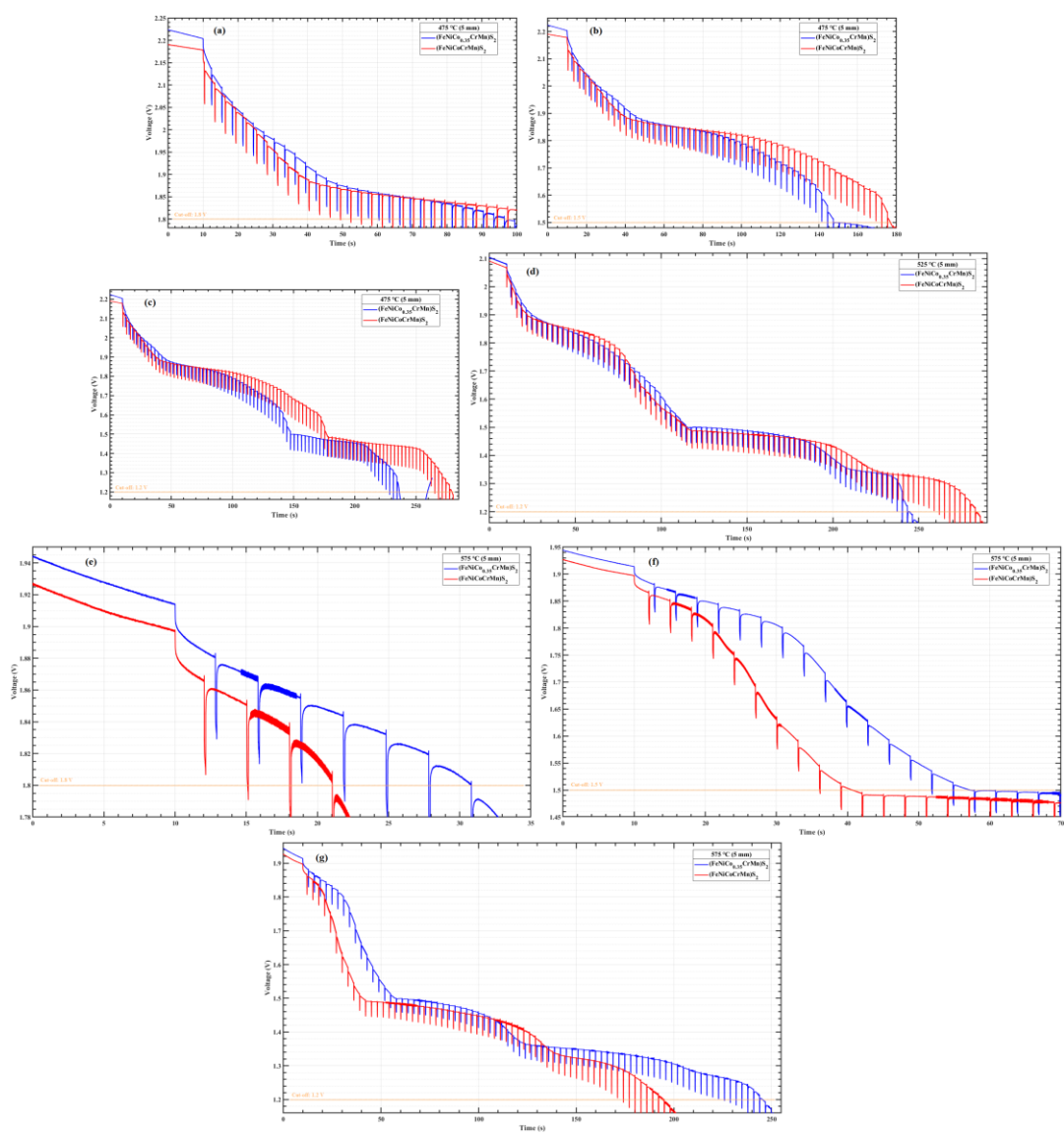
Figure 4.42 Discharge curves of single cells with $(FeNiCoCrMn)S_2$ and $(FeNiCo_{0.35}CrMn)S_2$ cathodes which are synthesized by WC balls with 5 mm diameters at (a-c) 475 ℃, (d) 525 ℃, and (e-g) 575 ℃ discharge temperatures with different cut-off voltages.

Table 4.8 Specific capacity and energy results of single cells with $(FeNiCoCrMn)S_2$ and $(FeNiCo_{0.35}CrMn)S_2$ cathodes which are synthesized by WC balls with 5 mm diameters at different discharge temperatures and cut-off voltages.

Cathode Material	Single Cell Test Temperature (°C)	Open Circuit Voltage (V)	Cut-off Voltage (V)	Specific Capacity (mAh g⁻¹)	Specific Energy (Wh kg⁻¹)
$(FeNiCo_{0.35}CrMn)S_2$	475	2.22	1.80	57.79	113.00
			1.50	153.43	280.65
			1.20	249.77	419.53
	525	2.11	1.20	249.77	419.53
	575	1.94	1.80	14.83	27.67
			1.50	50.69	88.64
			1.20	259.68	376.28
$(FeNiCoCrMn)S_2$ 5 mm	475	2.19	1.80	49.18	96.71
			1.50	197.97	359.06
			1.20	311.29	521.73
	525	2.09	1.20	319.17	498.01
	575	1.93	1.80	7.89	14.75
			1.50	34.47	60.10
			1.20	209.40	306.66

As given in Table 4.8, the specific capacity and energy of single cells with $(FeNiCo_{0.35}CrMn)S_2$ cathode at 475 °C with the cut-off voltage of 1.80 V is 17.5% and 16.8% higher than $(FeNiCoCrMn)S_2$ cathode, respectively. In case the operating time is enlarged and the cut-off voltages are chosen as 1.50 V and 1.20 V, the electrochemical performance of the $(FeNiCoCrMn)S_2$ cathode outperforms the $(FeNiCo_{0.35}CrMn)S_2$ cathode. When the cut-off voltage is 1.50 V, single cells with $(FeNiCoCrMn)S_2$ cathode have 29% and 27.9% higher specific capacity and energy

than $(FeNiCo_{0.35}CrMn)S_2$, respectively. These rates change to 24.6% and 24.4% if the cut-off voltage becomes 1.20 V.

When the discharge temperature is 525 °C and the cut-off voltage is 1.20 V, the specific capacity and energy of single cells with $(FeNiCoCrMn)S_2$ cathode are 27.8% and 18.7% higher than $(FeNiCo_{0.35}CrMn)S_2$, respectively.

Increasing the discharge temperature to 575 °C completely changes the specific capacity and energy comparison between the $(FeNiCoCrMn)S_2$ and $(FeNiCo_{0.35}CrMn)S_2$ cathodes. For most of the discharge periods, $(FeNiCo_{0.35}CrMn)S_2$ cathode exhibits infinitely better discharge performance thanks to its improved thermal stability. $(FeNiCo_{0.35}CrMn)S_2$ can achieve 87.9% and 87.6% higher specific capacity and energy than that of $(FeNiCoCrMn)S_2$ with the cut-off voltage of 1.80 V. When the cut-off voltage is 1.50 V, single cells with $(FeNiCo_{0.35}CrMn)S_2$ cathode exhibit 47% and 47.5% higher specific capacity and energy than $(FeNiCoCrMn)S_2$, respectively. If the operation time is extended and the cut-off voltage is chosen as 1.20 V, these performance gains become 24% and 22.7%, respectively.

These results suggest that increasing the mole fraction of cobalt element in $(FeNiCoCrMn)S_2$ high entropy disulfides may provide an excellent performance gain at elevated discharge temperatures. However, the discharge performance of the modified high entropy disulfide with higher cobalt content for longer operation times at relatively lower temperatures can be slightly worse than $(FeNiCoCrMn)S_2$ high entropy disulfides containing equimolar cations. Therefore, fine adjustments on the molar ratios may be applied to achieve the desired properties at different operation conditions of the batteries. This tunability of the stoichiometries and properties of the high entropy sulfides may create new design routes for application specific cathode materials.

4.6.4.2   Comparison of Electrochemical Performances of High Entropy Disulfides Synthesized with 7 mm Diameter WC Balls

Figure 4.43 shows the discharge curves of the single cells with $(FeNiCoCrMn)S_2$ and $(FeNiCoCuTi)S_2$ high entropy disulfide cathodes synthesized using WC balls with 7 mm diameter in high energy ball milling process at different single cell discharge temperatures of 475 ℃, 525 ℃, and 575 ℃.

The discharge curves show that replacing chromium and manganese with copper and titanium in the $(FeNiCoCrMn)S_2$ high entropy disulfide cathode decreases the open circuit voltage. The open circuit voltages of $(FeNiCoCuTi)S_2$ at 475 ℃, 525 ℃, and 575 ℃ are 2.08 V, 1.98 V, and 1.91 V, respectively. At these discharge temperatures $(FeNiCoCrMn)S_2$ cathodes exhibit 2.30 V, 2.14 V, and 2.10 V open circuit voltages, respectively. The results propose that incorporating different principal elements in the high entropy disulfide structure has a great impact on the maximum voltage of the designed material. Therefore, the open circuit voltage of the battery may be manipulated by simply substituting the elements and these manipulations can make the compliance of strict design requirements available.

Figure 4.43 Discharge curves of single cells with (FeNiCoCrMn)S_2 and (FeNiCoCuTi)S_2 cathodes which are synthesized by WC balls with 7 mm diameters at a) 475 °C, b) 525 °C, and c) 575 °C discharge temperatures.

Additionally, a comparison of the discharge performances of $(FeNiCoCrMn)S_2$ and $(FeNiCoCuTi)S_2$ cathodes at 475 °C and 525 °C depicts that the discharge times when using the single cells with $(FeNiCoCuTi)S_2$ cathodes are dramatically extended. In these conditions, the $(FeNiCoCuTi)S_2$ cathode shows more stable and long-continued discharge characteristics whereas the $(FeNiCoCrMn)S_2$ cathode exhibits relatively faster voltage losses. However, at 575 °C, $(FeNiCoCrMn)S_2$ outperforms the $(FeNiCoCuTi)S_2$ which may be attributed to the lower thermal decomposition temperature of the $(FeNiCoCuTi)S_2$ high entropy disulfide.

From the discharge results shown in Figure 4.43, the internal resistances were calculated by Equation (3.1). The internal resistance calculations were performed at the start and end of the pulses separately. The former region is investigated to observe the immediate resistance reflected by the cells, whereas the latter region is investigated to determine the kinetic effects. The trend of internal resistance changes is given in Figure 4.44.

As shown in Figure 4.44 (a-d), the internal resistance curves demonstrate that at discharge temperatures of 475 °C and 525 °C, the resistance values of $(FeNiCoCuTi)S_2$ cathode are significantly lower than $(FeNiCoCrMn)S_2$ for the entire discharge time and pulse regions. Even when the discharge temperature is 575 °C, as given in Figure 4.44 (e-f), $(FeNiCoCuTi)S_2$ has lower internal resistances except for only a short discharge period between 175 and 240 seconds at the end of the pulses. These results prove that replacing chromium and manganese with copper and titanium elements in $(FeNiCoCrMn)S_2$ may improve the electrical conductivity of electrochemical cells. Since titanium has an average electrical conductivity between chromium and manganese, the enhanced overall conductivity may be ascribed mainly to copper's very high intrinsic electrical conductivity which is superior to each principal element in the $(FeNiCoCrMn)S_2$ high entropy disulfide. Based on this example, it is clear that the aimed electrical properties of high entropy disulfides may be tailored by selecting appropriate primary elements for the structure.
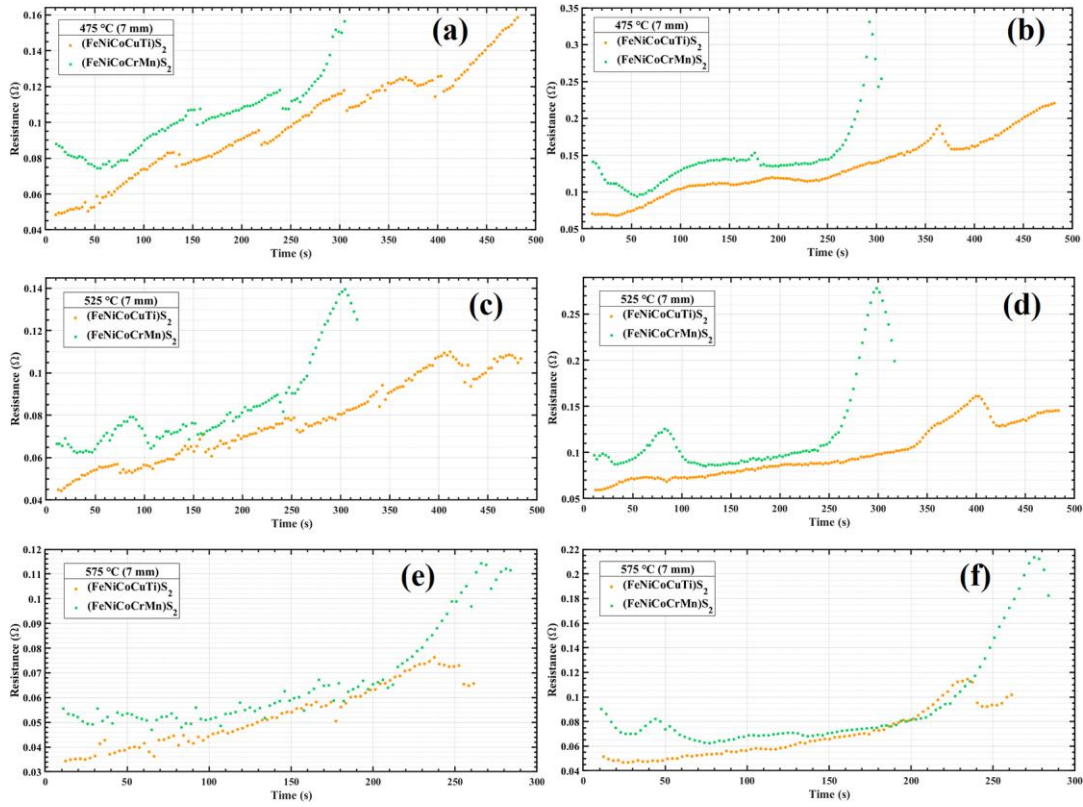
Figure 4.44 Internal resistances of single cells with $(FeNiCoCrMn)S_2$ and $(FeNiCoCuTi)S_2$ cathodes which are synthesized by WC balls with 7 mm diameters at 475 °C (a, b), 525 °C (c, d), and 575 °C (e, f) discharge temperatures, calculated at the start of the pulses (a, c, e) and the end of the pulses (b, d, f).

Based on the discharge curves in Figure 4.43, several cut-off voltages are chosen to compare specific capacities and energies of $(FeNiCoCrMn)S_2$ and $(FeNiCoCuTi)S_2$ high entropy disulfides. The chosen cut-off voltages are given in Table 4.9.

106

Table 4.9 Cut-off voltages chosen for comparison of the specific capacities and energies of (FeNiCoCrMn)S$_2$ and (FeNiCoCuTi)S$_2$ cathodes at different discharge temperatures.

Single Cell Test Temperature (°C)	Cut-off Voltage (V)
475	1.90
	1.60
	1.20
525	1.90
	1.40
	1.20
575	1.80
	1.50
	1.20

The confined discharge results obtained with selected cut-off voltages at discharge temperatures of 475 °C, 525 °C, and 575 °C are shown in Figure 4.45.

From the confined discharge results shown in Figure 4.45, the specific capacities and energies at different cut-off voltages are calculated by Equation (3.2) and Equation (3.3), respectively. The capacity and energy results are given in Table 4.10.
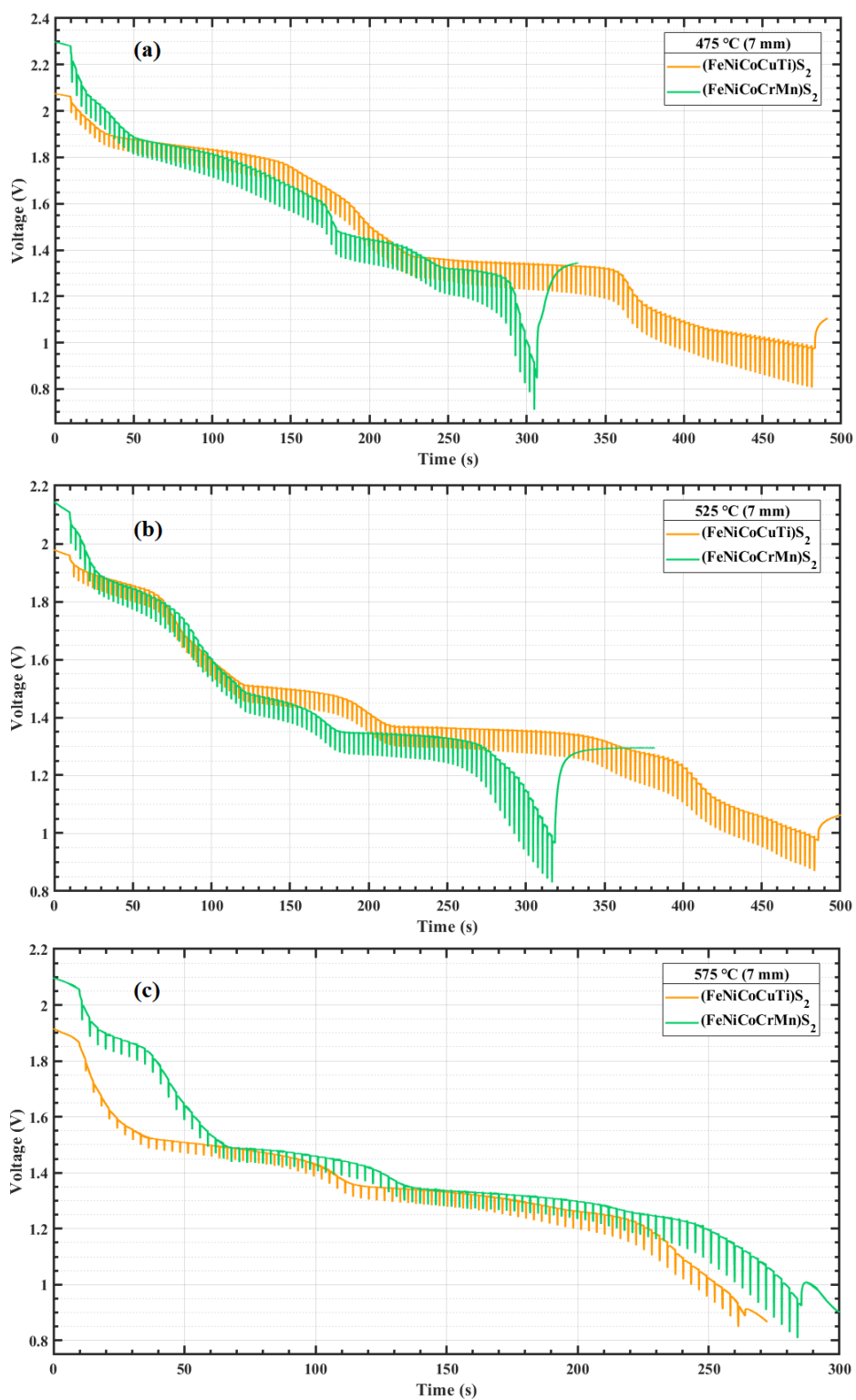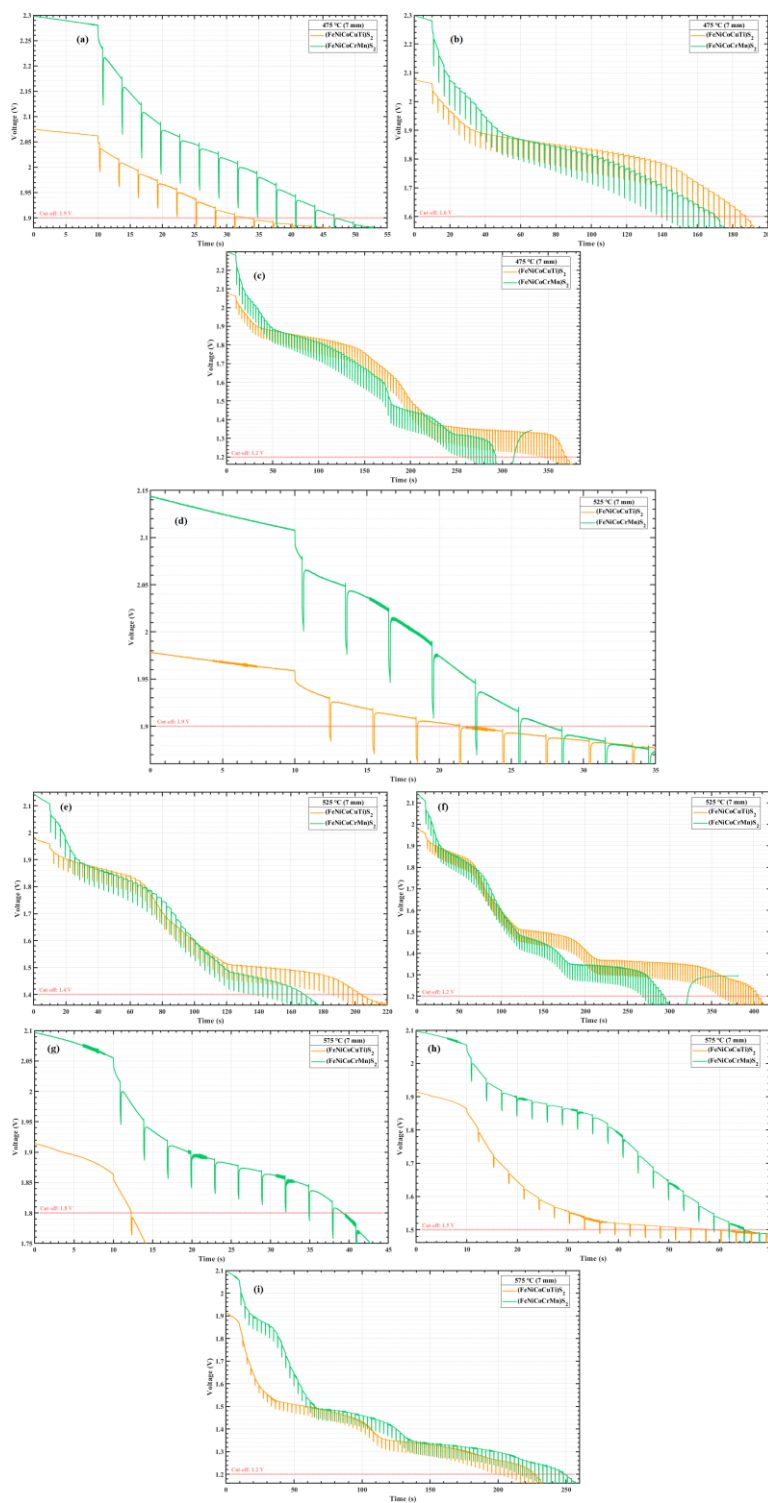
Figure 4.45 Discharge curves of single cells with (FeNiCoCrMn)S_2 and (FeNiCoCuTi)S_2 cathodes which are synthesized by WC balls with 7 mm diameters at (a-c) 475 ℃, (d) 525 ℃, and (e-g) 575 ℃ discharge temperatures with different cut-off voltages.

Table 4.10 Specific capacity and energy results of single cells with
(FeNiCoCrMn)S$_2$ and (FeNiCoCuTi)S$_2$ cathodes which are synthesized by WC
balls with 7 mm diameters at different discharge temperatures and cut-off voltages.

Cathode Material	Single Cell Test Temperature (°C)	Open Circuit Voltage (V)	Cut-off Voltage (V)	Specific Capacity (mAh g⁻¹)	Specific Energy (Wh kg⁻¹)
(FeNiCoCuTi)S$_2$	475	2.08	1.90	17.29	34.25
			1.60	179.75	329.23
			1.20	376.21	602.54
	525	1.98	1.90	3.11	6.05
			1.40	207.21	342.67
			1.20	411.51	618.67
	575	1.91	1.80	3.23	5.96
			1.50	28.76	47.45
			1.20	229.55	325.59
(FeNiCoCrMn)S$_2$ 7 mm	475	2.30	1.90	35.94	74.32
			1.60	163.82	306.22
			1.20	310.02	520.72
	525	2.14	1.90	17.11	34.58
			1.40	160.77	278.36
			1.20	326.48	502.91
	575	2.10	1.80	33.06	62.96
			1.50	63.71	114.64
			1.20	265.46	392.15

As shown in Table 4.10, owing to their relatively higher maximum voltages, the
specific capacity and energy of single cells with (FeNiCoCrMn)S$_2$ cathode at 475 °C

with the cut-off voltage of 1.90 V is 107.8% and 117% higher than $(FeNiCoCuTi)S_2$ cathode, respectively. Upon higher discharging times with cut-off voltages of 1.60 V and 1.20 V, $(FeNiCoCuTi)S_2$ achieves better discharge performances. When the cut-off voltage is 1.60 V, single cells with $(FeNiCoCuTi)S_2$ cathode have 9.7% and 7.5% higher specific capacity and energy than $(FeNiCoCrMn)S_2$, respectively. These results become 21.3% and 15.7% if the cut-off voltage is chosen as 1.20 V.

When the discharge temperature is 525 °C, a similar performance comparison between $(FeNiCoCrMn)S_2$ and $(FeNiCoCuTi)S_2$ cathodes is achieved with that of 475 °C. At the beginning of discharge, $(FeNiCoCrMn)S_2$ exhibits better capacities and energies for a short period thanks to their high open circuit voltages, then $(FeNiCoCuTi)S_2$ outperforms it with more stable and enlarged discharge plateaus. The single cells with $(FeNiCoCrMn)S_2$ cathode can achieve 450.3% and 471.9% higher specific capacity and energy with the cut-off voltage of 1.90 V than $(FeNiCoCuTi)S_2$, respectively. When the cut-off voltage is 1.40 V, $(FeNiCoCuTi)S_2$ cathodes have 28.9% and 23.1% higher specific capacity and energy values than $(FeNiCoCrMn)S_2$, respectively. If the discharge time is extended more and the cut-off voltage is chosen as 1.20 V, these electrochemical performance improvements become 26% and 23%, respectively.

Elevating the discharge temperature to 575 °C leads to a performance loss of $(FeNiCoCuTi)S_2$ cathode compared to $(FeNiCoCrMn)S_2$. For the entire discharging period, $(FeNiCoCrMn)S_2$ is superior to $(FeNiCoCuTi)S_2$ in terms of specific capacity and energy results. The single cells with $(FeNiCoCrMn)S_2$ cathode can achieve 924% and 956% higher specific capacity and energy than $(FeNiCoCuTi)S_2$ with the cut-off voltage of 1.80 V. If the cut-off voltage is 1.50 V, $(FeNiCoCrMn)S_2$ cathode has 121.5% and 141.6% higher specific capacity and energy than that of $(FeNiCoCuTi)S_2$, respectively. Even when the cut-off voltage is 1.20 V, $(FeNiCoCrMn)S_2$ cathode still exhibits 15.6% and 20.4% higher specific capacity and energy than $(FeNiCoCuTi)S_2$, respectively.

These electrochemical discharge results at different discharge temperatures suggest that substituting chromium and manganese in $(FeNiCoCrMn)S_2$ high entropy disulfides with copper and titanium elements may enhance the discharge life and prohibit relatively faster capacity losses. However, at elevated temperatures, the electrochemical performance could be degraded which may be attributed to the lower thermal decomposition temperature of $(FeNiCoCuTi)S_2$ relative to $(FeNiCoCrMn)S_2$. Therefore, regarding different thermal battery applications that can require higher platform voltages with shorter operating times, relatively lower discharge voltages with longer operating times, or excessive working temperatures, the principal high entropy disulfide elements may be alternated. As also evaluated in 4.6.4.1, application specific thermal battery cathodes may be designed thanks to this modifiability feature of high entropy disulfides.

4.6.5 Post-mortem Analyses of $(FeNiCoCrMn)S_2$, $(FeNiCo_{0.35}CrMn)S_2$, and $(FeNiCoCuTi)S_2$ High Entropy Disulfides

XRD was performed on the post-discharge products of $(FeNiCoCrMn)S_2$, $(FeNiCo_{0.35}CrMn)S_2$, and $(FeNiCoCuTi)S_2$ high entropy disulfides at each of the discharge temperatures of 475 °C, 525 °C, and 575 °C to investigate the discharging mechanism and to figure out the possible products. The anode, separator, and cathode pellets stuck together since the electrochemical single cell tests were performed under constant pressure and high temperature. Thus, to evaluate the cathode side predominantly, the cathode surface was separated from the current collector and XRD was performed on that surface. The post-discharge products and related XRD results for each temperature of $(FeNiCoCrMn)S_2$ – 5 mm, $(FeNiCoCrMn)S_2$ – 7 mm, $(FeNiCo_{0.35}CrMn)S_2$, and $(FeNiCoCuTi)S_2$ are given in Figure 4.46, Figure 4.47, Figure 4.48, and Figure 4.49, respectively.

The XRD results show that LiF, LiBr, LiCl, and MgO peaks are present besides the discharge products because of the electrolyte and binder content in the cathode pellet. In the XRD patterns Ni, Co, Ni_3S_2, Co_3S_4, Co_9S_8, Li_2S, and $Li_3Fe_2S_4$ are observed in

each of the high entropy disulfide cathodes. These are commonly seen in thermal battery cathode discharge products of metal disulfide cathode systems containing nickel, cobalt, and iron cations [29, 139-142]. Among these, Ni_3S_2, Co_9S_8, and Co_3S_4 may be categorized as intermediate discharge products of cathodes involving nickel and cobalt and their presence may be attributed to partial reductions and different reduction states across the material [29, 139, 140]. Further reductions of these compounds may lead to form elemental Ni and Co as final discharging products with Li_2S as by product [29, 140]. Moreover, $Li_3Fe_2S_4$ is frequently formed in electrochemical reactions of cathodes containing iron cations such as FeS_2 or $Fe_{0.2}Co_{0.8}S_2$ cathodes [141, 142]. Besides these discharge products, XRD patterns of $(FeNiCoCrMn)S_2$ and $(FeNiCo_{0.35}CrMn)S_2$ cathodes show some additional peaks or enhanced intensity values at shared peaks such as 44°, 58° or 77° 2ϑ values different than $(FeNiCoCuTi)S_2$. These changes are ascribed mainly to Cr_2S_3, MnS, Cr, and Mn. Similar to Ni_3S_2, Co_9S_8, and Co_3S_4, Cr_2S_3 and MnS may also be suggested as intermediate products of electrochemical reactions. On the other hand, for $(FeNiCoCuTi)S_2$ cathode, the different products compared to other high entropy disulfides are suggested as Cu_2S, TiS_2, Cu, and Ti. The XRD patterns of high entropy sulfide cathodes show that although different intensity ratios are observed at different discharge temperatures, the peak positions are nearly identical, and remarkable differences are not observed. However, the XRD results of $(FeNiCoCrMn)S_2 - 7$ mm at 475 °C and $(FeNiCo_{0.35}CrMn)S_2$ at 525 °C show irrelevant patterns which may be caused by a problem in the sampling or the operation of the XRD process because of the difficulty of obtaining a proper cathode surface from a stuck cathode, separator, anode, and current collector cell due to applied pressure and temperature in single cell testing. These post discharge results suggest that numerous cations in the high entropy sulfide structures may lead to both intermediate and final discharge products for each of the cations. Several elements with different electrochemical redox characteristics in the lattice and high operation temperatures of thermal batteries may lead to complicated discharge mechanisms and the relevant post discharge products may be formed as a result of partial or full reduction of the different cations.
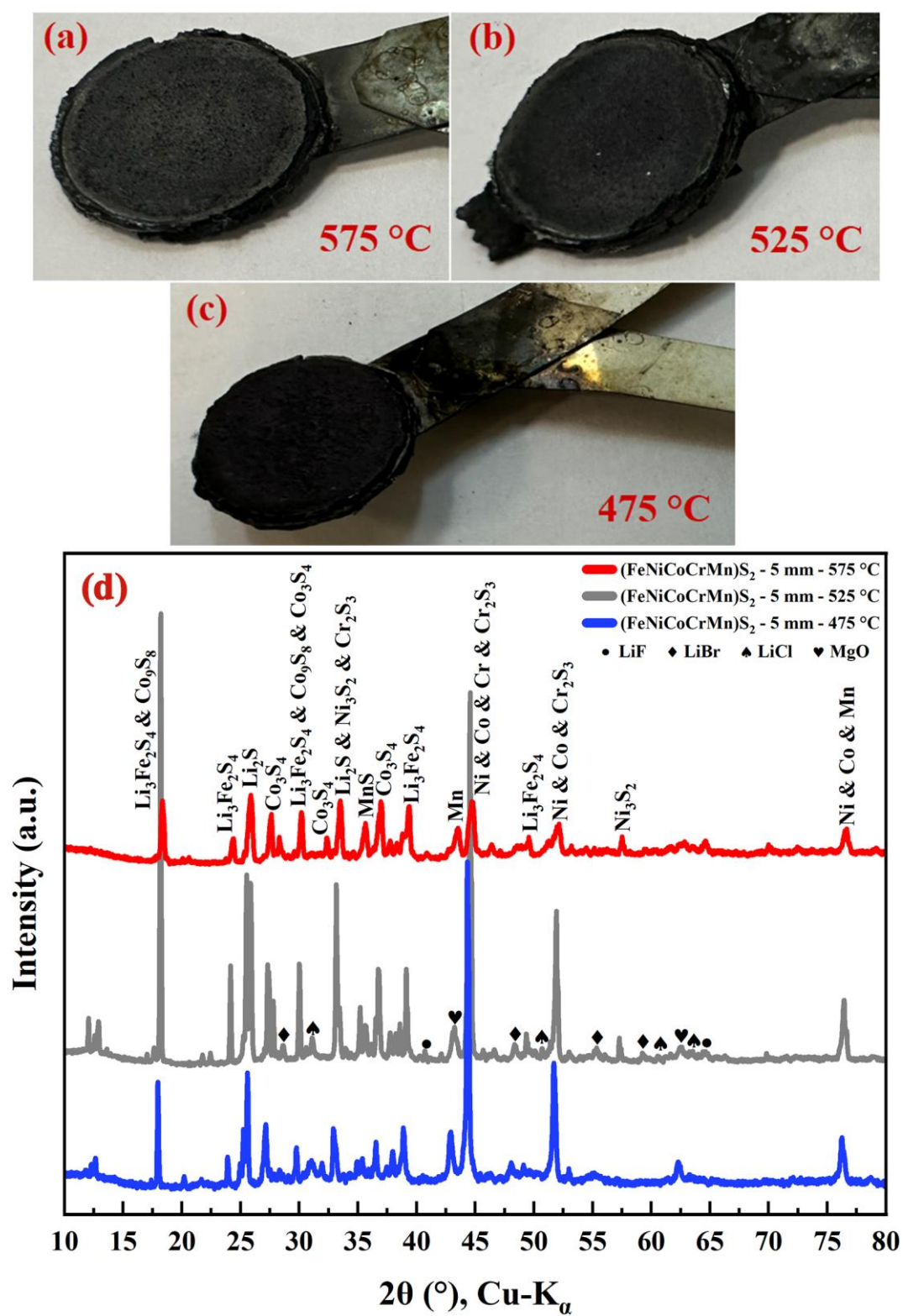
Figure 4.46 Post-discharge products (a-c) and XRD results (d) of $(FeNiCoCrMn)S_2$
– 5 mm at discharge temperatures of 475 °C, 525 °C, and 575 °C.
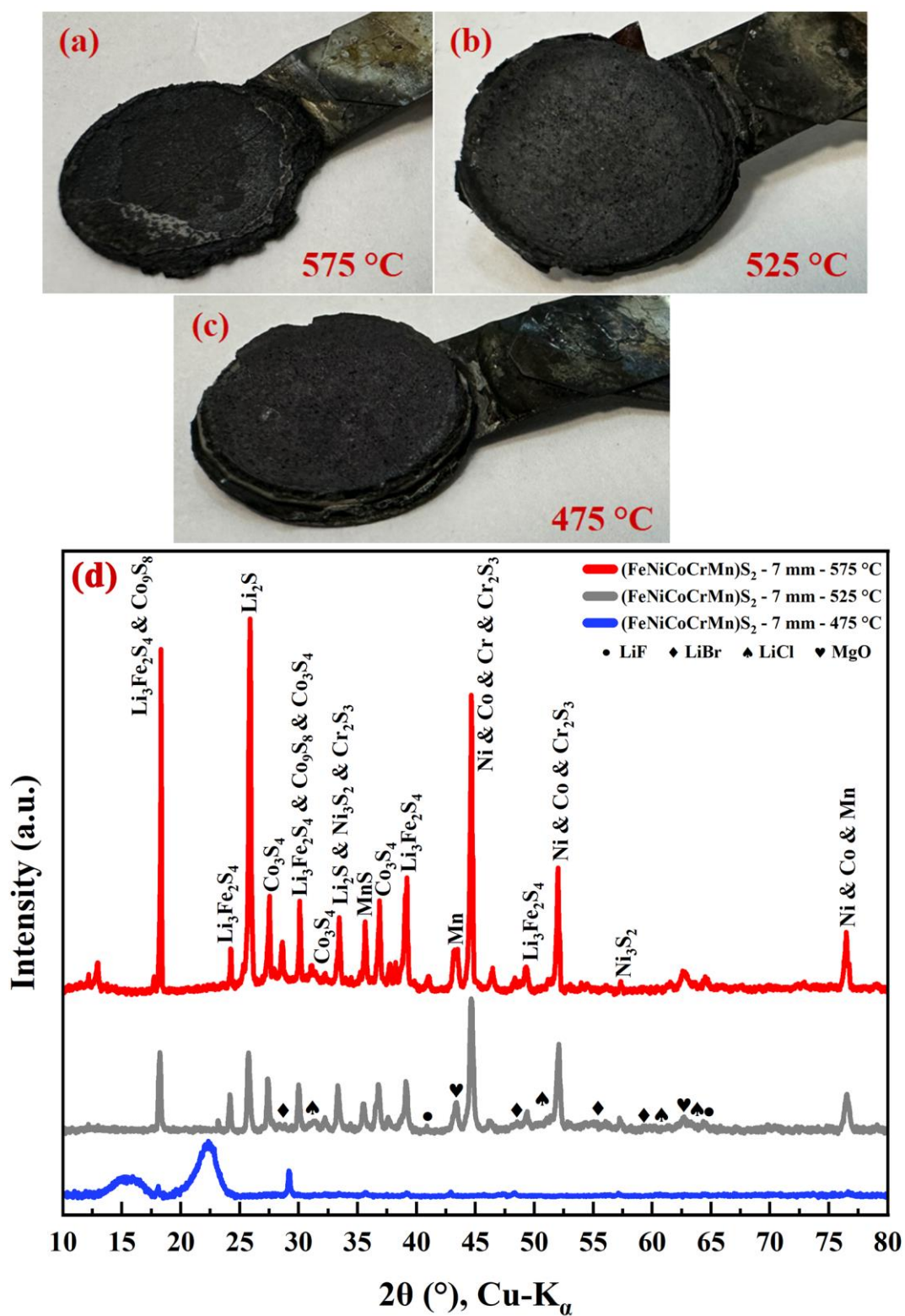
Figure 4.47 Post-discharge products (a-c) and XRD results (d) of $(FeNiCoCrMn)S_2$ – 7 mm at discharge temperatures of 475 °C, 525 °C, and 575 °C.
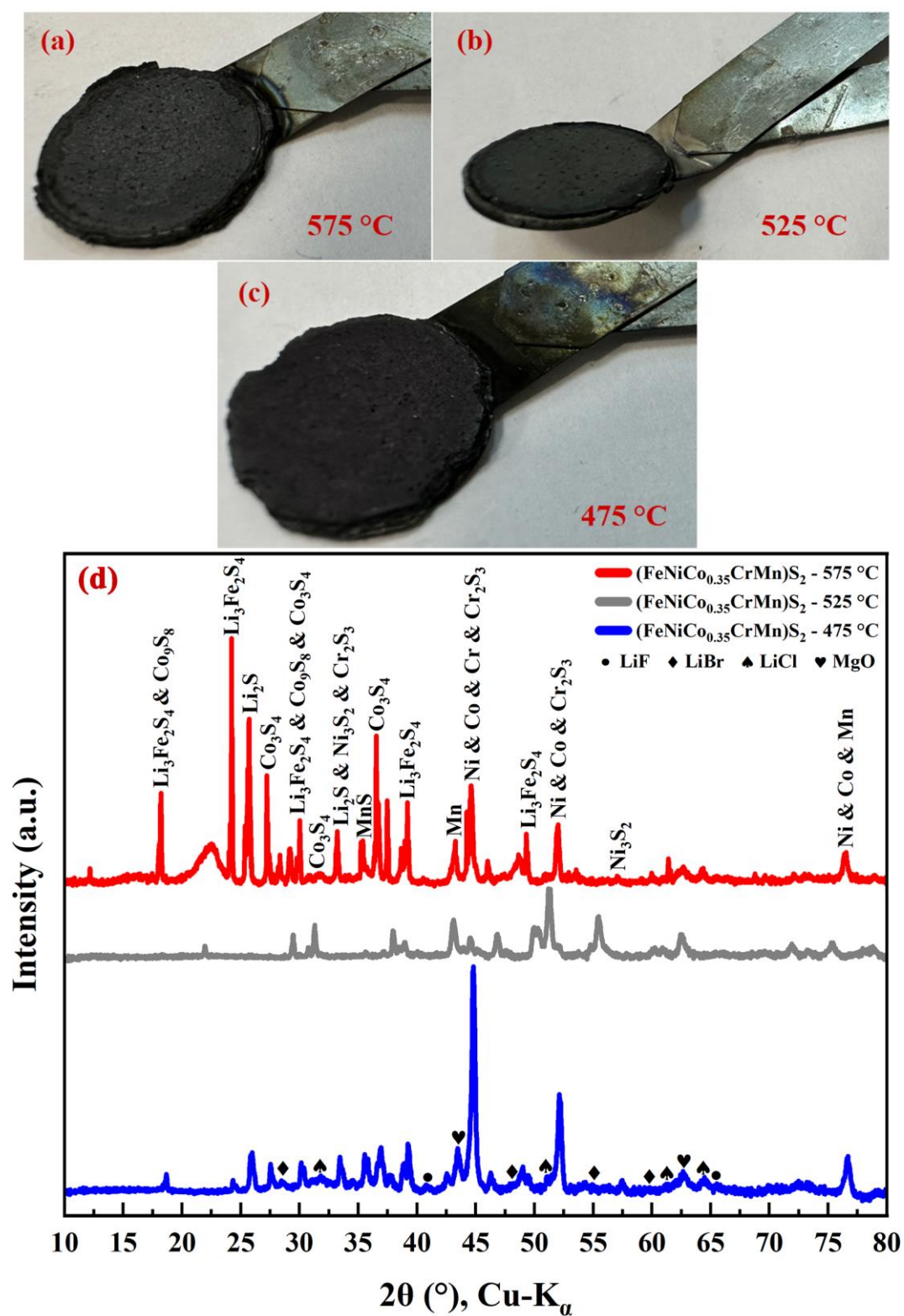
Figure 4.48 Post-discharge products (a-c) and XRD results (d) of (FeNiCo$_{0.35}$CrMn)S$_2$ at discharge temperatures of 475 °C, 525 °C, and 575 °C.
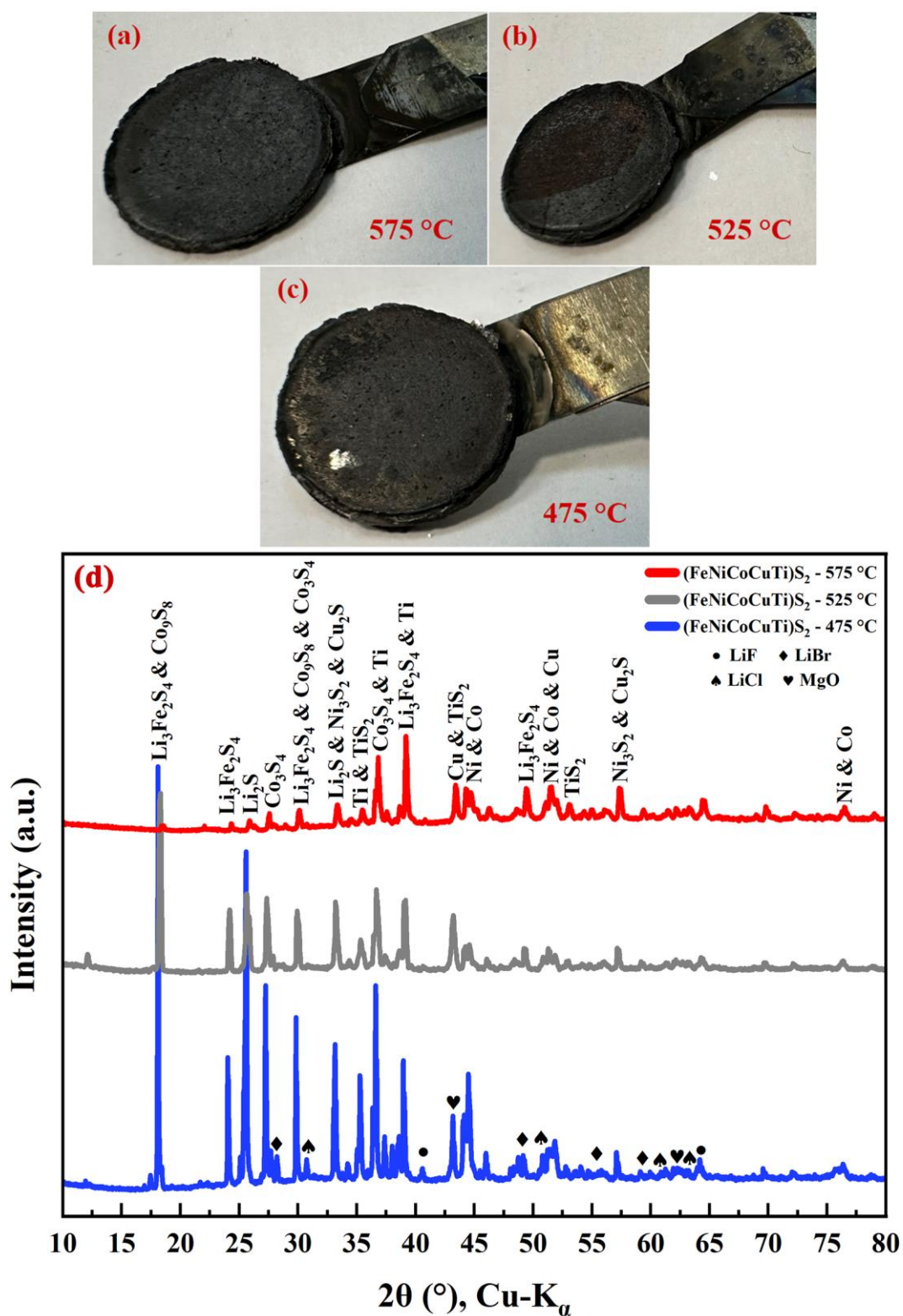
Figure 4.49 Post-discharge products (a-c) and XRD results (d) of (FeNiCoCuTi)S$_2$ at discharge temperatures of 475 °C, 525 °C, and 575 °C.

CHAPTER 5

CONCLUSIONS

In this thesis, high entropy sulfides were prepared by solvothermal and mechanochemical synthesis routes. After their detailed characterizations, they were tested as cathode active materials for thermal batteries. The following conclusions can be drawn regarding the results of this study.

- Mechanochemically synthesized $(FeNiCoCrMn)S_2$, $(FeNiCoCuTi)S_2$, and $(FeNiCo_{0.35}CrMn)S_2$ high entropy disulfides are successfully formed in a pyrite crystal structure (Pa-3) as single phases. However, the $(FeNiCoCrMn)S_x.aH_2O$ high entropy sulfide synthesized via the solvothermal method shows a hydrated structure that is unpreferable for thermal battery applications.

- The single cells with high entropy disulfide cathodes synthesized with the mechanochemical approach have significantly higher open circuit voltages in comparison with that of conventional FeS_2 cathode. The elevated open circuit voltage is mostly observed for $(FeNiCoCrMn)S_2$ equimolar disulfide with an open circuit voltage up to 2.30 V.

- $(FeNiCoCrMn)S_2$, $(FeNiCoCuTi)S_2$, and $(FeNiCo_{0.35}CrMn)S_2$ high entropy disulfides show outstanding electrochemical performance in terms of specific energy and capacity. Although their specific capacity and energy improvements compared to conventional FeS_2 vary at different discharge temperatures and cut-off voltages, they can outperform FeS_2, especially at lower operation times. Thus, they may be utilized in applications such as ejector seats employing short-life thermal batteries with short working time requirements.

- Electrochemical characteristics of high entropy disulfides can be successfully manipulated to achieve the desired properties. In comparison with

117

conventional FeS_2, $(FeNiCoCrMn)S_2$ high entropy disulfides show higher internal resistances which decrease their relative specific capacities at higher cut-off voltages and prohibit their usage at higher operation times. The addition of Cu as a primary element with excess inherent electrical conductivity decreased the internal resistance values and substantially enhanced the electrochemical performance at higher operation times. The single cell with $(FeNiCoCuTi)S_2$ cathode exhibits 40% and 21% higher specific capacities than that of conventional FeS_2 at 525 °C with 1.35 V and 1.10 V cut-off voltages, respectively. On the other hand, by increasing the Co content in the high entropy disulfides, the thermal stability and electrochemical properties at elevated temperatures are also successfully improved. $(FeNiCo_{0.35}CrMn)S_2$ cathode shows 62% and 50% higher specific capacity and energy in comparison with conventional FeS_2 at 575 °C with a cut-off voltage of 1.40 V.

These outcomes suggest that high entropy sulfides are promising cathode active materials for thermal batteries since they offer improved open-circuit voltages, specific capacities, and specific energies. In addition, the tunability of their structure by changing principal elements or altering the molar fractions may provide a limitless design of application-specific high entropy sulfide materials. Although some of their production methods can be time-consuming or difficult due to sulfide reactivity, their scalability can also be improved by continued research to make these high entropy sulfides more suitable for industrial applications.

REFERENCES

[1] Marin-Garcia, G., Vazquez-Guzman, G., Sosa, J. M., Lopez, A. R., Martinez-Rodriguez, P. R., & Langarica, D. (2020, November). Battery types and electrical models: A Review. In *2020 IEEE International Autumn Meeting on Power, Electronics and Computing (ROPEC)* (Vol. 4, pp. 1-6). IEEE.

[2] Zhao, Y., Pohl, O., Bhatt, A. I., Collis, G. E., Mahon, P. J., Rüther, T., & Hollenkamp, A. F. (2021). A review on battery market trends, second-life reuse, and recycling. *Sustainable Chemistry*, *2*(1), 167-205.

[3] Guidotti, R. A., & Masset, P. (2006). Thermally activated ("thermal") battery technology: Part I: An overview. *Journal of Power Sources*, *161*(2), 1443-1449.

[4] Stuart, S. (2018), *Reserve Batteries & You!* [PowerPoint slides]. Purdue University, West Lafayette, IN. https://nanohub.org/resources/28150.

[5] Schisselbauer, P. F., Bostwick, J. (2006, May 9–11). *Thermal Battery Development-Reduced Product Variability Through Six Sigma and Materials Finger-Printing* [Conference presentation]. 50th Annual NDIA Fuze Conference Norfolk, VA. https://ndiastorage.blob.core.usgovcloudapi.net/ndia /2006/fuze/kelly.pdf.

[6] Keener, M. (2014). Reliability of Thermal Batteries.

[7] Guidotti, R. A. (1995). Thermal batteries: A technology review and future directions.

[8] TÜBİTAK SAGE. (n.d.). *Thermal battery*. Retrieved November 28, 2024, from https://www.sage.tubitak.gov.tr/en/urunler/thermal-battery.

[9] Wesolowski, D. E., Papenguth, H. W., & Tuttle, L. W. (2012). *Lightweight packaging for thermal batteries* (No. SAND2012-2551C). Sandia National Lab. (SNL-NM), Albuquerque, NM (United States).

[10] Shin, J., Kang, H., Lee, Y., Ha, S. H., & Cho, E. (2022). Core–shell structured Li–Fe electrode for high energy and stable thermal battery. *RSC advances*, *12*(8), 4795-4804.

[11] Payne, J. L., Giagloglou, K., Carins, G. M., Crouch, C. J., Percival, J. D., Smith, R. I., ... & Irvine, J. T. (2018). In-situ studies of high temperature thermal batteries: a perspective. *Frontiers in Energy Research*, *6*, 121.

[12] Guidotti, R. A., & Masset, P. J. (2008). Thermally activated ("thermal") battery technology: Part IV. Anode materials. *Journal of Power Sources*, *183*(1), 388-398.

[13] Masset, P. J., & Guidotti, R. A. (2008). Thermal activated ("thermal") battery technology: Part IIIa: FeS2 cathode material. *Journal of Power Sources*, *177*(2), 595-609.

[14] Masset, P. J., & Guidotti, R. A. (2008). Thermal activated ("thermal") battery technology: Part IIIb. Sulfur and oxide-based cathode materials. *Journal of Power Sources*, *178*(1), 456-466.

[15] Ko, J., Kang, S. H., Cheong, H. W., Yoon, Y. S., Ko, J., Kang, S. H., ... & Yoon, Y. S. (2019). Recent progress in cathode materials for thermal batteries. *Journal of the Korean Ceramic Society*, *56*(3), 233-255.

[16] Choi, Y., Cho, S., & Lee, Y. S. (2014). Effect of the addition of carbon black and carbon nanotube to FeS2 cathode on the electrochemical performance of thermal battery. *Journal of Industrial and Engineering Chemistry*, *20*(5), 3584-3589.

[17] Ko, J., Kim, I. Y., Jung, H. M., Cheong, H., & Yoon, Y. S. (2017). Thin cathode for thermal batteries using a tape-casting process. *Ceramics International*, *43*(7), 5789-5793.

[18] Ko, J., Kim, I. Y., Cheong, H., & Yoon, Y. S. (2017). Organic binder-free cathode using FeS2-MWCNTs composite for thermal batteries. *Journal of the American Ceramic Society*, *100*(10), 4435-4441.

[19] Di Benedetto, G. L., Morris, L. A., Swanson, D. B., Wightman, B. D., Carpenter, R. R., McMullan, C. W., ... & Sanchez, P. A. (2021). Nanostructuring of iron disulfide cathode materials for enhanced thermal batteries. *Journal of The Electrochemical Society*, *168*(4), 046520.

[20] Xie, S., Deng, Y., Mei, J., Yang, Z., Lau, W. M., & Liu, H. (2017). Carbon coated CoS2 thermal battery electrode material with enhanced discharge performances and air stability. *Electrochimica Acta*, *231*, 287-293.

[21] Hu, J., Chu, Y., Tian, Q., Wang, J., Li, Y., Wu, Q., ... & Zhu, Y. (2018). Film cathode for thermal batteries using a screen-printing process. *Materials Letters*, *215*, 296-299.

[22] Hu, J., Zhao, L., Chu, Y., Tian, Q., Wang, J., Li, Y., ... & Zhu, Y. (2018). Preparation and electrochemical properties of a new Fe0. 5Co0. 5S2 cathode material for thermal batteries. *Journal of Alloys and Compounds*, *762*, 109-114.

[23] Tian, Q., Yu, Z., Wu, Y., & Liu, H. (2022). Synthesis and electrochemical performances of cathode material Fe0. 5Co0. 5S2 for thermal batteries by a facile molten salt method. *Journal of Materials Science: Materials in Electronics*, *33*(17), 13968-13976.

[24] Jin, C., Fu, L., Zhu, J., Yang, W., Li, D., & Zhou, L. (2018). A hierarchical carbon modified nano-NiS2 cathode with high thermal stability for a high energy thermal battery. *Journal of Materials Chemistry A*, *6*(16), 7123-7132.

[25] Jin, C., Song, K., Liu, J., Ge, B., Zhao, L., Pu, X., & Li, W. (2020). Flexible, self-assembly NiS2/C thin film cathodes for long life thermal battery. *Journal of Alloys and Compounds*, *833*, 155091.

[26] Yao, B., Fu, L., Liao, Z., Zhu, J., Yang, W., Li, D., & Zhou, L. (2022). Flexible NiS2 film as high specific capacity cathode for thermal battery. *Journal of Alloys and Compounds*, *900*, 163448.

[27] Xu, C., Jin, C., Gong, X., Wang, X., Xie, S., & Fan, Y. (2022). Increasing interfacial infiltration between cathode materials and solid molten salt for high power thermal batteries. *Journal of Energy Storage*, *45*, 103742.

[28] He, Y., Cao, L., Yuan, G., Fan, S., Li, Q., Bi, S., ... & Liu, H. (2020). Hydrothermally synthesized bimetallic disulfide Co x Ni 1-x S 2 as high-performance cathode material for lithium thermal battery. *Ionics*, *26*, 4985-4991.

[29] Guo, H., Tang, L., Tian, Q., Chu, Y., Shi, B., Yin, X., ... & Lu, Z. (2020). Cobalt-doped NiS2 micro/nanostructures with complete solid solubility as high-performance cathode materials for actual high-specific-energy thermal batteries. *ACS Applied Materials & Interfaces*, *12*(45), 50377-50387.

[30] Meng, X., Liu, H., Bi, S., Yang, C., Fan, S., & Cao, L. (2023). Structure modification of nickel sulfide cathode for enhanced performance in lithium thermal batteries. *Electrochimica Acta*, *464*, 142879.

[31] Zhang, C., Fu, L., Yao, B., Zhu, J., Yang, W., Li, D., & Zhou, L. (2023). Multi Element-Doped Ni-Based Disulfide Enhances the Specific Capacity of Thermal Batteries by High Thermal Stability. *ACS Applied Materials & Interfaces*, *15*(6), 8022-8032.

[32] Hu, J., Wang, X. L., Guo, H., Yang, M., Yuan, J. X., Chu, Y., & Zhao, L. L. (2022). High-Temperature Solid-State Synthesis and Electrochemical Properties of Transition Metal Sulfides for Thermal Batteries. *Energy Technology*, *10*(4), 2100885.

[33] Li, R., Guo, W., & Qian, Y. (2022). Recent Developments of Cathode Materials for Thermal Batteries. *Frontiers in Chemistry*, *10*, 832972.

[34] Giagloglou, K., Payne, J. L., Crouch, C., Gover, R. K., Connor, P. A., & Irvine, J. T. (2018). Transition metal chlorides NiCl2, KNiCl3, Li6VCl8 and Li2MnCl4 as alternative cathode materials in primary Li thermal batteries. *Journal of The Electrochemical Society*, *165*(14), A3510.

[35] Jin, C., Fu, L., Ge, B., Pu, X., Li, W., & Zhou, L. (2019). The NiCl2/NiS2@ C double active composite cathodes with surface synergistic effects for high-power thermal battery. *Journal of Alloys and Compounds*, *800*, 518-524.

[36] Tian, Q., Hu, J., Tang, L., Guo, H., Dong, Q., Wang, J., ... & Hu, W. (2021). A novel NiCl2-based cathode material for high-voltage thermal battery. *Materials Letters*, *301*, 130272.

[37] Cao, Y., Li, J., Yang, P., Wei, K., Ma, S., Zhang, X., ... & Wen, Z. (2021). Electrochemical performance of NiCl2 with Br-free molten salt electrolyte in high power thermal batteries. *Science China Technological Sciences*, *64*(1), 91-97.

[38] Tian, Q., Wang, J., Xiang, W., Zhao, J., Guo, H., Hu, J., ... & Hu, W. (2021). Fabrication of the Ni-NiCl2 composite cathode material for fast-response thermal batteries. *Frontiers in Chemistry*, *9*, 679231.

[39] Huang, M., Li, J., Li, S., Yue, B., Yang, M., Duan, J., ... & Liu, H. (2023). Controlling the Changes in Electrolyte Composition in the Cathode to Reduce the Voltage Decay of NiCl2 Thermal Batteries. *ACS Applied Energy Materials*, *6*(3), 1511-1518.

[40] Yao, B., Fu, L., Gui, Y., Zhu, J., Yang, W., Li, D., ... & Zhou, L. (2022). Instantaneous Activation of NiCl2 Cathode towards Thermal Battery by Constructing NiCl2–NiO Heterojunction. *ACS Sustainable Chemistry & Engineering*, *11*(1), 199-207.

[41] Yuan, Q., Li, B., Liu, Y., Li, Q., Zhang, Y., Wang, D., ... & Zhao, Y. (2023). The engineering strategy in fabrication and application of high-specific-energy cathode for thermal battery. *Electrochimica Acta*, *471*, 143390.

[42] Ge, Y. X., Luo, C. X., Zheng, X., & Liu, J. K. (2023). CoxNi1-xCl2 allomeric nanosheets with high specific surface area and excellent energy storage performance for cathode materials of thermal batteries. *Journal of Power Sources*, *584*, 233598.

[43] Chen, F., Jiang, C., Xu, L., Li, X., & Shen, Q. (2021). High utilization rate thermal batteries using PbCl2 as a cathode material. *Materials Letters*, *299*, 130018.

[44] nan Guo, S., Guo, H., Wang, X., Zhu, Y., Hu, J., Yang, M., ... & Wang, J. (2019). Iron trifluoride as a high voltage cathode material for thermal batteries. *Journal of the Electrochemical Society*, *166*(15), A3599.

[45] Kim, S. H., Choi, J. H., Park, S. H., Ahn, T. Y., Cheong, H. W., & Yoon, Y. S. (2023). FeF3/(acetylene black and multi-walled carbon nanotube) composite for cathode active material of thermal battery through formation of conductive network channels. *Nanomaterials*, *13*(20), 2783.

[46] Chang, Q., Luo, Z., Fu, L., Zhu, J., Yang, W., Li, D., & Zhou, L. (2020). A new cathode material of NiF2 for thermal batteries with high specific power. *Electrochimica Acta*, *361*, 137051.

[47] Tian, Q., Zhang, S., Guo, H., Tang, L., Dong, Q., Wang, J., ... & Hu, W. (2022). Preparation and properties of MnF3 cathode materials for high-voltage thermal batteries. *Materials Letters*, *324*, 132686.

[48] Hillel, T., & Ein-Eli, Y. (2013). Copper vanadate as promising high voltage cathodes for Li thermal batteries. *Journal of power sources*, *229*, 112-116.

[49] Dai, J., Lai, M., LaFollette, R. M., & Reisner, D. (2011). Thin film copper vanadium oxide electrodes for thermal batteries. *ECS Transactions*, *33*(27), 3.

[50] Roh, H. C., Kim, I. Y., Ahn, T. Y., Cheong, H. W., & Yoon, Y. S. (2021). Influence of temperature on performance of CuV 2 O 6 cathode for high voltage thermal battery. *Journal of the Korean Ceramic Society*, *58*, 507-518.

[51] Xu, C., Jin, C., Wang, X., Gong, X., Yin, J., Zhao, L., ... & Li, W. (2022). Structured confinement effects of hierarchical V2O5 cathodes to suppress flow of molten salt in high specific energy thermal batteries with binder-free MgO. *Electrochimica Acta*, *401*, 139496.

[52] Xu, C., Jin, C., Liu, L., Qi, Y., Xie, F., Chen, J., ... & Cheng, S. (2023). Stabilized electrode phase by prelithiating V2O5 cathode materials for high-specific energy thermal batteries. *Journal of Energy Storage*, *65*, 107284.

[53] Luo, Z., Fu, L., Zhu, J., Yang, W., Li, D., & Zhou, L. (2020). Cu2O as a promising cathode with high specific capacity for thermal battery. *Journal of Power Sources*, *448*, 227569.

[54] Liao, Z., Fu, L., Zhu, J., Yang, W., Li, D., & Zhou, L. (2020). High specific energy flexible CuO thin film cathode for thermal batteries. *Journal of Power Sources*, *463*, 228237.

[55] Wang, Y., Bai, X., Luo, Z., & Fu, L. (2020). High specific energy of CuO as a thermal battery cathode. *International Journal of Electrochemical Science*, *15*(10), 10406-10411.

[56] Liao, Z., Fu, L., Zhu, J., Yang, W., Li, D., & Zhou, L. (2020). Excellent electrochemical performance of flexible NiO thin film as thermal battery cathode. *Materials Letters*, *280*, 128592.

[57] Xia, X., Fu, L., Luo, Z., Zhu, J., Yang, W., Li, D., & Zhou, L. (2022). Discharge behavior of NiO as thermal battery cathode at ultrahigh temperature. *Electrochemistry Communications*, *134*, 107185.

[58] Wang, Y., Bai, X., Luo, Z., & Fu, L. (2020). High specific capacity thermal battery cathodes LiCu2O2 and LiCu3O3 prepared by a simple solid phase sintering. *Frontiers in Chemistry*, *8*, 575787.

[59] Guo, S., Guo, H., Wang, X., Zhu, Y., Yang, M., Zhang, Q., ... & Wang, J. (2019). Synthesis and electrochemical performance of WS2 nanosheet for thermal batteries. *Materials Letters*, *249*, 81-83.

[60] Chen, F., Guo, H., Zhao, L., Guo, X., Li, S., Chu, Y., ... & Zhu, Y. (2021). Defect engineering can enhance the electrochemical performance of WS2 for thermal batteries. *Journal of The Electrochemical Society*, *168*(10), 103507.

[61] Chen, F., Guo, H., Zhao, L., Chu, Y., Wang, X., & Zhu, Y. (2022). Study on electrochemical performance of WS2 cathode material for thermal battery prepared by one-step synthesis. *Ionics*, *28*(7), 3453-3460.

[62] Chen, F., Guo, H., Tang, L., Zhao, L., Chu, Y., Wang, X., & Zhu, Y. (2023). Vacancy engineering in transition metal sulfide and oxide composite material for thermal batteries of high specific capacity. *Materials Letters*, *350*, 134958.

[63] Zheng, X., Zhu, Y., Sun, Y., & Jiao, Q. (2018). Hydrothermal synthesis of MoS2 with different morphology and its performance in thermal battery. *Journal of Power Sources*, *395*, 318-327.

[64] Giagloglou, K., Payne, J. L., Crouch, C., Gover, R. K., Connor, P. A., & Irvine, J. T. (2016). Zirconium trisulfide as a promising cathode material for Li primary thermal batteries. *Journal of The Electrochemical Society*, *163*(14), A3126.

[65] Meng, J., Wang, M., Pan, Z., Wang, J., Tang, L., Tang, J., & Xiang, B. (2023). Preparation and electrochemical performance of FG/SnS2 composite as a cathode material for high power thermal batteries. *Materials Letters*, *351*, 135018.

[66] Zhao, J., Gao, S., Wei, H., Wei, Z., & Du, F. (2024). High Entropy Materials for Reversible Electrochemical Energy Storage Systems. *ChemElectroChem*, e202300606.

[67] Ma, Y., Ma, Y., Wang, Q., Schweidler, S., Botros, M., Fu, T., ... & Breitung, B. (2021). High-entropy energy materials: challenges and new opportunities. *Energy & Environmental Science*, *14*(5), 2883-2905.

[68] Schweidler, S., Botros, M., Strauss, F., Wang, Q., Ma, Y., Velasco, L., ... & Breitung, B. (2024). High-entropy materials for energy and electronic applications. *Nature Reviews Materials*, 1-16.

[69] Sarkar, A., Breitung, B., & Hahn, H. (2020). High entropy oxides: The role of entropy, enthalpy and synergy. *Scripta Materialia*, *187*, 43-48.

[70] Yeh, J. W. (2013). Alloy design strategies and future trends in high-entropy alloys. *Jom*, *65*, 1759-1771.

[71] Hsu, W. L., Tsai, C. W., Yeh, A. C., & Yeh, J. W. (2024). Clarifying the four core effects of high-entropy materials. *Nature Reviews Chemistry*, 1-15.

[72] Miracle, D. B., & Senkov, O. N. (2017). A critical review of high entropy alloys and related concepts. *Acta materialia*, *122*, 448-511.

[73] Sarkar, A., Wang, Q., Schiele, A., Chellali, M. R., Bhattacharya, S. S., Wang, D., ... & Breitung, B. (2019). High-entropy oxides: fundamental aspects and electrochemical properties. *Advanced Materials*, *31*(26), 1806236.

[74] Lin, L., Ding, Z., Karkera, G., Diemant, T., Kante, M. V., Agrawal, D., ... & Schweidler, S. (2023). High-entropy sulfides as highly effective catalysts for the oxygen evolution reaction. *Small Structures*, *4*(9), 2300012.

[75] Fu, M., Ma, X., Zhao, K., Li, X., & Su, D. (2021). High-entropy materials for energy-related applications. *Iscience*, *24*(3).

[76] Sarkar, A., Velasco, L., Wang, D. I., Wang, Q., Talasila, G., de Biasi, L., ... & Breitung, B. (2018). High entropy oxides for reversible energy storage. *Nature communications*, *9*(1), 3400.

[77] Shi, Z., Wang, L., Huang, Y., Kong, X. Y., & Ye, L. (2024). High-entropy catalysts: new opportunities toward excellent catalytic activities. *Materials Chemistry Frontiers*.

[78] Zhao, C., Ding, F., Lu, Y., Chen, L., & Hu, Y. S. (2020). High-entropy layered oxide cathodes for sodium-ion batteries. *Angewandte Chemie International Edition*, *59*(1), 264-269.

[79] Qiu, N., Chen, H., Yang, Z., Sun, S., Wang, Y., & Cui, Y. (2019). A high entropy oxide (Mg0. 2Co0. 2Ni0. 2Cu0. 2Zn0. 2O) with superior lithium storage performance. *Journal of Alloys and Compounds*, *777*, 767-774.

[80] Nguyen, T. X., Patra, J., Chang, J. K., & Ting, J. M. (2020). High entropy spinel oxide nanoparticles for superior lithiation–delithiation performance. *Journal of Materials Chemistry A*, *8*(36), 18963-18973.

[81] Wang, D., Jiang, S., Duan, C., Mao, J., Dong, Y., Dong, K., ... & Qi, X. (2020). Spinel-structured high entropy oxide (FeCoNiCrMn) 3O4 as anode towards superior lithium storage performance. *Journal of Alloys and Compounds*, *844*, 156158.

[82] Xiao, B., Wu, G., Wang, T., Wei, Z., Sui, Y., Shen, B., ... & Zheng, J. (2022). High-entropy oxides as advanced anode materials for long-life lithium-ion Batteries. *Nano Energy*, *95*, 106962.

[83] Sun, Z., Zhao, Y., Sun, C., Ni, Q., Wang, C., & Jin, H. (2022). High entropy spinel-structure oxide for electrochemical application. *Chemical Engineering Journal*, *431*, 133448.

[84] Wang, K., Hua, W., Huang, X., Stenzel, D., Wang, J., Ding, Z., ... & Mu, X. (2023). Synergy of cations in high entropy oxide lithium ion battery anode. *Nature Communications*, *14*(1), 1487.

[85] Wang, D., Liu, Z., Du, S., Zhang, Y., Li, H., Xiao, Z., ... & Wang, S. (2019). Low-temperature synthesis of small-sized high-entropy oxides for water oxidation. *Journal of Materials Chemistry A*, *7*(42), 24211-24216.

[86] Jin, Z., Lyu, J., Zhao, Y. L., Li, H., Chen, Z., Lin, X., ... & Qiu, H. J. (2021). Top–down synthesis of noble metal particles on high-entropy oxide supports for electrocatalysis. *Chemistry of Materials*, *33*(5), 1771-1780.

[87] Kante, M. V., Weber, M. L., Ni, S., van den Bosch, I. C., van der Minne, E., Heymann, L., ... & Baeumer, C. (2023). A high-entropy oxide as high-activity electrocatalyst for water oxidation. *ACS nano*, *17*(6), 5329-5339.

[88] Akrami, S., Murakami, Y., Watanabe, M., Ishihara, T., Arita, M., Fuji, M., & Edalati, K. (2022). Defective high-entropy oxide photocatalyst with high activity for CO2 conversion. *Applied Catalysis B: Environmental*, *303*, 120896.

[89] Jiang, Z., Zhang, R., Zhao, H., Wang, J., Jia, L., Hu, Y., ... & Wang, X. (2023). Preparation of (Ga0. 2Cr0. 2Mn0. 2Ni0. 2Zn0. 2) 3O4 high-entropy oxide with narrow bandgap for photocatalytic CO2 reduction with water vapor. *Applied Surface Science*, *612*, 155809.

[90] Tehrani, Z. P., Fromme, T., Reichenberger, S., Gökce, B., Ishihara, T., Lippert, T., & Edalati, K. (2024). Laser fragmentation of a high-entropy oxide for enhanced photocatalytic carbon dioxide (CO2) conversion and hydrogen (H2) production. *Advanced Powder Technology*, *35*(5), 104448.

[91] Wang, Z., Li, Z. T., Zhao, S. J., & Wu, Z. G. (2021). High-entropy carbide ceramics: a perspective review. *Tungsten*, *3*(2), 131-142.

[92] Tunes, M. A., Fritze, S., Osinger, B., Willenshofer, P., Alvarado, A. M., Martinez, E., ... & El-Atwani, O. (2023). From high-entropy alloys to high-entropy ceramics: The radiation-resistant highly concentrated refractory carbide (CrNbTaTiW) C. *Acta Materialia*, *250*, 118856.

[93] Yan, X., Constantin, L., Lu, Y., Silvain, J. F., Nastasi, M., & Cui, B. (2018). (Hf0. 2Zr0. 2Ta0. 2Nb0. 2Ti0. 2) C high-entropy ceramics with low thermal conductivity. *Journal of the American Ceramic Society*, *101*(10), 4486-4491.

[94] Feng, L., Fahrenholtz, W. G., & Brenner, D. W. (2021). High-entropy ultra-high-temperature borides and carbides: a new class of materials for extreme environments. *Annual Review of Materials Research*, *51*(1), 165-185.

[95] Wang, F., Monteverde, F., & Cui, B. (2023). Will high-entropy carbides and borides be enabling materials for extreme environments?. *International Journal of Extreme Manufacturing*, *5*(2), 022002.

[96] Shen, W. J., Tsai, M. H., Tsai, K. Y., Juan, C. C., Tsai, C. W., Yeh, J. W., & Chang, Y. S. (2013). Superior oxidation resistance of (Al0. 34Cr0. 22Nb0. 11Si0. 11Ti0. 22) 50N50 high-entropy nitride. *Journal of the Electrochemical Society*, *160*(11), C531.

[97] Hahn, R., Kirnbauer, A., Bartosik, M., Kolozsvári, S., & Mayrhofer, P. H. (2019). Toughness of Si alloyed high-entropy nitride coatings. *Materials Letters*, *251*, 238-240.

[98] Khan, N. A., Akhavan, B., Zhou, C., Zhou, H., Chang, L., Wang, Y., ... & Liu, Z. (2020). High entropy nitride (HEN) thin films of AlCoCrCu0. 5FeNi deposited by reactive magnetron sputtering. *Surface and Coatings Technology*, *402*, 126327.

[99] Li, H., Jiang, N., Li, J., Huang, J., Kong, J., & Xiong, D. (2021). Hard and tough (NbTaMoW) Nx high entropy nitride films with sub-stoichiometric nitrogen. *Journal of Alloys and Compounds*, *889*, 161713.

[100] Zhao, Y., Chen, S., Chen, Y., Wu, S., Xie, W., Yan, W., ... & Zhang, S. (2022). Super-hard and anti-corrosion (AlCrMoSiTi) Nx high entropy nitride coatings by multi-arc cathodic vacuum magnetic filtration deposition. *Vacuum*, *195*, 110685.

[101] Moskovskikh, D., Vorotilo, S., Buinevich, V., Sedegov, A., Kuskov, K., Khort, A., ... & Mukasyan, A. (2020). Extremely hard and tough high entropy nitride ceramics. *Scientific reports*, *10*(1), 19874.

[102] Dippo, O. F., Mesgarzadeh, N., Harrington, T. J., Schrader, G. D., & Vecchio, K. S. (2020). Bulk high-entropy nitrides and carbonitrides. *Scientific reports*, *10*(1), 21288.

[103] Suhr, E., Krysiak, O. A., Strotkötter, V., Thelen, F., Schuhmann, W., & Ludwig, A. (2023). High-Throughput Exploration of Structural and Electrochemical Properties of the High-Entropy Nitride System (Ti–Co–Mo–Ta–W) N. *Advanced Engineering Materials*, *25*(22), 2300550.

[104] Salian, A., Sengupta, P., Vishalakshi Aswath, I., Gowda, A., & Mandal, S. (2023). A review on high entropy silicides and silicates: Fundamental aspects, synthesis, properties. *International Journal of Applied Ceramic Technology*, *20*(5), 2635-2660.

[105] Liu, D., Huang, Y., Liu, L., & Zhang, L. (2020). A novel of MSi2 high-entropy silicide: Be expected to improve mechanical properties of MoSi2. *Materials Letters*, *268*, 127629.

[106] Gild, J., Braun, J., Kaufmann, K., Marin, E., Harrington, T., Hopkins, P., ... & Luo, J. (2019). A high-entropy silicide:(Mo0. 2Nb0. 2Ta0. 2Ti0. 2W0. 2) Si2. *Journal of Materiomics*, *5*(3), 337-343.

[107] Qin, Y., Liu, J. X., Li, F., Wei, X., Wu, H., & Zhang, G. J. (2019). A high entropy silicide by reactive spark plasma sintering. *Journal of Advanced Ceramics*, *8*, 148-152.

[108] Zhang, Y., Guo, W. M., Jiang, Z. B., Zhu, Q. Q., Sun, S. K., You, Y., ... & Lin, H. T. (2019). Dense high-entropy boride ceramics with ultra-high hardness. *Scripta Materialia*, *164*, 135-139.

[109] Iwan, S., Lin, C. M., Perreault, C., Chakrabarty, K., Chen, C. C., Vohra, Y., ... & Velisavljevic, N. (2022). High-entropy borides under extreme environment of pressures and temperatures. *Materials*, *15*(9), 3239.

[110] Sukkurji, P. A., Cui, Y., Lee, S., Wang, K., Azmi, R., Sarkar, A., ... & Breitung, B. (2021). Mechanochemical synthesis of novel rutile-type high entropy fluorides for electrocatalysis. *Journal of Materials Chemistry A*, *9*(14), 8998-9009.

[111] Cui, Y., Sukkurji, P. A., Wang, K., Azmi, R., Nunn, A. M., Hahn, H., ... & Botros, M. (2022). High entropy fluorides as conversion cathodes with tailorable electrochemical performance. *Journal of Energy Chemistry*, *72*, 342-351.

[112] Wang, T., Chen, H., Yang, Z., Liang, J., & Dai, S. (2020). High-entropy perovskite fluorides: a new platform for oxygen evolution catalysis. *Journal of the American Chemical Society*, *142*(10), 4550-4554.

[113] Wang, X., Liu, G., Tang, C., Tang, H., Zhang, W., Ju, Z., ... & Cui, Y. (2023). A novel high entropy perovskite fluoride anode with 3D cubic framework for advanced lithium-ion battery. *Journal of Alloys and Compounds*, *934*, 167889.

[114] Chen, X., & Wu, Y. (2020). High-entropy transparent fluoride laser ceramics. *Journal of the American Ceramic Society*, *103*(2), 750-756.

[115] Cheng, W., Liu, J., Hu, J., Peng, W., Niu, G., Li, J., ... & Gou, H. (2023). Pressure-Stabilized High-Entropy (FeCoNiCuRu) S2 Sulfide Anode toward Simultaneously Fast and Durable Lithium/Sodium Ion Storage. *Small*, *19*(29), 2301915.

[116] Li, S., Tong, L., Zhang, B., & Fu, X. (2024). First-principles study of high-entropy sulfides and their alkali metal-doped modification as cathode material for sodium-ion batteries. *ChemPhysChem*, e202300999.

[117] Cui, M., Yang, C., Li, B., Dong, Q., Wu, M., Hwang, S., ... & Hu, L. (2021). High-entropy metal sulfide nanoparticles promise high-performance oxygen evolution reaction. *Advanced Energy Materials*, *11*(3), 2002887.

[118] Xiao, W., Li, Y., Elgendy, A., Duran, E. C., Buckingham, M. A., Spencer, B. F., ... & Lewis, D. J. (2023). Synthesis of High Entropy and Entropy-Stabilized Metal Sulfides and Their Evaluation as Hydrogen Evolution Electrocatalysts. *Chemistry of Materials*, *35*(19), 7904-7914.

[119] Laila, A. Z., Fronzi, M., Kumegai, S., Sugiyama, K., Furui, R., & Yamamoto, A. (2022). High-pressure synthesis of high-entropy metal disulfides with pyrite-type structure. *journal of the physical society of japan*, *91*(8), 084802.

[120] Zhang, R. Z., Gucci, F., Zhu, H., Chen, K., & Reece, M. J. (2018). Data-driven design of ecofriendly thermoelectric high-entropy sulfides. *Inorganic chemistry*, *57*(20), 13027-13033.

[121] Lin, L., Wang, K., Sarkar, A., Njel, C., Karkera, G., Wang, Q., ... & Breitung, B. (2022). High-entropy sulfides as electrode materials for Li-ion batteries. *Advanced energy materials*, *12*(8), 2103090.

[122] McCormick, C. R., & Schaak, R. E. (2021). Simultaneous multication exchange pathway to high-entropy metal sulfide nanoparticles. *Journal of the American Chemical Society*, *143*(2), 1017-1023.

[123] Lei, Y., Zhang, L., Xu, W., Xiong, C., Chen, W., Xiang, X., ... & Shang, H. (2022). Carbon-supported high-entropy Co-Zn-Cd-Cu-Mn sulfide nanoarrays promise high-performance overall water splitting. *Nano Research*, *15*(7), 6054-6061.

[124] Theibault, M. J., McCormick, C. R., Lang, S., Schaak, R. E., & Abruña, H. D. (2023). High entropy sulfide nanoparticles as lithium polysulfide redox catalysts. *ACS nano*, *17*(18), 18402-18410.

[125] Moradi, M., Hasanvandian, F., Bahadoran, A., Shokri, A., Zerangnasrabad, S., & Kakavandi, B. (2022). New high-entropy transition-metal sulfide nanoparticles for electrochemical oxygen evolution reaction. *Electrochimica Acta*, *436*, 141444.

[126] Li, F., Ma, Y., Wu, H., Zhai, Q., Zhao, J., Ji, H., ... & Meng, X. (2022). Sub-3-nm high-entropy metal sulfide nanoparticles with synergistic effects as promising electrocatalysts for enhanced oxygen evolution reaction. *The Journal of Physical Chemistry C*, *126*(43), 18323-18332.

[127] Guo, M., Li, P., Wang, A., Wang, J., Chen, J., Lei, F., ... & Tang, B. (2023). Topotactic synthesis of high-entropy sulfide nanosheets as efficient pre-catalysts for water oxidation. *Chemical Communications*, *59*(34), 5098-5101.

[128] Yang, P., Sun, M., Wang, J., Li, J., Yang, R., Hao, Y., ... & Liu, X. (2024). High-entropy sulfurization enables efficient non-noble metal-based NiCoFeCuS electrocatalyst for alkaline oxygen evolution reaction. *Particuology*.

[129] Shi, J., Jiang, H., Hong, X., & Tang, J. (2024). Non-noble metal high entropy sulfides for efficient oxygen evolution reaction catalysis. *Applied Surface Science*, *642*, 158598.

[130] Adabasi, G., Deshpande, A., Tanaka, K., Ancheta, J., Maldonado, E., Özdoğan, M., ... & Baykara, M. Z. (2023). Nanoscale friction of high entropy alloy sulfide thin films in comparison with molybdenum disulfide. *Applied Physics Letters*, *123*(26).

[131] Ren, Y., & Zhang, S. (2020). Long Cycle Life TiC Anode Fabricated via High-Energy Ball Mill for Li-Ion Battery. *Journal of Nanomaterials*, *2020*(1), 5603086.

[132] Shivam, V., Shadangi, Y., Basu, J., & Mukhopadhyay, N. K. (2019). Alloying behavior and thermal stability of mechanically alloyed nano AlCoCrFeNiTi high-entropy alloy. *Journal of Materials Research*, *34*(5), 787-795.

[133] Arshad, J., Janjua, N. K., & Raza, R. (2021). Synthesis of Novel (Be, Mg, Ca, Sr, Zn, Ni) 3 O 4 High Entropy Oxide with Characterization of Structural and Functional Properties and Electrochemical Applications. *Journal of Electrochemical Science and Technology*, *12*(1), 112-125.

[134] Spiridigliozzi, L., & Dell'Agli, G. (2024). A novel high-entropy rare-earth hydroxycarbonate synthesized via facile hydrothermal synthesis with superior decomposition temperature. *Materials Letters*, *372*, 137090.

[135] Hasanvandian, F., Fayazi, D., Kakavandi, B., Giannakis, S., Sharghi, M., Han, N., & Bahadoran, A. (2024). Revitalizing CO2 photoreduction: Fine-tuning electronic synergy in ultrathin g-C3N4 with amorphous (CoFeNiMnCu) S2 high-entropy sulfide nanoparticles for enhanced sustainability. *Chemical Engineering Journal*, *496*, 153771.

[136] Liao, Y. J., Shen, W. W., Chang, C. B., & Tuan, H. Y. (2023). High-entropy transition metal disulfide colloid clusters: synergistic atomic scale interaction and interconnected network for ultra-stable potassium ion storage. *Chemical Engineering Journal*, *469*, 143942.

[137] Bo, L., Fang, J., Yang, S., Nian, F., Pu, L., Ma, Z., & Tong, J. (2024). Modulating electron structure of active sites in high-entropy metal sulfide

nanoparticles with greatly improved electrocatalytic performance for oxygen evolution reaction. *International Journal of Hydrogen Energy*, *84*, 89-96.

[138] Etghani, S. A., Ansari, E., & Mohajerzadeh, S. (2019). Evolution of large area TiS2-TiO2 heterostructures and S-doped TiO2 nano-sheets on titanium foils. *Scientific Reports*, *9*(1), 17943.

[139] Xie, Y., Liu, Z., Ning, H., Huang, H., & Chen, L. (2018). Suppressing self-discharge of Li–B/CoS 2 thermal batteries by using a carbon-coated CoS 2 cathode. *RSC advances*, *8*(13), 7173-7178.

[140] Meng, X., Liu, H., Ji, L., Gao, W., Bi, S., Fan, S., ... & Cao, L. (2024). Rational design of low interfacial resistance between NiS2 cathode and electrolyte for high-performance Li thermal battery. *Journal of Energy Storage*, *90*, 111719.

[141] Li, J., Chen, X., Shao, S., Tang, L., Zhu, J., Yang, W., ... & Fu, L. (2024). High capacity Co0. 8Fe0. 2S2 thermal battery cathode prepared by a solid-state synthesis technique. *Electrochimica Acta*, *498*, 144623.

[142] Li, W., Quan, T., Zhang, N., Bu, X., Jiao, Q., Zhu, Y., & Zhang, L. (2024). Preparation of LiLaZrMO (M= Ga/Al) solid electrolytes for thermal batteries. *Journal of Power Sources*, *613*, 234928.